Surface-anchored metal-organic frameworks for optical applications

Zur Erlangung des akademischen Grades eines
Doktor-Ingenieurs
von der KIT-Fakultät für Elektrotechnik und Informationstechnik des
Karlsruher Instituts für Technologie (KIT)
genehmigte
DISSERTATION
von

Nicolò Baroni, M.Sc.

Tag der mündlichen Prüfung:	Karlsruhe 13. November 2019
Hauptreferent:	Prof. Dr. Bryce Sydney Richards
Korreferent:	Prof. Dr. Paolo Falcaro

Table of contents

Kurzfassung

Lumineszierende Materialien, auch bekannt als Leuchtstoffe, die nach optischer Anregung Licht emittieren, haben viele Anwendungen wie Beleuchtung, Displays, Marker (z.B. in der Mikroskopie) und Energieumwandlung. Traditionell können Leuchtstoffe in die Kategorien anorganische und organische Materialien unterteilt werden, sowie in solche, die Fluoreszenz und Phosphoreszenz emittieren. Die Definition von Phosphoreszenz impliziert im Allgemeinen, dass seine Lumineszenz eine Zerfallszeit von mehr als 1 ms aufweist, während die Zerfallszeit eines fluoreszierenden Materials kürzer ist (im Falle von organischen Leuchtstoffen ist die Definition strenger: Lumineszenz ist die Emission aus einem angeregten singlet Zustand, und Phosphoreszenz ist die aus einem angeregten triplet Zustand). Daher werden in der Regel fluoreszierende Materialien für eine effiziente Lichtemission gesucht, aber phosphoreszierende Materialien sind für Anwendungen interessant, bei denen die Persistenz ihrer Emission von Nutzen sein kann. Anorganische Leuchtstoffe sind in der Regel kristalline Wirtsmaterialien, die mit Übergangs- oder Seltenerdmetallen dotiert sind, um die Lumineszenz zu aktivieren. Die gebräuchlichsten Wirtsmaterialien nennen sich Garnets, mit der chemischen Formel $A_3B_5O_{12}$, wobei A und B zwei verschiedene Elemente sind und O Sauerstoff ist. Einige Beispiele für optisch aktive Seltene Erden sind Cerium zur Erzeugung von Weißlicht, Neodym welches bereits für Laser und Erbium das in optischen Verstärkern Verwendung findet.

Zu den Vorteilen der organischen Leuchtstoffe gehören ihre hohen Absorptionsquerschnitte und ihre große Abstimmbarkeit. Durch die umfangreiche Kommerzialisierung organischer Leuchtdioden in den letzten Jahren, ist das Interesse an organischen Leuchtstoffen derzeit besonders hoch. Sie werden auch für Anwendungen in der Energieumwandlung eingesetzt, wie z.B. für lumineszierende Solarkonzentratoren.

Normalerweise sind organische Leuchtstoffe amorphe Mischungen aus kleinen Molekülen und Polymeren. Dies macht es schwierig, Wechselwirkungen zwischen dem organischen Wirtsmaterial und den organischen "Aktivator"-Chromophoren zu konstruieren. Eine Möglichkeit, diese Aspekte zu kontrollieren, bestand darin, organische Chromophore in poröse anorganische Wirte, wie beispielsweise Zeolithe, zu laden. In den letzten Jahren wurde jedoch eine neue Klasse von nanoporösen Hybridmaterialien, metallorganische Gerüste (MOFs), synthetisiert. MOFs kombinieren die interessanten Eigenschaften von anorganischen und organischen porösen Materialien wie z.B. genau definierte und geordnete Poren sowie die Vielseitigkeit der chemischen Synthese. In dieser Arbeit wurden Methoden zum Laden von lumineszierenden Gastchromophoren in einer bestimmten Art von MOF, die in einer Dünnschichtkonfiguration auf ein Substrat aufgebracht wurden, entwickelt und untersucht. Diese Art von MOFs werden auch oberflächenverankerte metallorganische Gerüste (SURMOFs) genannt. ZnBDC SURMOF, bestehend aus Zink und Bi-Carboxylatbenzol als anorganische bzw. organische Komponenten, wurde untersucht und es wurde gezeigt, dass flache Moleküle zwischen den einzelnen Ebenen dieses SURMOFs eingebracht werden können.

Die Einarbeitung der Chromophorenmoleküle erfolgte durch Drop-Casting der Farbstofflösung auf den SURMOF. Die Grundparameter für die Gastmolekülbeladung wurden mit metallisierten Porphyrinmolekülen untersucht, wodurch festgestellt wurde, dass das Vorhandensein von Carboxylgruppen ein entscheidender Faktor für eine erfolgreiche Beladung ist. Die Farbstoffbeladung wurde mit Hilfe der Sekundärionen-Massenspektroskopie (ToF-SIMS) detailliert untersucht, welche ein Tiefenprofil der Zusammensetzungen der geladenen Proben liefert und dadurch aufzeigen konnte, dass eine gleichmäßige Beladung des SURMOFs über die gesamte Tiefe erreicht werden konnte. Der gleiche Beladungsansatz wurde auch auf 4',4‴,4‴',4‴'',4‴''',4‴'''''-(Ethen-1,1,2,2-tetrayl)tetrakis-(([1,1'-biphenyl]-3-carbonsäure)) angewendet. (H_4ETTC), einen aggregierungsinduzierten Emissionsfarbstoff (AIE), der aufgrund der Einschränkung der Molekularbewegung eine erhöhte Emission aufweist, wenn er in das SURMOF-Gerüst

eingebaut wird. Eine Erhöhung der Menge an benutzter Drop-Cast-Lösung ist mit einer Zunahme der Farbstoffdichte im SURMOF und einer verbesserten Emissionseffizienz verbunden.

In dieser Arbeit wurde H_4ETTC geladenes SURMOF aus einer anwendungsorientierten Perspektive untersucht, wobei die Tintenstrahldrucktechnik mit der AIE-Beladung eines SURMOFs kombiniert wurde und als erster Schritt zur Etablierung eines Displays basierend auf SURMOFs mit einer Größe von bis zu 70 µm dient. Eine weitere Anwendung, die untersucht wurde, ist ein auf SURMOFs basierender lumineszierender Sonnenkonzentrator, bei dem SURMOFs auf einer großen Fläche (25 cm^2) abgeschieden und mit größt möglicher Dichte mit einem Farbstoff beladen wurden, um eine hohe Absorption und eine hohe Emissionseffizienz zu erreichen. Die Leistung des Geräts wurde untersucht, indem eine Solarzelle an einer Kante angebracht und der Gesamtwirkungsgrad des Systems berechnet wurde. Das System zeigte einen geringeren Wirkungsgrad im Vergleich zu einem Standard-Bulk-LSC. Obwohl die Ergebnisse dieser Arbeit einen Fortschritt in den SURMOF-Anwendungen darstellen, müssen zukünftige Verbesserungen erreicht werden. AIE-Moleküle mit dem gleichen Kern des H_4ETTC-Farbstoffs können eine breitere Absorption und eine rotverschobene Emission bewirken, um verschiedene Displayfarben zu erhalten.

Abstract

Luminescent materials, also known as phosphors, that emit light after optical excitation have many applications such as in lighting, displays, object tagging (i.e. for microscopy), and energy conversion. Traditionally phosphors can be broken into categories of inorganic versus organic materials, and those that emit fluorescence versus phosphorescence. Commonly, the definition of a phosphorescent implies that its luminescence has a decay time greater than 1 ms whereas a fluorescent material's decay time is shorter (in the case of organic phosphors the definition is more rigorous: luminescence being emission from a singlet excited state, and phosphorescence being that from a triplet excited state). Thus, fluorescent materials are usually sought for efficient light emission, but phosphorescent materials are interesting in applications wherein the persistence of their emission can be of use. Inorganic phosphors are usually crystalline host materials doped with transition or rare earth metals in order to activate luminescence. The most common host materials are called garnets, which have the chemical formula $A_3B_5O_{12}$, where A and B are two different elements, and O is oxygen. Some examples of optically active rare earth are cerium used for generating white-light, neodymium already used in the laser and erbium used in the optical amplifier.

Advantages of organic phosphors include their strong absorption cross-sections, and wide tunability. With the commercialization of organic light emitting diodes, the interest in organic phosphors is at a maximum. They are also used for applications in energy conversion, such as luminescent solar concentrators.

Normally, organic phosphors are amorphous blends of small molecules and polymers. This makes it difficult to engineer interactions between the host organic material and the organic 'activator' chromophores. One way of controlling these aspects was to load organic chromophores into porous inorganic hosts, such as zeolites. However, in recent years a new class of nanoporous hybrid material, metal-organic frameworks (MOFs), has been synthesized. MOFs combine the interesting qualities from both inorganic and organic porous materials such as well-defined and ordered pores and synthesis versatility. In this thesis, methods for loading luminescent guest chromophores into a specific type of MOF, deposited in a thin-film configuration onto a substrate has been developed and studied (called surface anchored metal-organic frameworks (SURMOF). ZnBDC SURMOF, composed by zinc and bi-carboxylate benzene, as inorganic and organic components respectively, has been investigated and shown that flat molecules can be introduced between the sheet-like planes of this SURMOF.

Chromophore molecules incorporation has been performed via drop-casting of dye solution directly on the SURMOF. The basic parameters for the guest molecule loading have been studied using metallated porphyrins molecules, establishing that the presence of carboxylic groups is a crucial factor for a successful loading. Dye loading has been investigated in detail through time-of-flight secondary-ion mass spectroscopy (ToF-SIMS), which provides a depth profile of the compositions of the loaded samples, showing a uniform loading of the SURMOF throughout all its depth. The same loading approach has been applied on 4',4''',4'''',4'''''''-(ethene-1,1,2,2-tetrayl)tetrakis-(([1,1'-biphenyl]-3-carboxylic acid)) (H_4ETTC), an aggregation-induced emission (AIE) dye, which exhibits an enhanced emission when incorporated in the SURMOF scaffold, due to restriction of molecular motion. A further increase of drop-casted solution is associated to an increase of dye density inside the SURMOF and an improved emission efficiency.

In this work, H_4ETTC loaded SURMOF has been studied from a device prospective, combining the ink-jet printing technique with the AIE loading in SURMOF and achieving features size down to 70 µm as a first step to establish a display made by SURMOF. An additional application which has been explored is a SURMOF based luminescent solar concentrator , where SURMOF has been deposited on a large area (25 cm^2) and incorporated with the highest density of dyes in order to achieve a high absorption and a high emission efficiency. The performance of the device has been studied, attaching a solar cell on one edge and

calculating the overall efficiency of the system. The system revealed a lower efficiency compared with a standard bulk LSC. Despite the results of this work constitute an advancement in the SURMOF applications, future improvements need to be achieved. AIE molecules with the same core of H_4ETTC dye can provide a broader absorption and a red-shifted emission in order to obtain different display colors.

Acknowledgments

First, I would like to thank Prof. Dr. Bryce S. Richards for the opportunity to pursue the Ph.D. in his multicultural group. For his guide through the years of the Ph.D., continuous advice and for his enormous patience in waiting for my thesis, which takes more than a dugong pregnancy[1] to be delivered.

Special thanks go to Dr. Ian A. Howard, a supervisor, and a friend. The one that always believed, even more than me, in my research and work.

Many thanks go to my colleagues that made the days of the Ph.D. special and full of happiness.

My office mates Michael A. and Sheying, who shared with me laughs, food, and culture. I think I would have never came out from the Ph.D. with my mental sanity intact without you two guys. Michael Oldenburg my beloved Luigi! Who shared with me the burden of the SURMOF. Stephan the alfa and omega: who provided me a rooftop on my head at the beginning and help me with thesis submission at the end. Marius I promise we will watch a better football match of Italy together in the future, maybe we will not fall asleep.

I want to thank as well people from IFG: Prof Dr. Christof Wöll, Dr. Peter Weidler, Dr. Stefan Heisler, Dr. Alexander Well, Dr. Ritesh Haldar who shared with me their knowledge and facilities.

Special thanks go to Prof. Dr. Natalia B. Shustova and to the people of the University of South Carolina who lighted in me the spark of synthetic chemistry and made me regrets (a little bit) for haven't chosen chemistry at the beginning of my bachelor.

I want to thank Karlsruhe School of Optics and Photonics (KSOP) for founding my scholarship for the first two years of my Ph.D. and Karlsruhe House of Young Scientist (KHYS) for founding my research abroad in the USA.

Un ringraziamento particolare va ai miei genitori che mi hanno sempre supportato in questo cammino anche quando sembrava essere troppo dura. Un grazie ad Elisa amore mio. Un grazie a Lollo, Vitto ed Ila amici di una vita che ho sempre sentito vicino nonostante gli 800 km di distanza. Un grazie a Simone ed Alessia che con i weekends passati ad Heidleber e Gissen hanno reso i primi momenti più spensierati.

Grazie a tutti belli e brutti!

[1]https://www.nationalgeographic.com/animals/mammals/d/dugong/

List of publications

Peer-Reviewed Journals

N. Baroni, A. Turshatov, M.l Adams, E. A. Dolgopolova, S. Schlisske, G. H. Sosa, C. Wöll, N. B. Shustova, B. S. Richards and I. A. Howard. *Inkjet-Printed Photoluminescent Patterns of Aggregation-Induced-Emission Chromophores on Surface-Anchored Metal-Organic Frameworks. ACS* Applied Materials & Interfaces**,** 2018

N. Baroni, A. Turshatov, M. Oldenburg, D. Busko, M. Adams, R. Haldar, A. Welle, E. Redel, C. Wöll, B. S. Richards, I. A. Howard. *Facile loading of thin-film surface-anchored metal-organic frameworks with Lewis-base guest molecules*. Mater. Chem. Front., 2017,1, 1888-1894.

M. Adams, **N. Baroni,** M. Oldenburg, F. Kraffert,, J. Behrends, , R. W. MacQueen, R. Haldar, D. Busko, A. Turshatov, G. Emandi, M. O. Senge, C. Wöll, Lips, K., Richards, B. S. & Howard, I. A. *Reaction of porphyrin-based surface-anchored metal-organic frameworks caused by prolonged illumination*. Physical Chemistry Chemical Physics, 2018, **20**, 29142–29151.

M. Adams, M. Kozlowska, **N. Baroni**, M. Oldenburg, , R. Ma, D. Busko, A. Turshatov, G. Emandi, M. Senge, O., R. Haldar, C. Wöll, G. U. Nienhaus, B. S. Richards & I. A. Howard, *Highly Efficient One-Dimensional Triplet Exciton Transport in a Palladium–Porphyrin-Based Surface-Anchored Metal–OrganicFramework.* ACS Applied Materials & Interfaces, **11**, 15688–15697.

M. Oldenburg, A. Turshatov, D. Busko, S. Wollgarten, M. Adams, **N. Baroni**, A. Welle, E. Redel, C. Wöll, B. S. Richards and I.A. Howard. *Photon Upconversion at Crystalline Organic–Organic Heterojunctions.* Adv. Mater., 2016, 28: 8477–8482.

Conference contribution

N. Baroni, M. Oldenburg, A. Turshatov, C. Wöll, I. A. Howard and B. S. Richards. *Surface-anchored metal organic frameworks (SURMOFs) for optical applications: our forays into dye-loading, up-conversion, and dipolar rotors.* Symposium - Design, characterization and facilitating technologies for porous materials -Graz - February 2017- oral presentation

N. Baroni, A. Turshatov, M. Oldenburg, D. Busko, M. Adams, A. Welle, E. Redel, C. Wöll, B. S. Richards and I. A. Howard. *Post-Synthetic Loading of Luminescent Guest Molecules in Surface-Anchored Metal Organic Frameworks.* AMN8, 12 - 16 February 2017 - Queenstown, New Zealand -Poster

N. Baroni, I.A. Howard, A. Turshatov, M. Oldenburg, E. Redel, C. Wöll and B. S. Richards*. Surface anchored metal organic framework (SURMOF) for directed light emission*. DPG-Regensburg, Germany, march 2016. Oral presentation.

List of Acronyms

AIE	aggregation-induced emission
BDC	bicarboxylatebenzene
$CDCl_3$	deuterated chloroform
DMSO	dimethyl sulfoxide
DTA	dithioterephtalic acid
DXP	N,N-bis(2,6-dimethylphenyl)-3,4:9,10-perylene tetracarboxylic diimide
FRET	Foster resonance energy transfer
e-PLQY	external photoluminescence quantum yield
LED	light-emitting diode
H_4ETTC	4’,4’’’,4’’’’’,4’’’’’’’-(Ethene-1,1,2,2-tetrayl)tetrakis-(([1,1’-biphenyl]-3-carboxylic acid))
HNMR	Proton nuclear magnetic resonance
IPA	isophtalic acid
i-PLQY	internal photoluminescence quantum yield
LSC	luminescent solar concentrator
LMCT	ligand to metal charge transfer
Me_4ETTC	tetramethyl4’,4’’’,4’’’’’,4’’’’’’’-(ethene-1,1,2,2-tetrayl)tetrakis([1,1’-biphenyl]-4-carboxylate)
MeOH	methanol
MLCT	metal to ligand charge transfer
MHDA	16-mercaptohexadecanoic acid
MOF	metal-organic framework
MUD	11-mercapto-1-undecanol
OLED	organic light-emitting diode
OPO	optical parametric oscillator
PLQY	photoluminescence quantum yield
PSM	post-synthetic modification
PV	photovoltaic
RIM	restriction of intermolecular motion
RIR	restriction intermolecular rotation
RIV	restriction of intermolecular vibration

RTP	room-temperature phosphorescence
SAM	self-assembled monolayer
SURMOF	surface-anchored metal-organic framework
ToF-SIMS	time of flight secondary ion mass spectroscopy
TRPL	Time resolved photoluminescence
TPE	tetraphenylethene
TPE-Br	Tetrakis(4-bromophenyl)ethane
WC	wavelength converter
XRD	X-ray diffractometry

Chapter 1: Introduction

1.1 Motivation

Porous materials can be classified according to their composition. Pure inorganic compounds such as zeolites, which are composed of silicon, aluminum, and oxygen, are crystalline material characterized by well-defined pores but with a low versatility in the synthesis. Differently, pure organic materials such as organic polymers are characterized by an high versatility, though with different dimensions and disordered pores [1]. In 1999, Yaghi *et al.* [2] have defined, for the first time, a new class of porous materials named metal-organic frameworks (MOFs). MOFs are hybrid materials constituted by metal ion clusters connected with organic linkers, which combine the ordered and the rational design of inorganic compound with the synthetic versatility of the organic compound [1]. MOF pores can be tuned from 1 nm to 10 nm with a high degree of definition. Furthermore, MOFs can acquire novel properties with the exchanging of the metal ion or the organic linker or by the loading of guest molecules within their pores [1].
In this work, in order to have a device-driven approach, it has been preferred to work with MOFs that can be grown on a substrate, using a thin-film configuration. A Layer-by-layer deposition has been performed, to grow MOFs in a thin-film fashion on different kinds of substrates, defining an innovative kind of material called surface anchored metal organic frameworks (SURMOFs). SURMOFs maintain the higher degree of crystallinity of the MOF with well-defined pores [3].

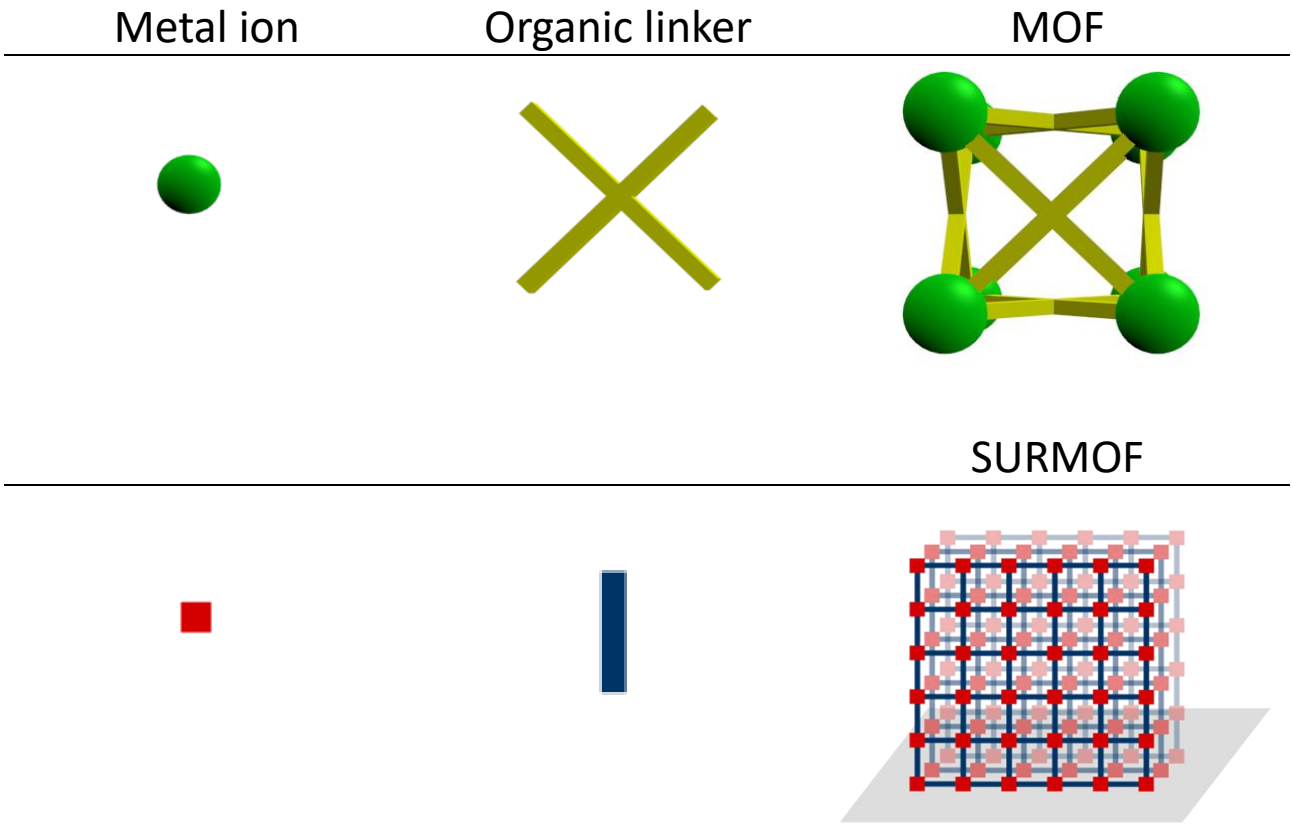

Figure 1.1: schematic representation of MOF and SURMOF structures and their constituents: metal ion and organic linker. SURMOF structure is represented deposited on a substrate (in grey) while MOF structure is free standing in a powder form.

As for the MOF, the SURMOF characteristics can be tuned with the modification of metal ion and organic linker or via a guest molecule loading. In this work, the guest-molecule loading approach has been chosen over the other two due to the fact that the choice of loaded molecules are not restricted by structural requirements as for the metal ion and the organic linker [4].

The focus of the present thesis is the investigation of SURMOFs and their usage for different optical applications. First, the chromophore loading into SURMOF has been fundamentally investigated, establishing criteria for dyes that allow SURMOFs to be loaded easily with solution-based approaches including ink-jet printing. The first candidate of this investigation is a porphyrin dyes, ideally suited as initial candidates to establish how intercalation can occur in these systems. Then it is demonstrated that the technique can be extended to load aggregation induced emission chromophores that are much more efficient in the solid-state. Thus loaded SURMOFs could be developed towards potential optical applications such as luminescent down-shifting (for lighting and display technologies), and luminescent solar concentrators (LSC).

In the field of light technologies and illumination, light-emitting diode (LED) is one of the most common device. LEDs are based on direct bandgap semiconductors doped in order to induce the formation of a p-n junction, which, under forward bias, is dominated by the recombination current. Electrons and holes are injected into the p-n junction, and recombine in the depletion region, providing light emission. Emission of LEDs highly depends on the band-gap of the semiconductor and emit in a narrow wavelengths range. For lighting purposes broadband, 'white', light emission is desired, therefore two approaches can be used to increase the spectral bandwidth of LEDs. In the first one, the white light source is produced by a sum of LEDs and the LEDs spectra are mixed to obtain white light emission. LEDs in dichromatic, trichromatic or tetrachromatic configuration have, respectively, an emission generated by two LEDs (blue and yellow), three LEDs (blue, green and red), and four LEDs (blue, cyan, green and red), as shown in Figure 1.2 [5].

In the second approach, a wavelength converter (WC), which could be a dye or phosphor, is applied inside LED encapsulation. Therefore, the LED light is used to excite one or more WCs and in order to obtain an emerging light, which is the sum of LEDs emission and WC emission. In this approach, it can be identified as well as dichromatic configuration with the emission a yellow WC emitter combined with a blue LED, a trichromatic configuration with three WCs excited by an UV LED, and tetrachromic configuration with four WCs excited by UV LED, as shown in Figure 1.2 [5].

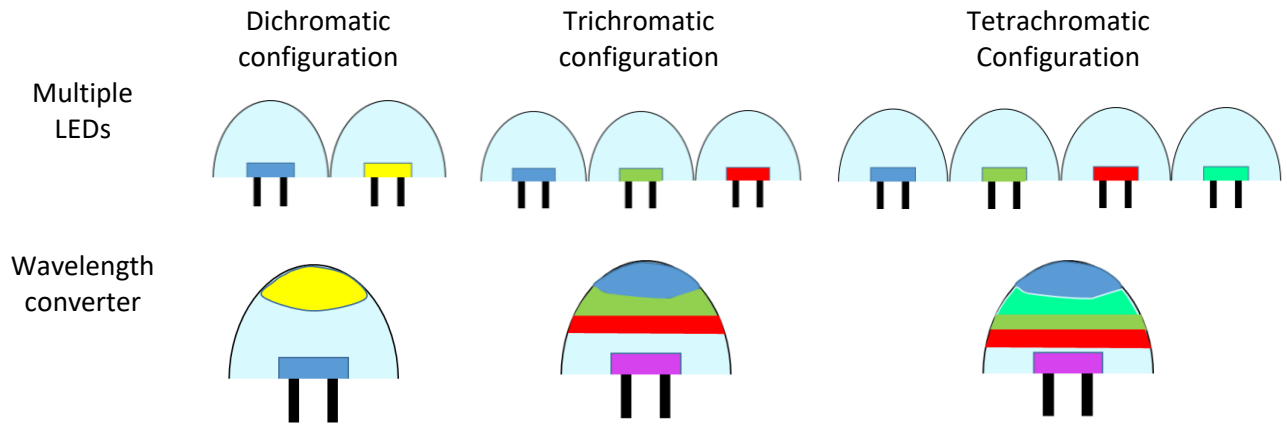

Figure 1.2: schematic representation of dichromatic, trichromatic and tetrachromatic configuration in the two approaches: multiple LEDs (top) and wavelength converter (bottom) to provide white light emission.

Focusing on the second approach, an ideal WC would be a material, which can be deposited easily as thin film on the different shapes of LED with a high concentration of optically active material to guarantee a high absorption and with a high light emission efficiency. Therefore, SURMOF has been investigated as host material for WC chromophores in detail. SURMOF loaded with aggregation-induced emission dyes will provide a high density of loading with a good emission efficiency. The possibility to localize chromophores inside the SURMOF is studied as well and it is critical in order to design wavelength converter, which can acts as display as well.

A second application is the development of a SURMOF based Luminescent solar concentrators (LSCs) [6]. LSCs are one of the most promising technologies in the field of the non-imaging concentrating photovoltaic (CPV) systems. LSCs are typically formed by slabs of transparent material doped with luminescent dyes and equipped with small arrays of photovoltaic cells (PV). In LSC, the light that hits the surface is absorbed by the dyes and re-emitted isotropically at longer wavelength. The light is collected via total internal reflection (TIR), due to the difference in the refractive index (n) between air and host material, to the edges of the slab where is harvested by PV cells, as shown in Figure 1.3 a.

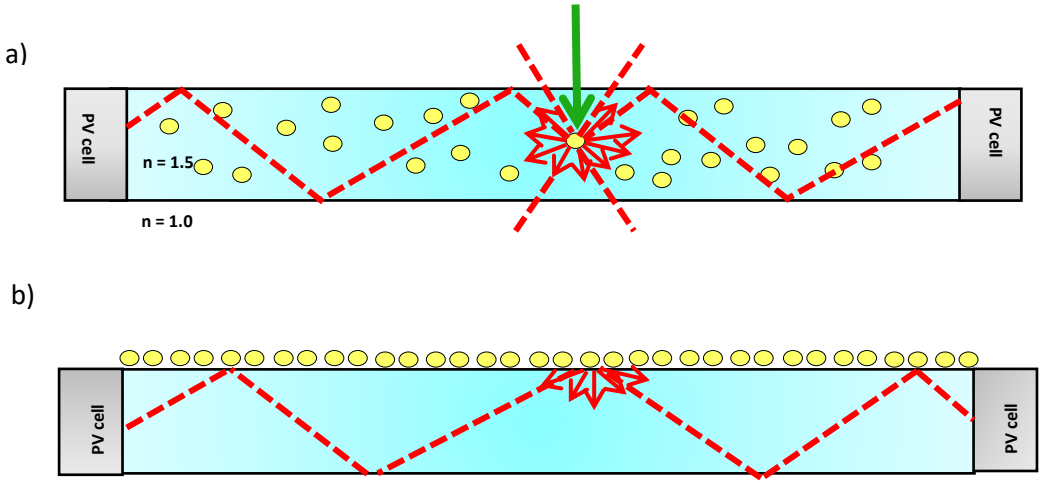

Figure 1.3: Panel a) basic configuration and working principle of a bulk LSC. The host material (in light blue), the fluorophores (in yellow) and the photovoltaic solar cell (in grey). The incident light (green arrow) is absorbed by the fluorophore and re-emitted isotopically with a longer wavelength (red arrows). Then light is total internal reflected and then collected to the edges (dotted red lines). Panel b) basic configuration of thin-film LSC, the dyes are deposited on the surface as a thin-film.

LSCs show several advantages with respect to CPV: they can convert the diffuse radiation, are compatible with large-area and low-cost manufacturing process, do not need a solar tracker, and are lighter than traditional Si panel. For these reasons, LSC can be easily integrated into architecture and constitute an encouraging technology for solar concentration [7]. Another design of LSC is with luminescent dyes deposited as a thin film on the top of the waveguide, as shown in Figure 1.3 b. In this configuration, a higher concentration of dye is needed to have the same absorption of the bulk LSC. For this system, the SURMOF can be deposited directly on top of the transparent slab and loaded with luminescent molecules. Aggregation-induced emission dye has been chosen as chromophore in order to achieve a high concentration of dye and a high absorption avoiding the emission quenching [8].

1.2 Fundamentals of absorption and emission in organic fluorophores

In this section, the basic principles of absorption and emission of light in organic fluorophores and how the environment affects their behavior are described.

1.2.1 Absorption

The light absorption by a molecule can be described following a classical or a quantum mechanical approach.

Classical approach:

In the classical approach, the force bounds the electrons to the nuclei can be considered as a spring; the electric field induces a dipole in the molecule, then the generated charges start oscillating and, due to the frictional forces, are dumped. The system can be approximated with three different elements:

- The light as an oscillating electromagnetic field.
- The molecule as a harmonic oscillator.
- The interaction between the light and the molecule as an oscillating external force driving the oscillator.

The forces equation of the system is

$$F_{inertia} = F_{E.M} + F_{spring} + F_{damping}. \tag{1.1}$$

Where the forces are explicated:

$$m\ddot{x} = \hat{\varepsilon}\frac{e}{m}\, E_0 e^{-i(\omega t - kz)} - k_s x - b\dot{x}, \tag{1.2}$$

In Equation 1.2, the term $\hat{\varepsilon}\frac{e}{m}\, E_0 e^{-i(\omega t - kz)}$is the electric field force with e the electron charge, m the electron mass, ω the forcing frequency. The term $-k_s x$ is the elastic force, with k_s the spring constant, that is opposed to the displacement induced by the electric field and $-b\dot{x}$ is the damping force, with b as the damping coefficient, which reduces the oscillation.
Equation 1.2 is a second order inhomogeneous linear differential equation, where the solution is the sum of the general solution of the corresponding homogeneous equation $g(t)$ plus a particular solution of the inhomogeneous $p(t)$.

$$x(t) = g(t) + p(t), \tag{1.3}$$

$$g(t) = (Acos(\omega_0^2 - \beta^2)^{\frac{1}{2}}t + Bsin(\omega_0^2 - \beta^2)^{\frac{1}{2}}t)e^{-\beta t}, \tag{1.4}$$

With $\omega_0 = \sqrt{k_s/m}$ and $\beta = b/2m$

$$p(t) = Re\left(\frac{\hat{e}\left(\frac{e}{m}\right)E_0 e^{-i(\omega t - kz)}}{\omega_0^2 - \omega^2 - 2i\beta\omega}\right). \tag{1.5}$$

In Equation 1.5, only the real part of the solution is taken into account since it is the only term with a physical meaning. Three kinds of oscillator are present: i) the overdamped oscillator, which has a high spring constant and has almost no oscillation; ii) the critically-damped oscillator, which, after the excitation, it returns to the equilibrium and iii) the underdamped-oscillator, which exhibits an oscillation that decays with time.

Only the underdamped oscillator is considered as the most frequent case [9], which brings to a $\beta \ll \omega_0$. Making an approximation of $t \gg 1/\beta$. $1/\beta$ is defined as the damping time, which is small with respect to the periods of oscillation of the system $T_0 = 2\pi/\omega_0$ and $T = 2\pi/\omega$ with $\omega_0, \omega \gg \beta$. The approximation brings the exponential of the homogeneous solution to be $e^{-\beta t} \ll 1$ and neglecting the homogenous term from the moment it is small. The absorption can be calculated via the absorbed power *P*

$$P = \frac{dW}{dt} = F_{E.M.}\frac{dx}{dt} = \left(\frac{\left(\frac{e^2}{m}\right){E_0}^2\beta^2\omega^2}{({\omega_0}^2 - \omega^2)^2 + 4\beta^2\omega^2}\right), \tag{1.6}$$

For the previous condition $\beta \ll \omega_0, \omega$, defined as the absorbed power is low unless $\omega = \omega_0$. Therefore, light is absorbed only at the resonance frequency ω_0 that is characteristic for every molecular system.

Quantum mechanics approach

Light absorbed by a molecule with sufficient energy to promote an electron from the highest occupied molecular orbital (HOMO) to the lowest unoccupied molecular orbital (LUMO). In terms of energy, the molecule goes from a ground state S_0 to an excited state called S_n. To understand the light absorption by a molecule, the total molecular wavefunction needs to be considered and can be expressed as the product of two components:

$$\Psi_{total} = \Psi_{spatial}\Psi_{spin}, \tag{1.7}$$

Where, Ψ_{spin} is the spin wavefunction, which represents the individual spin wavefunctions of the electrons;$\Psi_{spatial}$ is the spatial wavefunction and depends on the electrons position in the molecule (r_i) and the nuclei positions (R_i), In order to make explicit these dependences the spatial wavefunction can be written as $\Psi_{spatial}(R_i; r_i)$. During molecule absorption and emission, nuclei move relatively slowly with respect to the electron, due to their mass, therefore the interaction between these two components can be considered low. In this condition, the system is regulated by the Frank-Condon principle [10] and can be approximated by the Born-Oppenheimer approximation, expressing the spatial wavefunction as the product of a nuclei wavefunction (Ψ_{nuclei}) and an electronic wavefunction (Ψ_{el}). Since the nuclei are not fixed but vibrate along an equilibrium position with a frequency ω, $\Psi_{nuclei} = \Psi_{vib}$and as a consequence the spatial wavefunction can be written as:

$$\Psi_{spatial} = \Psi_{el}(R_i; r_i)\Psi_{vib}(R_i), \tag{1.8}$$

Then Ψ_{total} can be re-written as:

$$\Psi_{total} = \Psi_{el}\Psi_{vib}\Psi_{spin}. \tag{1.9}$$

Assuming no significant interaction between the single electron wavefunctions (Ψ_i), the total electron wavefunction Ψ_{el} can be approximated as the product of the single electron wavefunctions

$$\Psi_{el} = \prod_i \Psi_i, \tag{1.10}$$

Ψ_i can be written as a linear combination of the atomic wavefunctions of the electrons ϕ_j

$$\Psi_i = \sum_j c_j \phi_j. \tag{1.11}$$

The intensity of light absorbed by a molecule I is proportional to the number of photons (n) absorbed per second $k_{abs} = \frac{dn}{dt}$. The light absorption can be approximated as an increase of the molecular energy. In the Hamiltonian of the molecule, the increase in energy can be expressed by term (H') added to the Hamiltonian of the molecule before the light absorption (H_0). To express the light perturbation interaction with the molecule the dipole operator $e\hat{\boldsymbol{r}}$ is adopted.

$$H = H_0 + H' = H_0 + e\hat{\boldsymbol{r}}. \tag{1.12}$$

When $e\hat{\boldsymbol{r}}$ is small compared to the original Hamiltonian, then it is reasonable to consider also the eigenvalues and the wavefunctions changed by a small quantity and calculate them using perturbation theory. The transition rate k_{if} can be defined as for transition from an initial state Ψ_i to a final stateΨ_f. Applying the *Fermi's golden rule,* k_{if} can be written:

$$k_{if} = \frac{2\pi}{\hbar} \left| \langle \Psi_f | H' | \Psi_i \rangle \right|^2 \rho, \tag{1.13}$$

With ρ the density of final states. Using Equation 1.9 for the wavefunction and the Equation 1.12 for the dipole operator a k_{if} is obtained as

$$k_{if} = \frac{2\pi}{\hbar} \left| \langle \Psi_{el,f} \Psi_{vib,f} \Psi_{spin,f} | e\hat{\boldsymbol{r}} | \Psi_{el,i} \Psi_{vib,i} \Psi_{spin,i} \rangle \right|^2 \rho. \tag{1.14}$$

The electromagnetic field of light induces an oscillation on the molecule electrons with no effects on the nuclei, which are too heavy to be influenced, and on the spin. Then the dipole operator acts only on the electronic wavefunction.

$$k_{if} = \frac{2\pi}{\hbar} \left| \langle \Psi_{el,f} | e\hat{\boldsymbol{r}} | \Psi_{el,i} \rangle \right|^2 \left| \langle \Psi_{vib,f} | \Psi_{vib,i} \rangle \right|^2 \left| \langle \Psi_{spin,f} | \Psi_{spin,i} \rangle \right|^2 \rho, \tag{1.15}$$

In the term$\langle \Psi_{el,f} | e\hat{\boldsymbol{r}} | \Psi_{el,i} \rangle$, the dipole operator ($e\hat{\boldsymbol{r}}$) is odd under spatial inversion and in order to obtain a non-zero integral the parity of the initial state should be different from the one of the final state. If the integral is equal to zero then the transition between states is dipole-forbidden while if non-zero the transition is dipole-allowed. The integral value depends on two factors: the overlap integral between the initial state wavefunction and final state wavefunction and the value of the dipole moment of the molecule related to the two states.

The term$\left| \langle \Psi_{vib,f} | \Psi_{vib,i} \rangle \right|^2$ indicates the probability to have the transition from the 0th ground state to the mth of an excited state. The vibrational factor $\langle \Psi_{vib,f} | \Psi_{vib,i} \rangle$ controls the shape of the absorption and emission spectrum. Absorption and emission spectrum changes depending on the rigidity of the molecule. If the molecule has rigid bonds there is transitions from vibrational 0th level, while when the molecule is flexible, other vibrational levels are active, as shown in Figure 1.4. The intensity of the transition is the overlap integral of the vibration wavefunctions called Franck–Condon-factor.

$$I_{0\to m} = \left|\langle \Psi_{vib,f} | \Psi_{vib,i} \rangle\right|^2 = \frac{S^m}{m!} e^{-S}, \tag{1.16}$$

With *S* named Huang–Rhys-parameter defined as:

$$S = \frac{1}{2} M \omega_m \frac{\Delta Q^2}{\hbar}, \tag{1.17}$$

Where M is the reduced mass, ω_m is the angular frequency and, ΔQ is the variation in the equilibrium in configuration coordinate due to the fact that the electromagnetic field induces a change in the position of the electrons but not in the nuclei, inducing a change in a larger equilibrium distance.

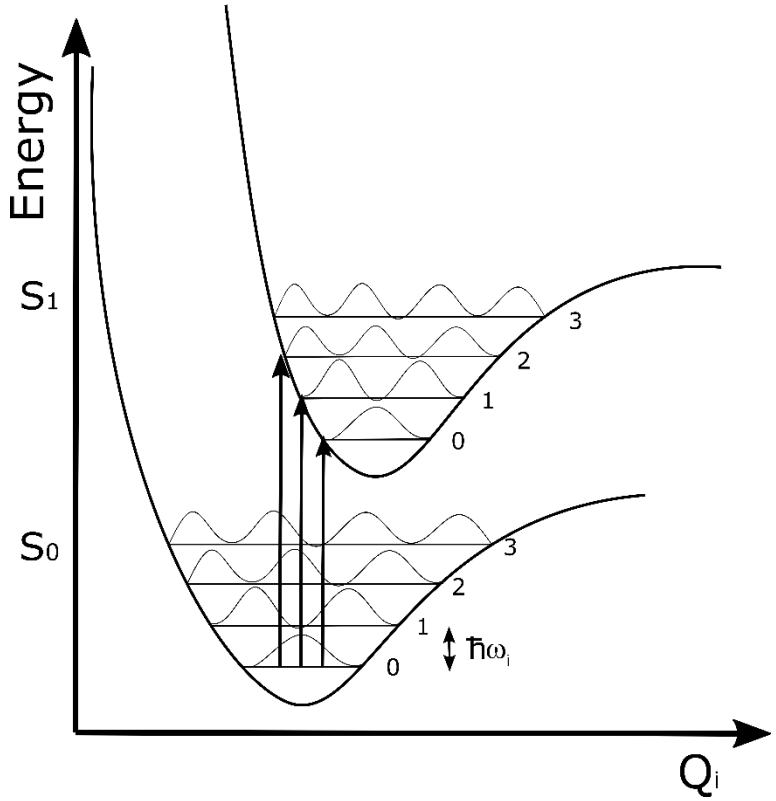

Figure 1.4: potential energy curves of ground state and of first excited state with vibrational energy wavefunctions. Absorbed light can excite a molecule from a 0th vibrational ground state to the nth first excited state.

$\langle \Psi_{spin,f} | \Psi_{spin,i} \rangle$ is the spin factor that can assumes only two values: 0 or 1. The first value (0) is obtained when the two spins are unpaired, as one singlet and one triplet, while the second value (1) is for a transition from states with the same spin. Therefore, the transition are called spin-forbidden or spin-allowed, respectively. Absorption from the ground state takes place only to another singlet excited state.

A high absorption rate between two energy states is positively influenced if the two states have the same parity, same spin and a good overlap of π-electrons.

In order to have efficient photoemission, the limit on the wavelength range, in which useful absorption can take place, is approximately from 200 nm to 1000 nm. The lower limit is given by the ionization energy of the molecule. The light below 200 nm has enough energy to ionize the molecule. A fluorophore, which absorbs light below 200 nm, is decomposed by the light. On the other side, the upper limit of absorption is a consequence of the small difference between the excited and ground state which brings to a high probability to lose the excitation via a non-radiative decay [11]. This behavior indicates the most relevant absorption by fluorophores is accounted for by $n \rightarrow \pi^*$ and $\pi \rightarrow \pi^*$ molecular transitions, which have energies corresponding to photon wavelengths between 200 nm and 1000 nm.

1.2.2 Emission

After the photon absorption, the de-excitation, towards the ground state, can occurred via several pathways, as shown in Figure 1.5.

Internal conversion: the excitation is released via a non-radiative decay between two states with the same spin. Internal conversion is more efficient if the energy difference between the two states is small, i.e. the internal conversion is more probable between two excited states, as S_2 and S_1, rather than an excited state and the ground state, as S_1 and S_0. When a photon is absorbed by the molecule, which is promoted to an excited state higher than the zeroth vibrational order of the first excited state S_1. *Vibrational relaxation* brings the electron to the zeroth-order vibrational level of the excited state, and then the internal conversion will bring it to the first excited state. For this reason, the emission spectrum of a molecule is independent of the excitation source. This is summarized in Kasha's rule, which states spontaneous emission of a photon, therefore, occurs almost exclusively from the lowest excited state of a given multiplicity.

Fluorescence: the excitation is released via a radiative transition from the first excited state S_1 to the ground state S_0. The fluorescence spectrum is red-shifted for the absorption due to vibrational relaxation and thus, energy loss. The difference between the peak of absorption and peak of emission is defined as Stokes shift. In molecules where the Stoke shift is small, there is an overlap of absorption and emission spectrum, which brings to a higher probability of re-absorption where the light emitted by a molecule is re-absorbed by the molecule itself [12].

Intersystem crossing: is a non-radiative transition between two vibrational states with the same energy but different spin. The energy transfer between two states with unpaired spins is usually forbidden, although it is allowed in presence of a perturbation provided by the spin-orbit coupling. In the optical transition, the total angular momentum (J), defined, as the sum of the spin angular momentum (s) and orbital angular momentum (l), needs to be conserved. In order to have an intersystem crossing, if the spin angular momentum is changing, the orbital angular momentum have to change as well. Therefore, the spin-orbit perturbation is proportional to the fourth power of the atomic charge, and there is strong spin-orbit coupling and as a consequence high probability of intersystem crossing if a heavy atom is present in the molecule.

Phosphorescence: In phosphorescence, the excitation is transferred into a triplet state (T_1) via the *intersystem crossing* after reaching the first excited singlet state (S_1). The light is emitted from T_1 to the ground state S_0 and it is in competition with intersystem crossing between the two states. Temperature affects the phosphorescence rate, enhancing *vibrational relaxation* that increases the probability of intersystem crossing. The probability of intersystem crossing increases with the decreasing of the temperature. However, examples of efficient phosphorescence at room temperature, defined Room temperature phosphorescence (RTP), can be found. At room temperature and without the aid of a heavy

atom, it is possible to have a good rate of intersystem crossing if the molecule is confined in a rigid configuration that avoids the deactivation via molecular motion (vibration and rotation) [13]. The presence of oxygen is another factor that affects the efficiency of phosphorescence; since oxygen molecules quench the phosphorescence via collision giving an energy transfer channel for the energy in triplet state.

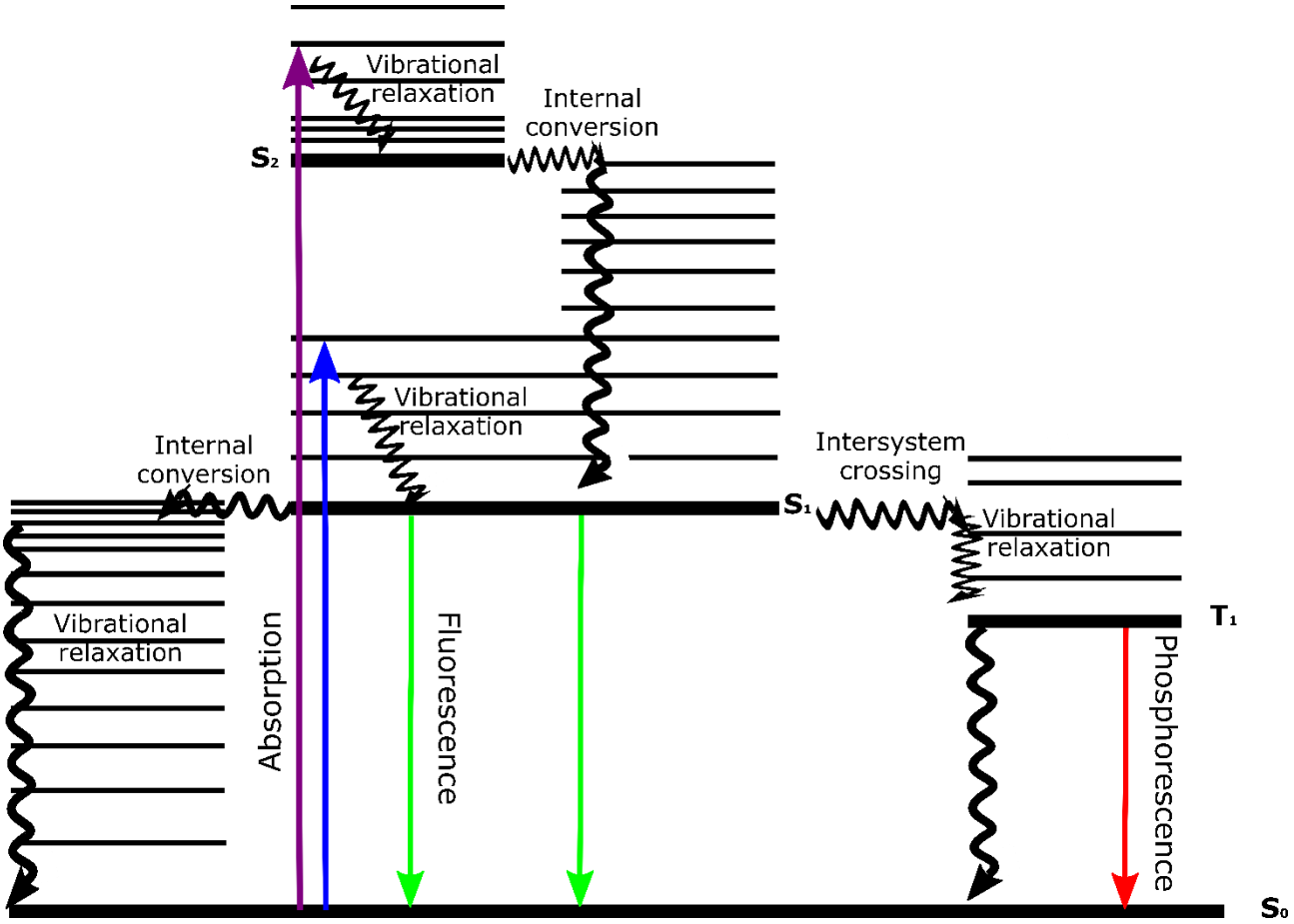

Figure 1.5: three pathways of de-excitation of the absorbed light. On the left side, the de-excitation via non-radiative decay, the excitation goes under internal conversion and then to a vibrational relaxation losing energy via heat. In the center the de-excitation via fluorescence, the excitation reaches the first singlet excited state via vibrational relaxation and then emitted via fluorescence. On the right the de-excitation via phosphorescence, where the excitation is transferred via intersystem crossing from first excited singlet state to the first excited triplet state and then emitted via phosphorescence.

1.2.3 Photoluminescence lifetime

Photoluminescence lifetime is the average value of time that the molecule spends in its excited state. The lifetime of a molecule is determined by the sum of all kinetic constants of de-excitation processes. The population of excited states is described by the rate equation:

$$\frac{dn^*}{dt} = -Kn^*(t) + f(t), \tag{1.18}$$

Where n^* are the excited states, *K* is kinetic constant of all the de-excitation processes with the unit of measurement of s^{-1} and *f(t)* is a function describing the excitation source in time. Considering Equation 1.18 when the excitation is turned off at t=0.

$$\frac{dn^*}{dt} = -Kn^*(t), \tag{1.19}$$

Re-arranging Equation 1.19, to describe the decrease of the excited states:

$$n^*(t) = n^*(0)e^{-Kt}, \tag{1.20}$$

The lifetime τ is defined as the inverse of the kinetic constant K: $\tau = \frac{1}{K}$. K can be described as the sum of two components, the kinetic constant related to the radiative decay (K_r) and the one related to non-radiative decay (K_{nr}).

$$K = K_r + K_{nr}. \tag{1.21}$$

With this definition of lifetime, it can be differentiated between phenomena of fluorescence and phosphorescence depending on their lifetime. Fluorescence is a faster decay with a lifetime from 1 to 100 of nanoseconds, while phosphorescence, from the moment that involves a spin flipping in the intersystem crossing from the triplet state to singlet ground state, is a slower decay.

1.2.4 Fluorophore aggregation

Most of the real systems are not composed of a single molecule but from a series of molecules. Molecules, which are closed together, have the tendency to form aggregates. Aggregation can influence the absorption and emission properties of the molecules and their lifetime. Aggregation originates from a high concentration of molecules in a solution or in a solvent where they are not soluble.

When two molecules are brought together, the total wavefunction of the ground state can be considered as the product of the two molecular wavefunctions $\Psi_{ground} = \Psi_1\Psi_2$ and the total Hamiltonian as the two-particle Hamiltonians with the terms of the single particles H_1, H_2 and an intermolecular potential expressing the interaction between the two moleculesV_{12}.

$$H = H_1 + H_2 + V_{12}. \tag{1.22}$$

Therefore, the energy of the ground state E_g become:

$$E_g = \langle\Psi_1\Psi_2|H_1 + H_2 + V_{12}|\Psi_1\Psi_2\rangle = E_1 + E_2 + D, \tag{1.23}$$

The term *D*, given by $\langle \Psi_1 \Psi_2 | V_{12} | \Psi_1 \Psi_2 \rangle$, is the van-der-Waals interaction energy and it is negative. *D* depends on the distance between the molecules and the orientations of their dipoles. Therefore, the ground state of the molecules together is lower compared to the ground state of the single molecule. As for the ground state, also the excited is influenced. The wavefunction of the excited state is a linear combination of the two possible configurations of the excited state. If the molecules are identical, the excited state can be reassembled as $\Psi_1^* \Psi_2$ or $\Psi_1 \Psi_2^*$ and the total wavefunction can be written:

$$\Psi_{E\pm} = \frac{1}{\sqrt{2}} (\Psi_1^* \Psi_2 + \Psi_1 \Psi_2^*), \tag{1.24}$$

With a corresponding energy

$$\begin{aligned} E_{excited\,\pm} &= \frac{1}{2} \langle \Psi_1^* \Psi_2 \pm \Psi_1 \Psi_2^* | H_1 + H_2 + V_{12} | \Psi_1^* \Psi_2 \pm \Psi_1 \Psi_2^* \rangle \\ &= E_1^* + E_2 + \langle \Psi_1^* \Psi_2 | V_{12} | \Psi_1^* \Psi_2 \rangle \pm \langle \Psi_1 \Psi_2^* | V_{12} | \Psi_1 \Psi_2^* \rangle \\ &= E_1^* + E_2 + D' \pm \beta, \end{aligned} \tag{1.25}$$

With E_1^* the energy of the first molecule in the excited state (with no influence of the second molecule), E_2 energy of the second molecule in the ground state, D' having the same meaning of *D* in Equation 1.23 as the Van-der-Waals interaction between the two molecules and β the resonance term depends from interaction in the overlap between the charge density of the two molecules. The resonance term also depends on the orientation and on the distance between two molecules. To understand the change in the absorption and emission spectrum, the individual energies of the two molecules and the energy difference between S_1 and S_0.

The difference in energy between the excited state and the ground state of the two molecules has to be taken into account and not only the energies themselves

$$\Delta E_{total} = (E_1^* + E_2 + D' \pm \beta) - (E_1 + E_2 + D) = \Delta E_1 + \Delta D \pm \beta, \tag{1.26}$$

Depending on , three different scenarios are possible. i) For $\beta \approx 0$, it represents the case for a large distance between the molecules and the splitting cannot be resolved. ii) For β finite but smaller respect to the energy of the excited state, a dimer is formed with a splitting of the excited state into two, separated by 2β. The molecules configuration in a dimer are stacked on top of each other tilted of 54.7°. iii) For β large, there is a hanging in the molecules configuration optimize their interaction. For the excimer, the splitting in the excited state is clearly visible in the emission and absorption.

To distinguish the type of excimer is from the angle between the two adjacent molecules (α). If α is higher than 54.7° until 90° the aggregate is defined as H-aggregate, while the one from 0° to 54.7° is defined as J-aggregate as shown in Figure 1.6.

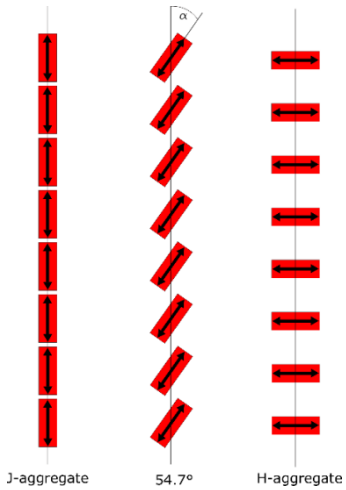

Figure 1.6: classification of molecular aggregates depending on the angle between the neighbor molecules. J-aggregate is defined for an angle 0°≤ α<54.7°, while H-aggregate for an angle 54.7°≤α<90°. The black arrows show the dipole of the molecule.

Assuming the transition dipole moments of two non-interacting molecules defined as $\boldsymbol{\mu_1} = \langle \Psi_1 | e\boldsymbol{r} | \Psi_1{}^* \rangle$ and $\boldsymbol{\mu_2} = \langle \Psi_2 | e\boldsymbol{r} | \Psi_2{}^* \rangle$. For the aggregate, it becomes:

$$\begin{aligned} \mu_{\pm} &= \langle \Psi_G | e\boldsymbol{r} | \Psi_{E\pm} \rangle = \langle \Psi_1 \Psi_2 | e\boldsymbol{r} | \Psi_1{}^* \Psi_2 \pm \Psi_1 \Psi_2{}^* \rangle \\ &= \frac{1}{\sqrt{2}} \langle \Psi_1 \Psi_2 | e\boldsymbol{r} | \Psi_1{}^* \Psi_2 \rangle \pm \langle \Psi_1 \Psi_2 | e\boldsymbol{r} | \Psi_1 \Psi_2{}^* \rangle \\ &= \frac{1}{\sqrt{2}} \boldsymbol{\mu_1} \pm \boldsymbol{\mu_2} \end{aligned} \tag{1.28}$$

In J-aggregate, the E_- state has the parallel dipoles with a total dipole moment of 2μ, while the higher energy state E_+ has the dipoles in anti-parallel configuration with a total dipole moment equal to 0. The consequence on the absorption and emission spectrum is an overall red shifting. Instead, H-aggregate behaves in the opposite way. The higher energy state has the parallel dipole moment and the lower energy state has anti-parallel leading to a blue shifting of the absorption and emission as shown in Figure 1.7.

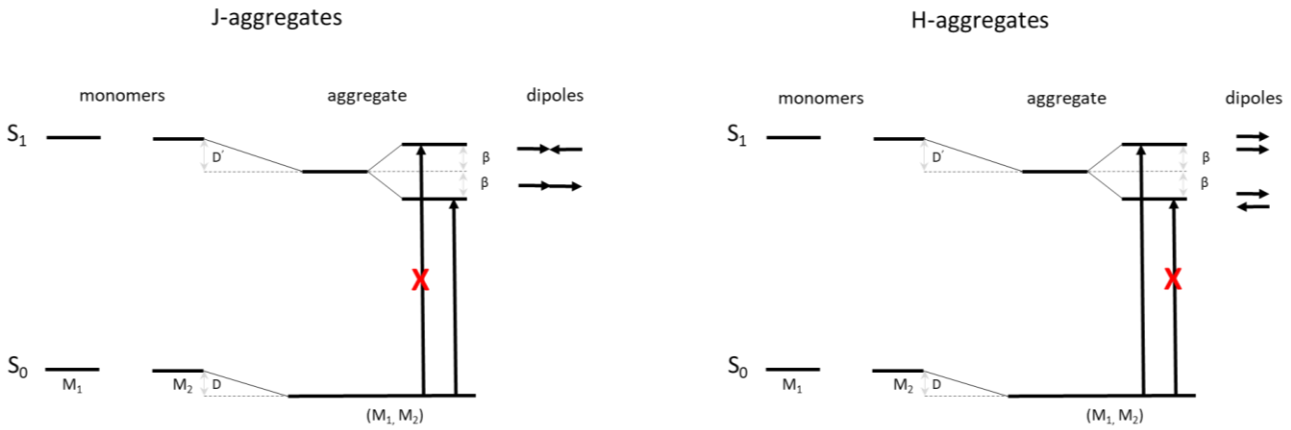

Figure 1.7: energy states in monomers (M_1 and M_2) and in aggregates (M_1M_2) for J- and H- aggregates. The transition with the red x is the forbidden one. *D* and *D'* are the Vander Waals interaction terms for ground state and excited state. β is the resonance term that gives the energy splitting in the excited state of the aggregate.

Furthermore, molecular aggregation affects the emission efficiency of the molecule. The molecular aggregates induced the phenomenon of dynamic quenching, where the energy is transferred to neighborhood molecules with Foster resonance energy transfer (FRET) and then released via non radiative decay [14].

The aggregation effect on a fluorophore photoluminescence lifetime is a shortening of the lifetime due to a quenching on the fluorescence in the aggregates or, more in general, the lifetime is a combination of the single lifetime of the monomer and of the aggregate lifetime.

1.2.5 Aggregation-induced emission dye

Aggregation-induced emission (AIE) is a phenomenon associated to AIE chromophores are characterized by a weak emission in solution that increases in aggregated state, opposed to the behavior of standard dyes. 1-methyl-1,2,3,4,5-pentaphenylsilole has been one of the first AIE dye reported with this behavior. This molecule synthetized by Luo *et al*. in 2001 [15] shows an increase in emitted light when inserted in a thin film compared to its emission in solution. The mechanism behind this behavior is a restriction intermolecular rotation (RIR). In solution, the phenyl rings of the molecule are able to rotate and this motion acts as a non-radiative channel for the molecule excitation. When the molecule is in the aggregate state, the rotational modes are blocked allowing the molecule to emit light in a more efficient way. Further example of a molecule showings AIE via RIR is the tetraphenylethene (TPE), as shown reported in Figure 1.8. In TPE, phenyl rings can are able to rotate or twist around the ethane stator. In solution, TPE has almost no emission with undetectable fluorescence quantum yield, while in solid-state it shows a bright blue light (425 nm) with 24.6 % of fluorescence quantum yield (measured with by a calibrated integrating sphere) [16].

Restriction of intermolecular vibration (RIV) is a different mechanism that switches on the emission of the AIE dye. When a molecule in solution vibrates, its energy is lost via motion, while in solid-state, the motion is restricted and thus the emission is enhanced. An example of this mechanism can be found in the 10,10',11,11'-tetrahydro-5,5'-bidibenzo[a , d] annulenylidene (THBA). THBA is formed by two parts, which can band and vibrate when the molecule is isolated. In aggregate, the motion is blocked, as exemplified in

Figure 1.8 [17]. THBA has a fluorescence quantum yield in solution <0.1% while in solid-state it has a violet emission (380 nm) with 23.0 % fluorescence quantum yield [18].

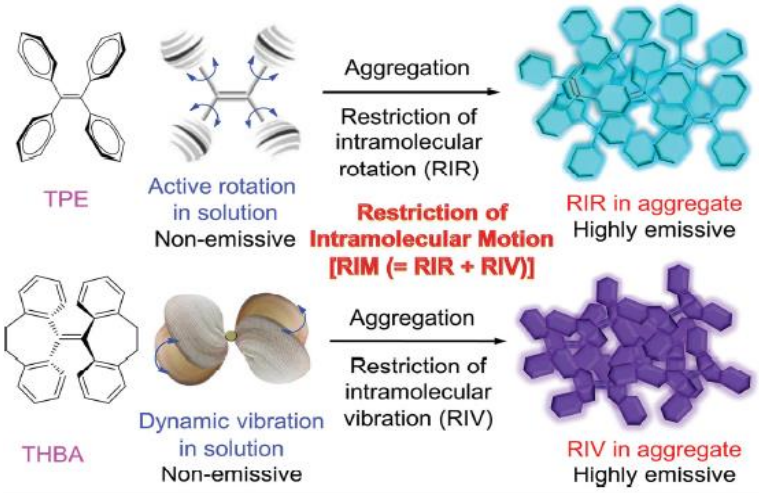

Figure 1.8: two examples of AIE dyes. The TPE molecule in solution shows a weak emission due to rotation of phenyl ring around the ethane stator. In solid-state, the restriction of intramolecular rotation (RIR) increases the efficiency of light emission. THBA molecule loses it excitation energy via vibration. In solid-state the restriction of intramolecular vibration (RIV) switches on the emission. A molecule that shows both rotation and vibration, in solid-state shows restriction of molecular motion (RIM), as the sum of RIR and RIV. Picture reproduced with permission [17].

AIE molecule that loses energy via vibrational and rotational motion, in solid-state presents both RIR and RIV called restriction of intermolecular motion (RIM) [17]. (R)-Diethyl 1,2,3-triphenyl1,2,3,6-tetrahydropyrimidine-4,5-dicarboxylate is a good example where both restrictions act as AIE mechanism [19].

AIE dyes can be applied in the organic light emitting diode (OLED) or in LED. In OLED, AIE dyes are used as an emitting layer to prevent the aggregation induced quenching which can arise in thin film of solid-state dye. A large numbers of AIE dyes are based on the TPE building block, which can provide a variety of different emissions.

In 2012, Huang and coworkers [20] synthesized a series of AIE blue emitters. These AIE chromophores belongs to the family of 4,4'-bis(1,2,2-triphenylvinyl)biphenyl (BTPE) derivatives, which can be considered as a couple of TPE molecules connected in different sites. In Figure 1.9 a, 2,3 ' -bis(1,2,2-triphenylvinyl)biphenyl (oTPE-pTPE) can be found as an example of these dyes, where TPE molecules are connected in *orto* (i.e. the positions of substituents in aromatic compound are 1,2 positions) and *para* (i.e. the positions of substituents in aromatic compound are 1,4 positions) positions. The dye shows no emission in a solution of THF (suitable solvent for the dye), while, the dye shows aggregation when the fraction of water is increased in the solution and its fluorescence quantum yield increases form <0.1% to 34% with an emission peak of 454 nm.

In 2012, Zhao *et al.* produced a TPE-based red emitter constructed on 4,7- di(thiophen-2-yl)benzo-2,1,3-thiadiazole core and TPE peripheries called TTPEBTTD (the structure is shown in Figure 1.9 b. This dye produces a red light with an emission peak of 650 nm. Also for this OLED, the emitter part is deposited via chemical vapor deposition. An example of single emitter AIE OLEDs produced with the bluish-green light-emitting material 1,3,6,8-tetrakis [4-(1,2,2-triphenylvinyl)phenyl]pyrene (TTPEPy) and the red light-emitting material 4-(4-(1,2,2-triphenylvinyl)phenyl)-7-(5-(4-(1,2,2-triphenylvinyl)phenyl)thiophen-2-yl)benzo[c][1,2,

5]thiadiazole (BTPETTD) are shown in Figure 1.9 c and d. When the two emitters are combined in the same device, one on top of each other or separated by NPB layer of 3 nm, a white OLED can be obtained [21] as shown in Figure 1.9 e. The AIE dye can be used also in the LED technology as down converting layer to obtain a white light. Yue et al. built an hybrid LED made by gallium nitride (GaN) covered with a down-converting layer of 4,7-Bis[4-(1,2,2- triphenylvinyl)phenyl]benzo-2,1,3-thiadiazole (BTPETD). GaN LED emits blue light (460 nm) that excites the downconverter layer with an emission around 550 nm. The out-coming radiation is the sum of the two emission spectra providing an overall white light [22].

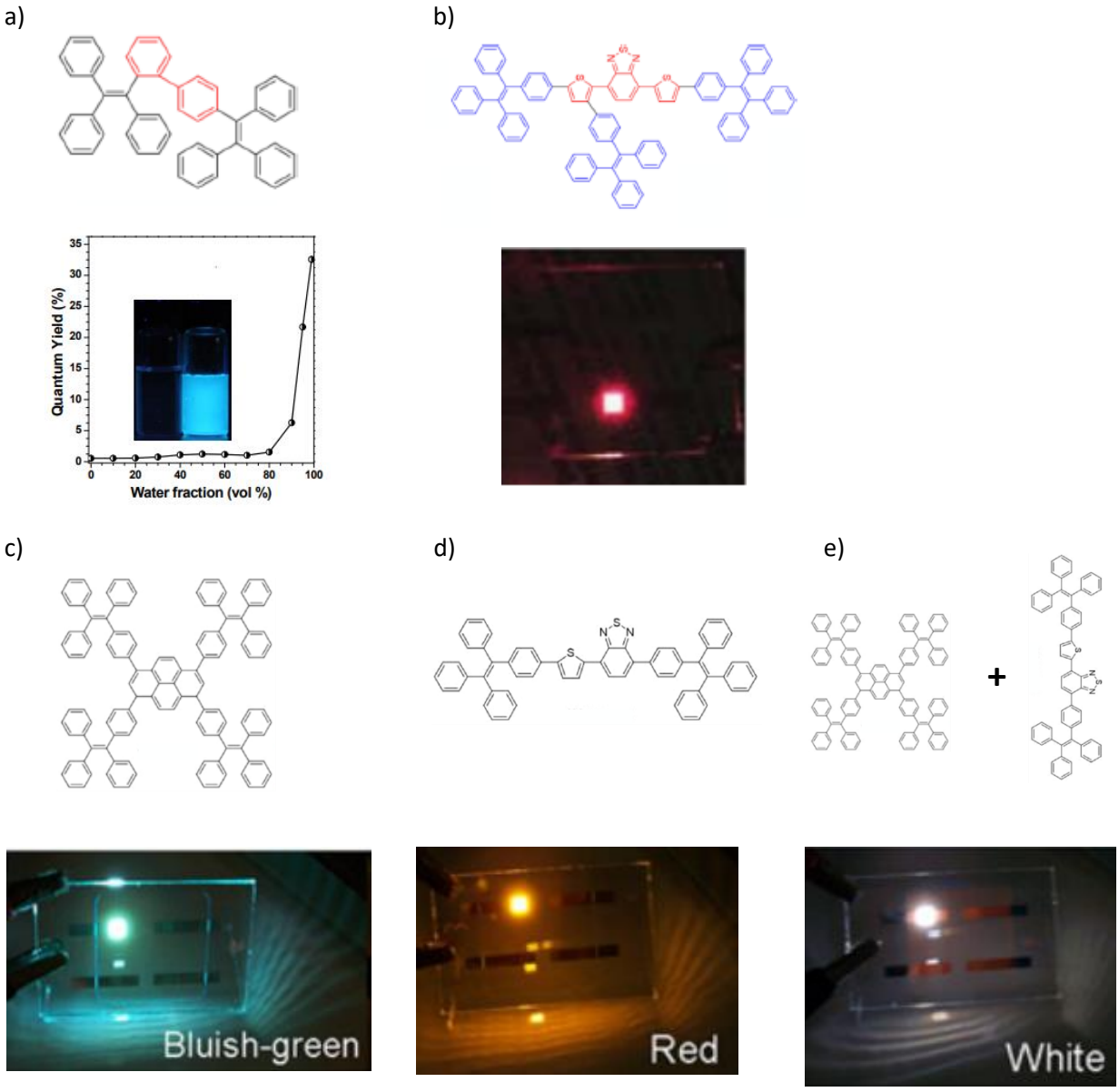

Figure 1.9: Examples of TPE-based chromophores used for OLED. Panel a) oTPE-pTPE molecule (λ_{max} = 454 nm) and values of fluorescence quantum yield depending on the water/THF ratio. In the inset, the dye solution mixtures inducing aggregation of the dye [20]. Panel b) TTPEBTTD molecule (λ_{max} = 650 nm) producing a red light OLED [23]. Panel c) TTPEPy (λ_{max} = 488 nm) gives a bluish-green OLED. Panel d) BTPETTD (λ_{max} = 592 nm) gives a orange-red OLED. Panel e) Combination of the AIE dye in c and d as emitter to originate a white OLED [21]. Pictures adapted with permissions.

1.3 Metal-organic frameworks (MOFs) for optical applications

MOFs, as a subset of porous coordination polymers (PCPs), are hybrid materials composed by metal ion center, also called secondary building unit (SBU), and organic linkers. These two components are bounded together to form a Werner complex (complex of organic molecule and metal ion) and generate an extended crystalline network. Both the SBU and the liker influence the structure of the resulting MOF but most important it is possible to predict the structure of the resulted MOF *a priori*, selecting the most suitable SBU and linker for the desired structure [24]. By changing the metal ion or the organic linker, it is possible to produce new structures with different properties, as shown in Figure 1.10 [25, 26].

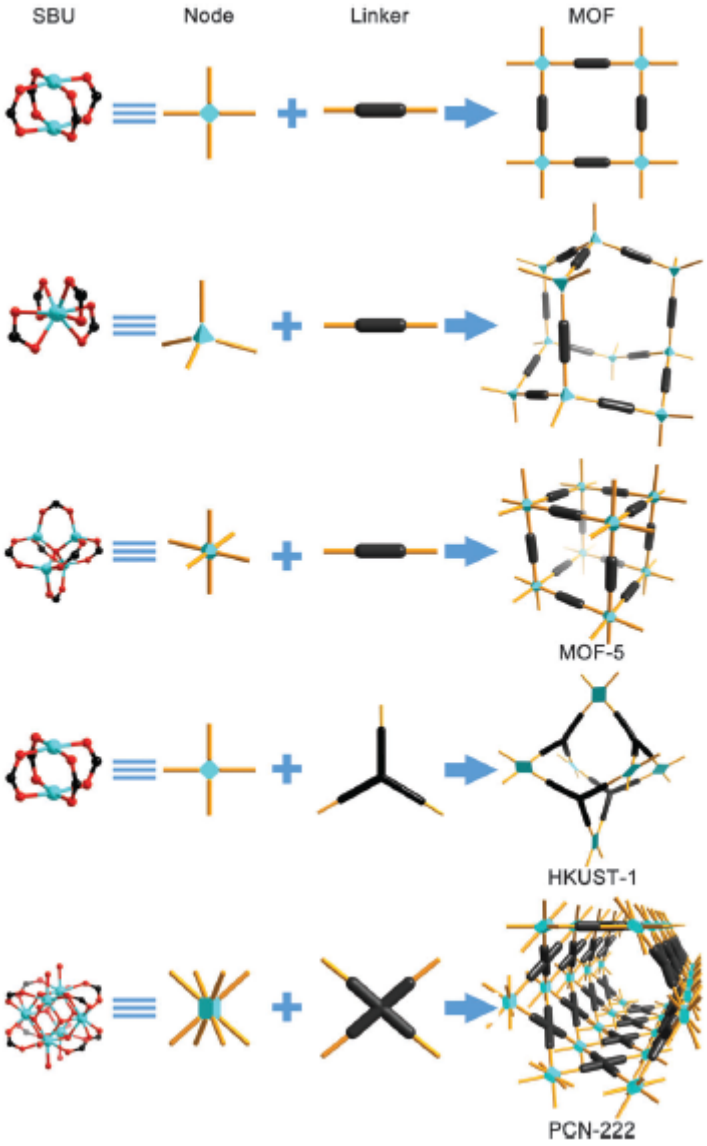

Figure 1.10: Examples of MOFs (on the right) composed by different SBUs (on the left) and different organic linkers (in the middle) [25] (reproduced with permission). The SBU unit, defined also as metal center, and the organic linker structure induces different geometry in the MOFs. The same linker with a different metal ion brings to a different MOF structure and *vice versa*.

The main characteristic of MOFs is the high porosity leading to a high specific surface area. This property brought a wide range of applications. The first application explored for MOFs is gas storage; MOFs have

been used to absorb hydrogen [27], methane [28] and carbon dioxide [29]. Yaghi *et al*. in 1995 [30] reported one of the first MOF (layered Co-BTC) showing a reversible molecule absorption. Catalysis is another application for MOFs, the catalytic properties in the MOF are provided by unsaturated metal sites and organic sites introduced during the MOF synthesis or in the MOF scaffold with post-synthetic modification (PSM) [31]. The porosity of MOF can also be used in gas separation; depending on the size of the pores, the MOF can be permeable to some molecule and impermeable to another one. An example is the membrane MOF, Cu-BDC lamella with nanometer thickness made by Rodenas *et al.* [32], which has shown the characteristic to separate CO_2 from a mixture of CH_4/ CO_2.

The MOF synthesis is influenced, not only by the starting materials but also by the production parameters as well. Several parameters influence the reaction products, including compositional parameters such as the molar ratio of starting materials, the pH of the starting solution and the solvent; and also process parameters such as reaction time, temperature and pressure. Stock and Biswas have distinguished the MOF synthesis methods into “conventional synthesis” and “alternative synthesis” [32]. Conventional synthesis can also be divided into solvothermal and non-solvothermal. The fundamental difference between these two syntheses is the reaction temperature. The solvothermal process required a specific temperature usually provided via a convection oven that is above the boiling point of the used solvent and is carried out in a closed vessel under autogenous pressure as defined by Rabenau [33]. Non-solvothermal processes required a lower temperature and, in some cases, the synthesis can work at room temperature. In room temperature processes, the vial is open, allowing the evaporation of the solvent, gradually increasing the concentration of the reactants and consequentially starting the nucleation of the MOF crystals.

The alternative synthesis routes use different energy sources, such as electric potential, electromagnetic radiation, mechanical waves (ultrasound), or mechanical forces. The source can influence reaction time, the pressure inside the vial, and the result of the reaction. In this work, Microwave-Assisted Synthesis (MAS) has been used as MOF synthesis. In MAS, there is direct contact of the micro-wave with the solution and the reactants which influences the nucleation rate and allows to produce a good quality MOF in a shorter time, compared to the solvothermal methods [34].

The tunability of MOF has also been used to produce MOFs with optical properties. The optical properties in MOFs can originates from the organic linkers, metal ion, or from a guest molecule loaded in the pores.

1.3.1 Ligand-based emission

The first requirement to have an emission directly from the organic linker is to have no interaction between the organic and inorganic components of the MOF. In particular, the metal ion should have core orbitals, as d^{10}, filled and consequentially the transition of d-d orbital or f-f orbitals forbidden such as in Cd^{II}, Zn^{II} and Ag^{I} ions. A second factor, which influences the ligand base emission, is the energy difference between HOMO and LUMO energy levels. If the energy gap between these two levels is small, then it is unlikely that the excitation is transferred via a charge transfer to the metal. For a high energy gap, the probability of having energy transfer from the organic linker to the metal ion is higher. This phenomenon is called ligand to metal charge transfer (LMCT) and brings a red shifting of the emission spectrum of the MOF.

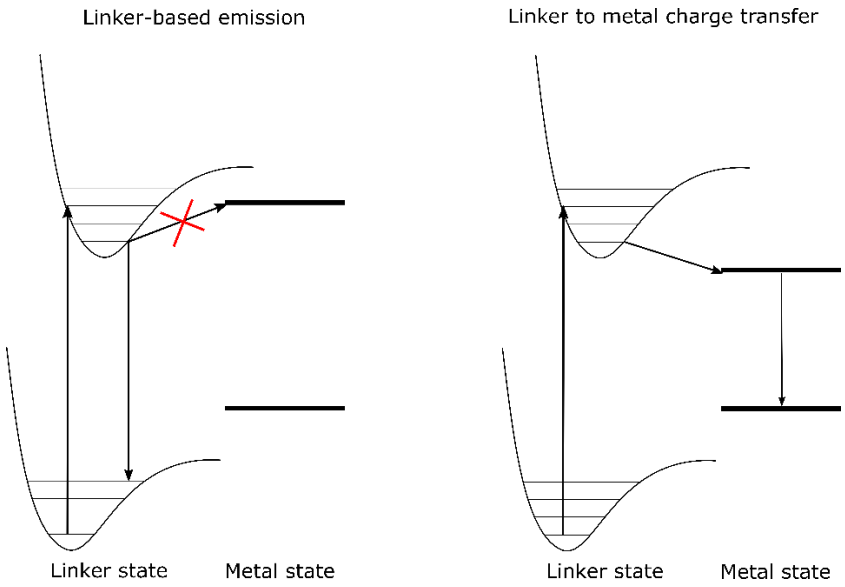

Figure 1.11: a) the emission mechanism from a MOF system where the bang gap of the organic linker is small and the excitation transfer to the metal state is unlikely. b) MOF where the energy gap of the organic linker is bigger and there is an excitation transfer to the metal center ligand to metal charge transfer (LMCT) [35].

An example of these two mechanisms can be found in the isoreticular MOF (IRMOF) family, which are with a cubic framework based on dicarboxylated linkers, where the degree of conjugation of the organic linker affects the energy gap and thus the emission mechanism [36]. IRMOF-1, MOF is constituted by a zinc acetate metal center and bicarboxylatebenzene (BDC), and has an emission peak of 525 nm. In the system, the organic linker acts as an antenna, which absorbs the light, and via LMCT the energy is transferred to the zinc metal [37]. On the other hand, the IRMOF-11 has the same structure of IRMOF-1 but with a different organic linker 4,5,9,10-Tetrahydropyrene 2,7-dicarboxylic acid. In IRMOF-11, the new linker has a higher degree of conjugation than the BDC, corresponding to a decrease in π-π^* energy gap making the energy transfer to the metal center less efficient with the consequent emission only from the linker [35].

Additional phenomenon that involves the transfer of charge between metal and linker is the metal to ligand charge transfer (MLCT), when a d-electron from the metal is transferred to a lower empty ligand state. MLCT is a characteristic phenomenon for MOF containing Cu^{1+} and Ag^{1+} metal centers. He *et al.* [38] described this behavior for seven different organic-inorganic compounds containing Cu^{I}. For $[Cu_2(CN)(5\text{-phtta})]_n$, in the emission spectrum, there are two peaks, and the one with longer wavelength (502 nm) can be attributed to the metal to ligand transition, while the second peak at 408 nm can be attributed to the ligand emission.

Other metal centers, such as Cu^{2+}, quench the emission from the organic linker due to its electronic structure. The quenching properties of the Cu^{2+} are related to the unfilled d orbitals of the Cu^{2+}which acts as a non-radiative channel for the excitation. Jayaramulu *et al.* [39] have shown how the incorporation of different amount of Cu^{2+} in a manganese-based MOF quenches the emission of the linker reducing the fluorescence quantum yield of the MOF and the lifetime of the emission.

The interpenetration of the MOF structure is another factor that influences the linker emission. The same linker in two different configurations could lead to different types of emissions as shown by Meek *et al.* IRMOF-15 (interpenetrated MOF) and IRMOF-16 (non-interpenetrated MOF) that are synthesized from Zinc nitratehexahydrate ($Zn(NO_3)\cdot 6H_2O$) and p-Terphenyl-4,4''-dicarboxylic acid (TPDC) as linker. To synthetize, the non-interpenetrated MOF a lower concentration of reactants in synthesis solution is needed. The interpenetrated MOF shows a red shifting in the emission, as shown in Figure 1.12, due to the

smaller linkers-linker and linker-metal center distances facilitate the energy transfer between these elements with respect to the non-interpenetrated structure [40] .

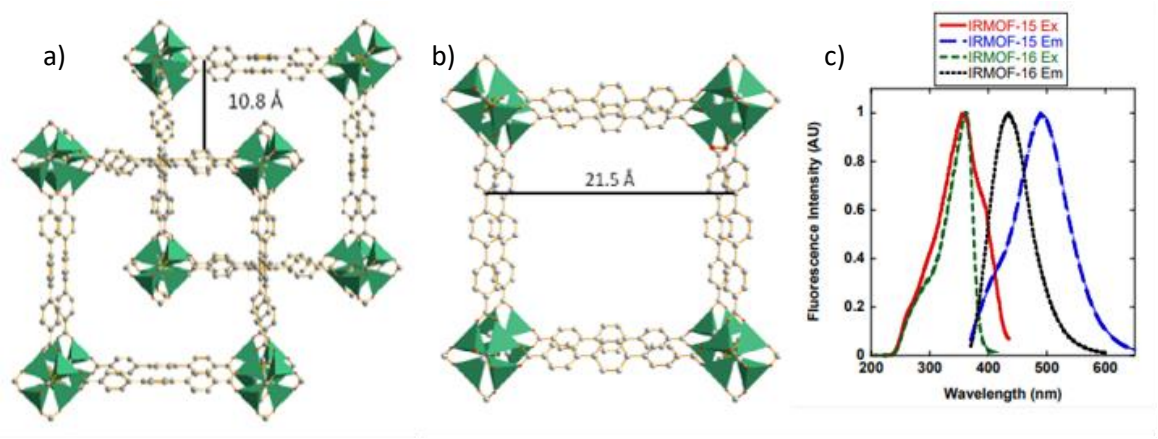

Figure 1.12: panel a) interpenetrated MOF, IRMOF-15. Panel b) non- interpenetrated MOF, IRMOF-16. Interpenetration changes the distances between linkers molecules and the distances between linker and metal center inducing a red-shifting in the emission spectrum panel c). picture reproduced with permission [40].

MOF scaffolds have also been used to enhance the emission properties of linker molecules. One example is the work of Wei *et al.* [41] where H_4ETTC, a TPE based molecule, is immobilized in a zirconium-based MOF that switches on the emission of the organic liker with an increasing of quantum yield from 30% to 99.5%. An additional example is a series of MOFs made by cadmium (Cd) and zinc (Zn) metal ion and terephthalic acid (TPA), isophtalic acid (IPA) and trimesic acid (TMA) as organic linker. The linkers in the MOF structure shown a long living phosphorescence at room temperature (RTP) with a maximum lifetimes of Zn-IPA MOF in air of 1321 ms [13].

1.3.2 Metal-based emission

MOFs with emission directly from the metal center usually contain SBUs made from rare earth elements or uranyl atoms. The rare earths are trivalent lanthanides (Ln^{3+}) which have a narrow emission and weak and narrow absorption. A solution for their weak absorption is to provide them with antenna molecules, with a broader absorption and transfer it to the lanthanides. The MOF scaffold provides an excellent system where the antenna molecule is the organic linker, and it is brought in the proximity of the lanthanides to increase the probability of energy transfer, as shown in Figure 1.13 a.

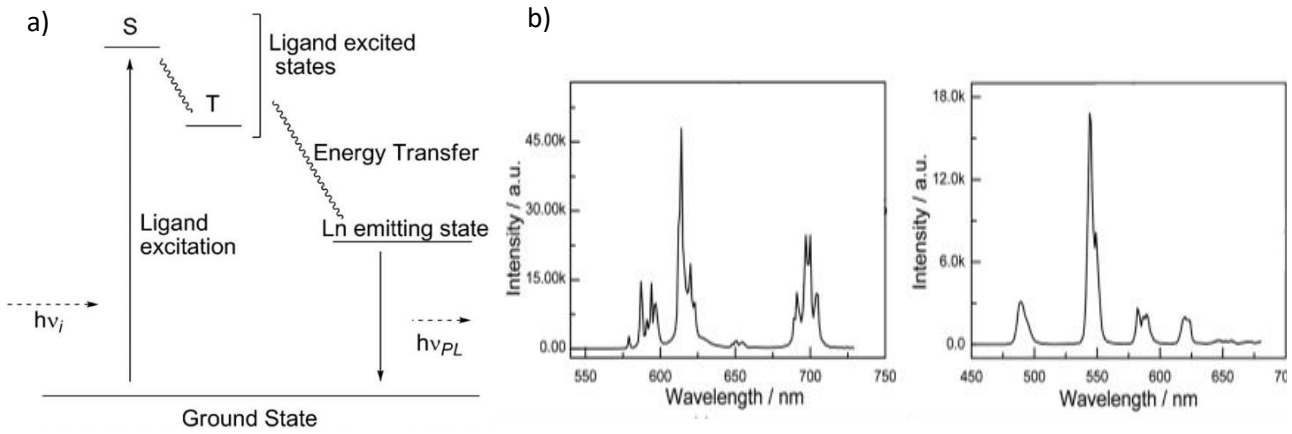

Figure 1.13: panel a) schematic representation of the processes involved in light absorption, energy transfer and light emission in a lanthanide based MOF equipped with organic linker antenna. The light ($h\nu_i$) is absorbed by the linker that get to an excited singlet state. Via intersystem crossing the excitation goes to a triplet state and then via energy transfer we have the excitation migration from linker molecule to the metal center, which finally emits light ($h\nu_{PL}$). adapted figure from [36]. Panel b) emission spectra of MOF made by europium and terbium as metal ion (left and right spectrum respectively) and 3-sulfobenzoateas organic linker [42]. Pictures reproduce with permission.

Li *et al.* [42] reported two examples of metal-based emission MOFs. The first one involves three different types of MOFs prepared via hydrothermal synthesis using europium, terbium and gadolinium as the metal center and 3-sulfobenzoate as the organic linker. All the MOFs show the typical narrow emission of the lanthanide shown in Figure 1.13 b. The second one, using the organic linker, 2-(pyridin-4-yl)-1H-imidazole-4,5-dicarboxylic acid, for MOFs with different metal centers, that vary from cadmium and zinc to europium, terbium and yttrium. The samples made with zinc and cadmium show emission from the linker, while those with lanthanide show only emission from the metal center, indicating that the excitation is transferred from the organic linker to the metal center [43].

1.3.3 Guest-induced emission

A third way to provide optical properties to the metal-organic framework is using their pores as sites for the loading of guest molecules. The guest molecules can provide their luminescence to the MOF; they can switch on the luminescence of the organic linker or the system guest molecule-MOF can express a new property.

Guest-induced emission in MOF can be found in the work of Muller *et al.*, where the N,N-bis(2,6-dimethylphenyl)-3,4:9,10-perylene tetracarboxylic diimide (DXP) molecule is loaded, via gas phase, into the MOF-5 structure. The gas phase loading consists in heating the dye molecule at 300°C into a chamber, with pressure of 10^{-3} mbar, containing the MOF. The loaded MOF changes its color and has new emission properties originating from the dye inclusion, as shown in Figure 1.14 [44]. An additional example, from the work of Wagner *et al.* [45], shows how, after the inclusion of the luminescent molecule, the emission changed due to the formation of an excimer inside the MOF structure, then the loaded MOF has new emission property but different from the loaded molecule in solution.

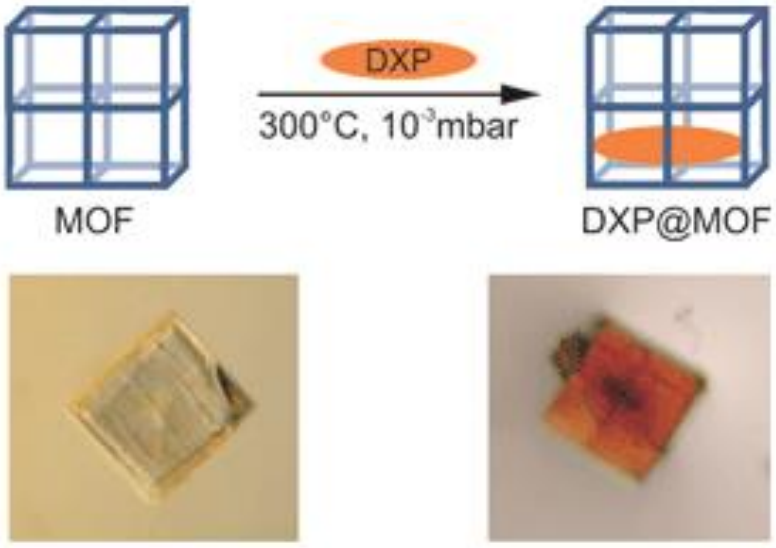

Figure 1.14: MOF-5 crystal before (right) and after (left) the inclusion via gas phase of N,N-bis(2,6-dimethylphenyl)-3,4:9,10-perylene tetracarboxylic diimide (DXP). After the guest molecule loading the MOF changed its color and shows new emission properties. Reproduced with permission [44].

Falcaro *et al.* made another significant example of dye inclusion in a highly orientated MOF film. The MOF is fabricated via heteroepitaxial growth starting from a copper hydroxide substrate. The molecules are incorporated via immersion of the MOF sample in an ethanolic solution containing the dye and the emission of the dye is recorded via fluorescence spectroscopy. In Falcaro's work, the MOF structure even induced a certain orientation in emission of the dye giving different fluorescence response depending on the orientation of the excitation light [46].

1.4 Surface anchored metal-organic frameworks (SURMOFs)

For a device-driven approach, MOF powder provides a limited fields of application. Thin-film configuration is a more versatile and the ideal system to be deposited on a solid substrate.

Fisher *et al.* [47] have defined two categories of MOF thin film: polycrystalline MOF film and surface anchored metal-organic frameworks (SURMOFs). The polycrystalline MOFs are films of randomly orientated MOF crystals that can grow as island in a non-continuous layer, as shown in Figure 1.15 a. On the other hand, SURMOF grows uniformly orientated with their (001)-axis aligned with the surface normal and their thickness is strictly related to the organic linker used and to the number of deposition cycles, as shown in Figure 1.15 b.

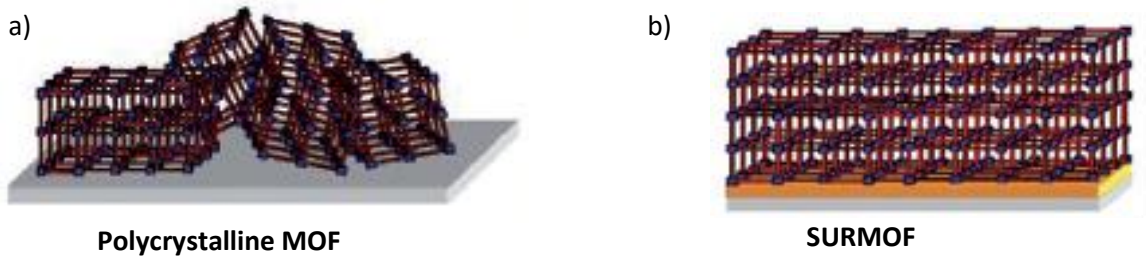

Figure 1.15: panel a) graphical representation of a polycrystalline MOF film. Polycrystalline MOF grows as islands with different crystalline orientation. Panel b) graphical representation of a SURMOF grown on gold substrate. SURMOF shows an higher degree of crystallinity and covers in an homogenous fashion all substrate. Picture adapted and reproduced with permission [48].

In this work, only SURMOF are investigated due to their higher degree of crystallinity, which guarantees well-defined oriented pores where guest molecules can be intercalated to give SURMOF new properties. In order to grow SURMOFs it is necessary to functionalize the substrate surface. For this purpose, two approaches are possible, i) using self-assembly molecules called self-assembled monolayer (SAM) or ii) using oxygen plasma treatment. The surface functionalization is important not only to give anchoring points to the SURMOF but in some cases, to induce a specific type of crystallinity in the SURMOF. As shown by Liu *et al.* [49], SAM as 16-mercaptohexadecanoic acid (MHDA) that gives COOH groups as anchoring point, and 11-mercapto-1-undecanol (MUD), which gives OH group, induced two film orientations in the HKUST-1 SURMOF. SAMs are used for functionalizing metal substrates, such as gold, whereas oxygen plasma is used for functionalizing substrates such as quartz and silicon. In this work, only the oxygen plasma treatment is used because the samples are only prepared on glass or silicon substrate. Therefore, the functionalization with oxygen plasma treatment is described in detail in the method chapter. SURMOFs are deposited via layer-by-layer deposition, where the substrate surface is exposed to an ethanol solution containing the metal ion and then to a solution with the organic linker. After every exposure, the sample is washed with ethanol to remove the unreacted species. Thicker SURMOF can be obtained, increasing the number of cycles, as shown in Figure 1.16.

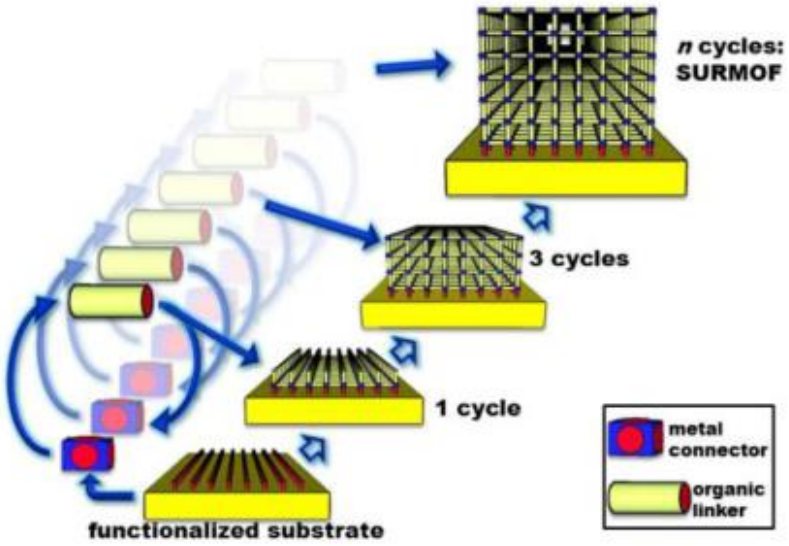

Figure 1.16: schematic representation of the SURMOF formation with reaction of metal ion and organic linker. The increasing number of cycles increases the SURMOF thicknesses. Picture reproduced with permission [50].

There are four methods of SURMOF thin-film deposition. The first one, developed by Wöll and co-workers in 2007 [51], is called the dip method. In the dip method, the substrate is dipped into the metal and linker solution, and the reaction of the components of the MOF develops during the time that the substrate spends inside the solutions, as shown in Figure 1.17 a. A second method for SURMOF deposition is spray coating, where the reactant solutions are sprayed towards the substrate via spray nozzles, as shown in Figure 1.17 b [52]. The spraying method, with respect to the dip one, is faster and can produce thicker SURMOF. The third method is the pump method, where the substrate is kept in a closed vial at the desired temperature and the reactant flow in the vial via a pump following the standard steps, as shown in Figure 1.17 c [53]. Pump method is used for SURMOF, which required a specific temperature and a close environment. The last method developed in 2016 by Chernikova and co-workers [54] is the spin coating method, where the solutions are spread via syringes overall substrate using a spin coater, as shown in Figure 1.17 d. This method is characterized by a low growth rate, high precision of control of the SURMOF thickness and uniformity in the deposition.

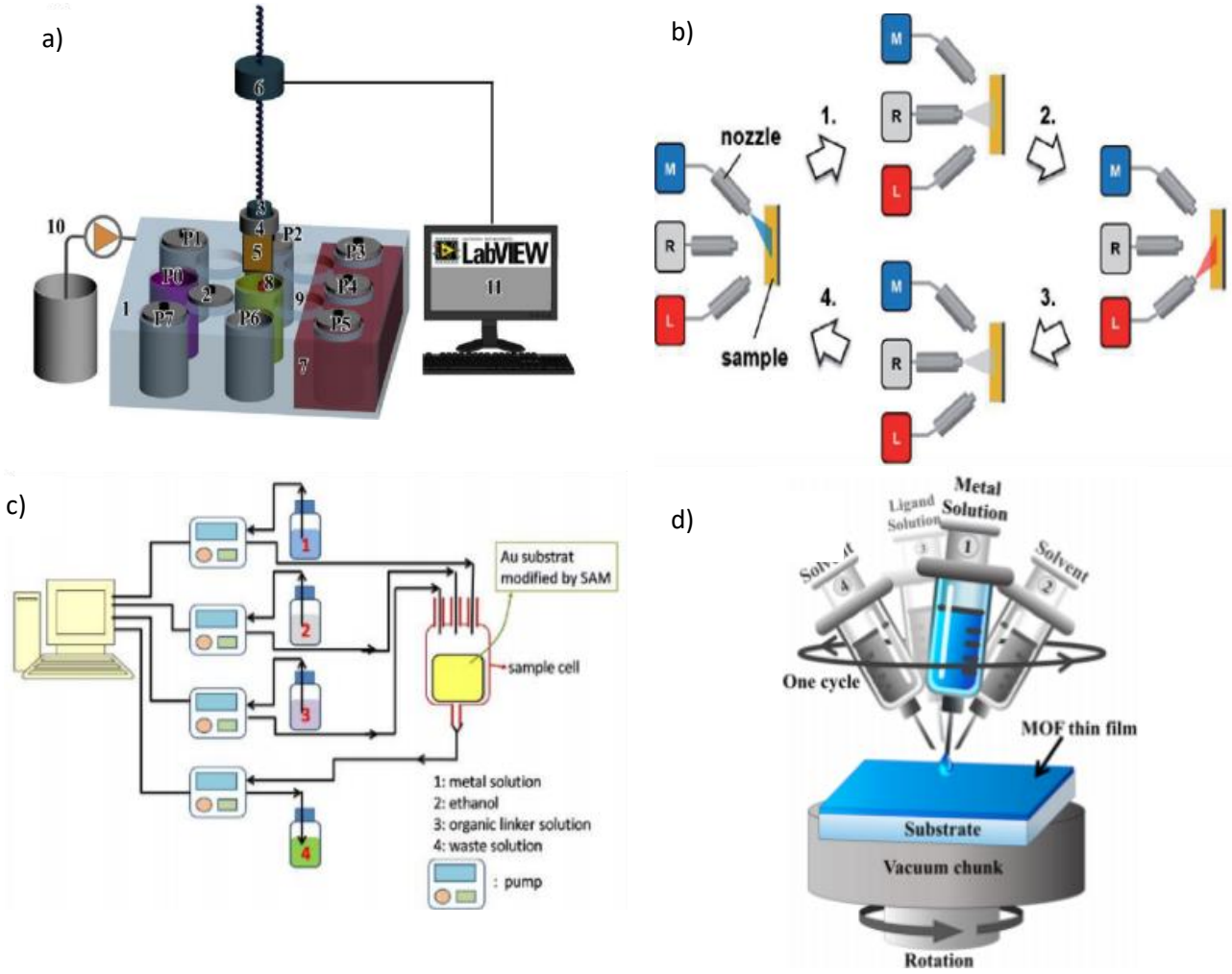

Figure 1.17: panel a) Dip method performed by a robot arm, controlled by a PC, which dips the substrate in the different backers containing the different reactants and rinsing solutions. Panel b) Spray method and its steps where “M” stands for metal solution, “L” linker solution and “R” rinsing solution. Panel c) Pump method, the substrate is placed in a sample cell, where three pumps controlled by a PC, the sample cell is flushed with the different reactants solutions. The unreacted solution, after each step, is flushed out via a fourth pump. Panel d) Spin coating method, the substrate is placed on a fixed vacuum plate during the rotations. The syringes put a chosen amount of solution onto the substrate, and the rotation spreads the solution all over the substrate. Pictures reproduced with permission [48, 53-55].

In this work, only the spray method is used as a deposition route for its versatility to coat a big area and obtain a thick SURMOF in a short amount of time, which are essential characteristics for a device-driven approach. Therefore, it is described in detail in the second chapter. In the SURMOFs synthesis, in contrast to the MOFs, the metal centers are limited to the ones with a paddle wheel structure, such as zinc acetate and copper acetate. On the other hand, the range of linkers is larger, organic linkers with dicarboxylic groups at meta (i.e. the positions of substituents in the aromatic compound are 1,3 positions) and para (i.e. the positions of substituents in the aromatic compound are 1,4 positions)positions, used for building 2-D SURMOF called SURMOF 2. SURMOF 2 has a sheets-like structure where the lattice parameter in two directions is given by the organic linker, and the third one is smaller and usually around 0.6 nm, as shown in Figure 1.18 a. Other organic linkers with nitrogen group at para positions are used to form 3-D SURMOF called pillar SURMOF [4]. The pillar SURMOFs are composed of both types of linkers. The carboxylic acid linker coordinates two directions, while the nitrogen linker coordinates the third one, as shown in Figure 1.18 b. An exception is the SURMOF called HKUST-1 that has a 3-D structure using a trimesic acid with three anchoring points as the organic linker and copper acetate as the metal center.

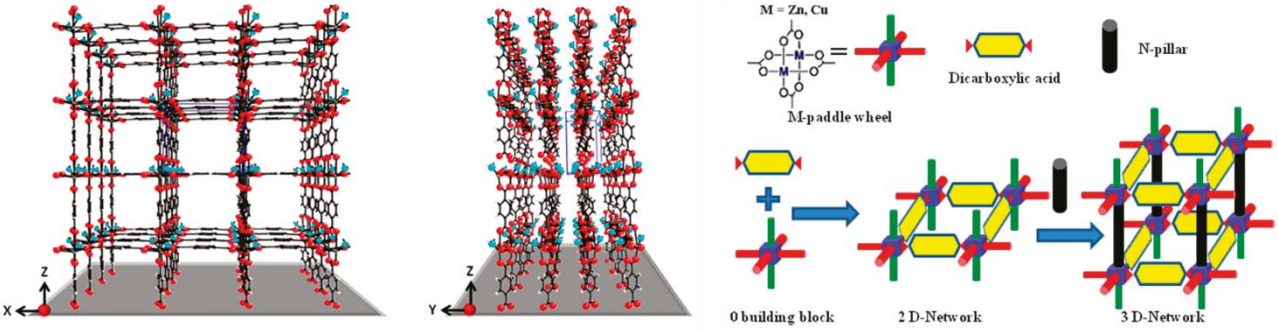

Figure 1.18: Panel a) SURMOF2 structure in the three direction. Panel b) components and structure of the pillar SURMOF. Pictures adapted with permission [53].

In this work, only SURMOF 2 structure is explored due to the optimal spacing between its sheets, which allows incorporation of big flat guest molecules. Furthermore, the SURMOF 2 structure is also suitable for the spray method. [42]

1.5 Outline

The experimental methods used for production and characterization of the main materials are presented in the **2nd chapter**.

The results of the metallated porphyrin molecule loading in the SURMOF 2 structure with material and optical characterization is described in the **3rd chapter**.

The characterization of H_4ETTC aggregation-induced emission dye loaded in the SURMOF 2 structure, the determination of dye density and how the structure enhances dye emission are presented in the **4th chapter**.

Two optical applications for SURMOF 2 loaded with H_4ETTC, dye printing and SURMOF based luminescent solar concentrator are shown in the **5th chapter**.

The synthesis and the characterization of two MOFs with room temperature phosphorescence, Zn-IPA and Zn-DTA and the loading attempts with iridium complex are presented in the **6th chapter.**

The conclusions of the work and the outlooks for the research are presented in the **7th chapter**.

Chapter 2: Materials and Methods

2.1 SURMOF synthesis

For the SURMOF synthesis, the spray coating has been chosen as deposition method, over the other three (dip method, pump method and spin coating method), for two reasons: the growth rate and the flexibility of the process. In the first, the aerosol formation during the spraying decreases the reaction time of reactive species of the SURMOF due to the high reaction surface. The second allows the SURMOF deposition on surfaces with different sizes, which is an essential feature for a scale-up and a device-driven process [52].

2.1.1 Substrate activation

Before the deposition process, the substrate has been functionalized to give anchoring sites where the metal ions can attach and start the nucleation of the SURMOF. The activation includes a first step of cleaning process to remove the contaminants from the top surface of the substrate, through the immersion in an ultrasonic acetone bath for ten minutes. Then the substrate is treated with oxygen plasma (4-TEC plasma etcher), which finishes the process of cleaning and provides the hydroxylic groups (OH^-) over-all substrate surface.

2.1.2 SURMOF deposition

The SURMOF deposition set-up is composed of three spraying nozzles connected to metal ion solution, organic linker solution and rinsing solution, respectively, as shown in Figure 2.1. The spraying nozzles are pressurized and connected to nitrogen gas with a pressure of around 2 bar.

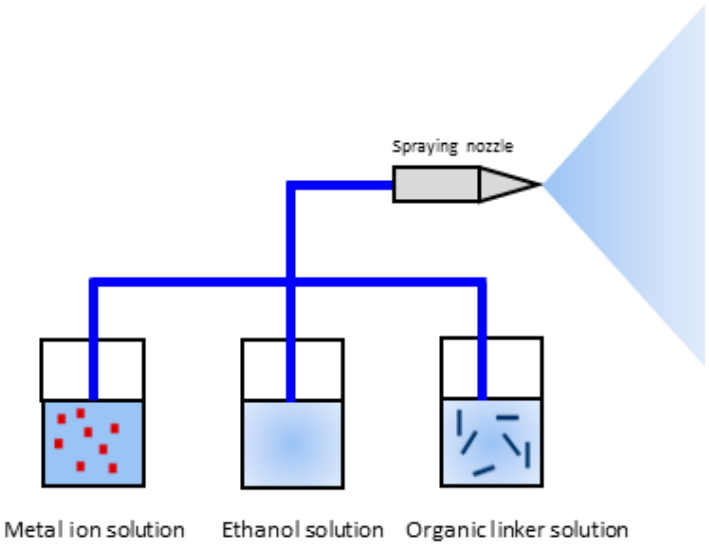

Figure 2.1: spraying set-up composed of three vials with metal ion solution (red squares), rinsing solution, and linker solution (blue bars).

After the activation, the substrate is sprayed for 15 seconds with 1 mM ultra-pure ethanol solution of the chosen metal ion, followed by a waiting step for 35 seconds. The sample is then rinsed for 5 seconds with ultra-pure ethanol and sprayed for 25 seconds with 0.2 mM ultra-pure ethanol solution of terephthalic acid (H_2BDC). Afterward, the process is concluded with an additional waiting step of 35 seconds and ethanol rinsing for 5 seconds. During the waiting time, the sample is tilted in a horizontal position in order to preserve the sample humid. This procedure has not been described before in the literature, but it has been developed within this thesis during the optimization of spray coating, as it provides samples with better crystallinity and increasing optical quality, as shown in Figure 2.2. The result is consistent with the other methods, such as the dipping method and the pump method, where direct contact with reactant solutions has been shown to enhance the nucleation. The process described above is defined as a cycle, with a total time of two minutes and the thickness of the SURMOF increases with the number of cycles. The samples presented in this work are the result of 30 cycles spraying to achieve the thicknesses of 150 nm (measured via Dektak), since one cycle of spraying corresponds to 5 nm SURMOF on average.

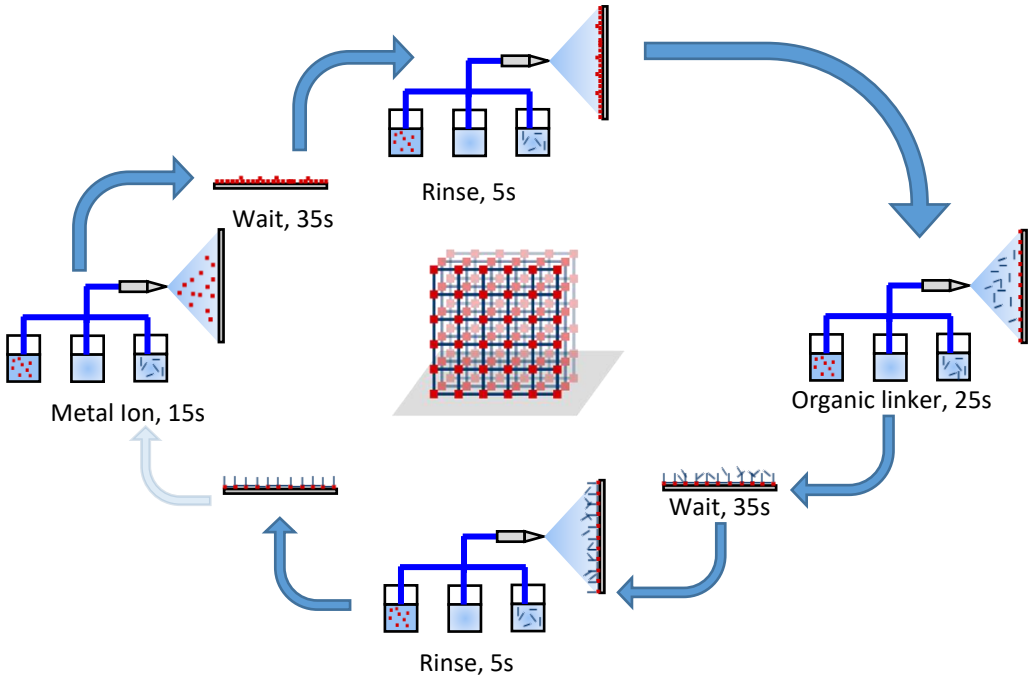

Figure 2.2: schematic representation of one cycle of SURMOF spray coating. The cycle is composed of the spraying of metal ion solution for 15 seconds, waiting step for 35 sec, rinsing with ethanol step for 5 sec, spraying organic linker solution for 25 sec and again waiting step for other 35 sec.

2.2 Post-synthetic loading of SURMOF films: Drop-Casting

Nicolò Baroni, Michael Oldenburg and Ian A. Howard developed this technique as route for dye loading in SURMOF [56].

In this section, the technique for dye loading in SURMOF is described. The technique is used in the third and fourth chapter to achieve a high density loading of metallated porphyrin and aggregation induced emission dyes inside SURMOF.

Ultra-pure ethanol solution with a dye concentration of 0.1 mM is spread over the SURMOF surface of the (Figure 2.3 b) and allowed to let dry completely. During the drying process, the dye molecule passes, via diffusion, from the solution to the sample (Figure 2.3 c). Depending on the amount of solution drop-casted on the samples, a different dye concentration inside the SURMOF is reached. After the solution is

completely dried, the sample is rinsed with 20 ml flux of ethanol for 30 seconds, which allows to remove the unreacted dye present on the surface and not loaded in the SURMOF scaffold, as reported in Figure 2.3 d.

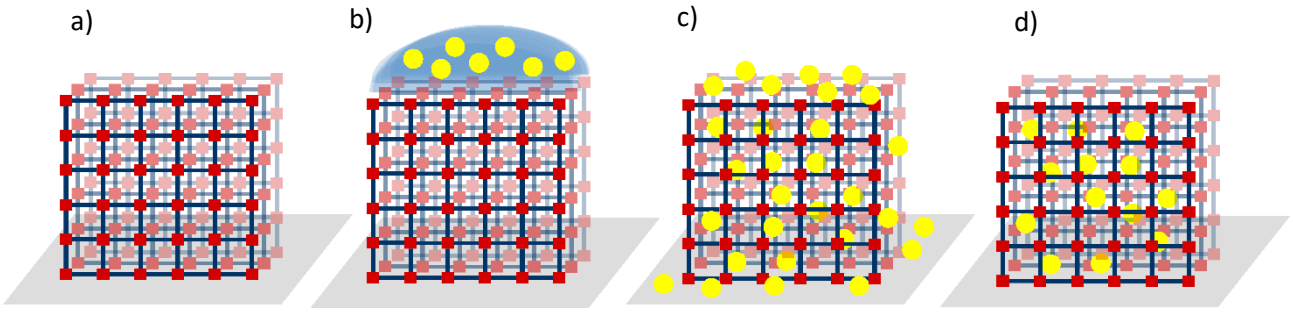

Figure 2.3: panel a) empty SURMOF. Panel b) solution drop-casts on SURMOF. Panel c) SURMOF after dye diffusion. Panel d) Rinsed SURMOF.

2.3 Material and Structural characterization

2.3.1 X-ray diffractometry (XRD)

The most important characteristic of a SURMOF, which can also be used as a figure of merit of its quality, is crystallinity. In this work, crystallinity has been studied via X-ray diffractometry (XRD). The principle behind XRD is the Bragg diffraction, which describes the behavior of X-rays interacting with two parallel crystalline planes. For constructive interference, the Bragg's law is:

$$n\lambda = 2d\sin(\theta), \tag{2.1}$$

Where n is the order of constructive interference, λ the wavelength associated with the x-ray source, d is the spacing between the planes and ϑ is the angle of incidence of the x-ray. With Bragg's law, it is also possible to understand the SURMOF structure, calculating the distances of the crystalline planes in the three directions from the diffraction angle, as shown in Figure 2.4. XRD out-of-plane and in-plane are performed to resolve all the three lattice parameters of the SURMOF. From out-of-plane XRD, the distance between planes parallel to the substrate are obtained (Figure 2.5), while XRD in-plane provides information about the lattice parameters in the other two directions.

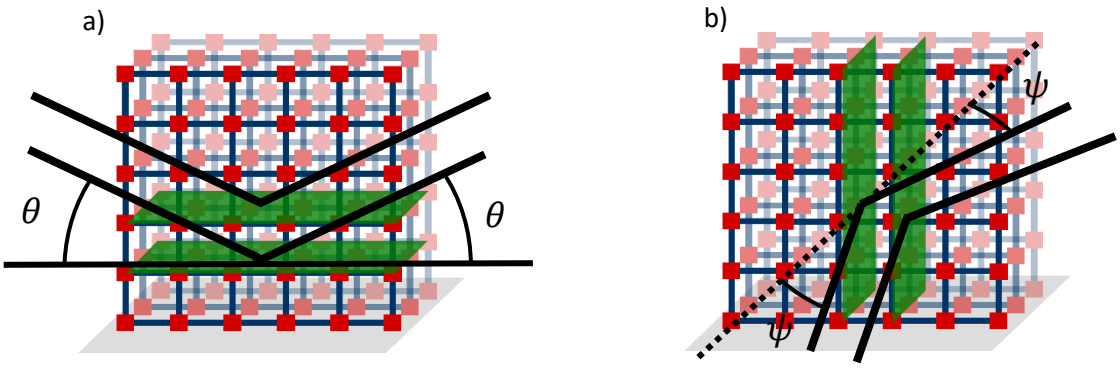

Figure 2.4: Panel a) XRD out-of-plane configuration, which measurement can detect the distance between crystalline planes parallel to the sample surface. Panel b) XRD in plane configuration, which gives information about the crystalline planes perpendicular to the sample surface.

For x-ray diffraction measurements, the instrument XRD D8 advanced from Bruker has been used, equipped with an x-ray source of Cu-anode with a Cu $K_\alpha 1,2$ radiation (λ = 0.15419 nm).

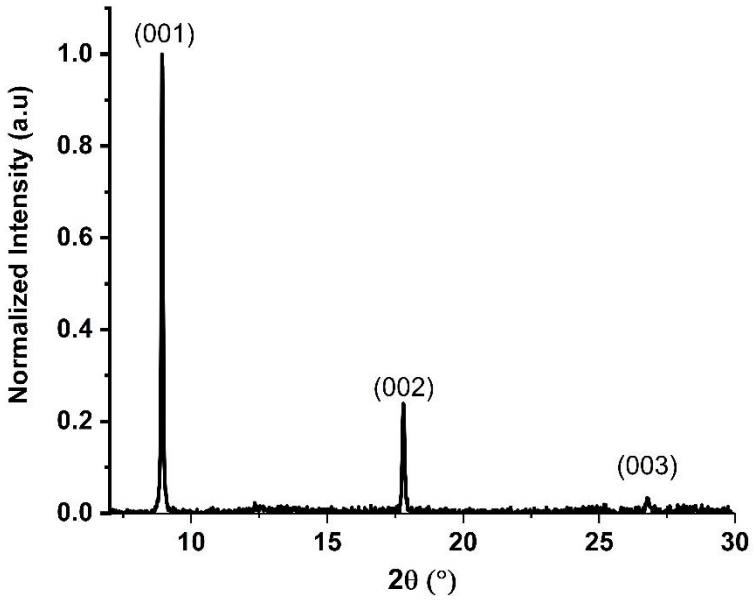

Figure 2.5: XRD out-of-plane of ZnBDC SURMOF with the first three diffraction peaks. Considering the angle related to the first order of diffraction, the distance between planes parallel to the sample surface can be calculated applying Bragg's law.

2.3.2 Proton nuclear magnetic resonance (HNMR)

HNMR is performed during the synthesis of the organic ligand H_4ETTC to determine the chemical purity of the reaction products. HNMR is based on the principle that the hydrogen nucleus in an external magnetic field shows splitting in the energy level due to the hyperfine structure. When the nucleus is excited by radio frequency, it absorbs and then remits this radiation. The splitting in energy is influenced by the electron cloud of the surrounding atoms, which shields the magnetic field. HNMR detects H atoms in the analyzed

molecule. In particular, with HNMR it is possible to differentiate H atoms with a different environment (neighbor atoms), thus the peaks in the HNMR spectrum are related to a hydrogen atom with a specific environment. In order to perform HNMR, the samples need to be dissolved into a deuterated solvent where the hydrogen atoms are replaced with deuterium atoms. Deuterium is not HNMR active, and the solvent is not interfering with the measurement. The HNMR spectrum provides four kind of information that can be related to the analyzed compound. i) The number of peaks in the HNMR spectrum provides the number of H-atoms with a different environment, where H-atom with the same environment provides the same signal and they are called chemical equivalent. ii) The chemical shift is related to the frequency of the re-emitted radiation weighted over to the frequency of the radiation sent by the HNMR instrument. Chemical shift is reported as the x-axis in the HNMR spectrum, and it is measured in parts per million (ppm). iii) Area of the peaks, which is related to the number of H-atom that contributes to the peak. iv) Peaks splitting, the H-atom signal is influenced by the neighbor H-atoms via spin-spin coupling that splits the single peaks into a doublet, triplet, quadruplet, and quintuplet. HNMR of tetraphenylethene is reported in Figure 2.6, showing the chemical shift (in ppm) on x-axis and the relative intensity on y-axis.

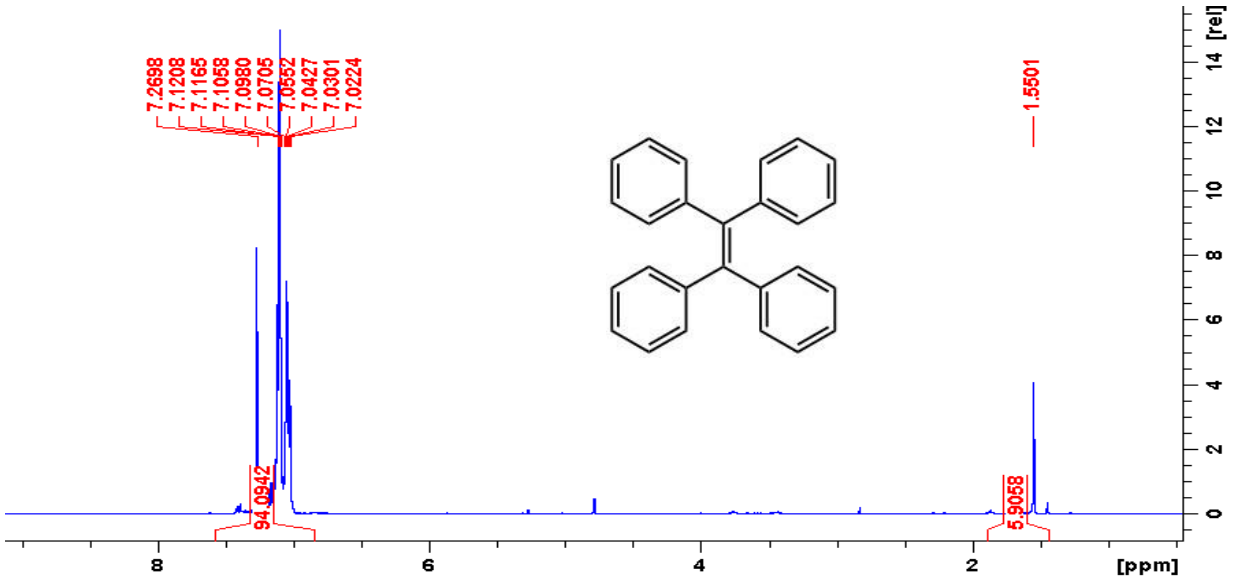

Figure 2.6: example HNMR spectrum of tetraphenylethene in deuterated chloroform ($CDCl_3$). The peaks related to the compound are at higher ppm (between 6 and 8 ppm), while peaks at lower ppm are the result of traces of residual elements from the synthesis.

The instrument used for HNMR analysis is a Bruker Avance III-HD 300 MHZ provided by the Institute of chemistry and biochemistry of the University of South Carolina, U.S.A.

2.3.3 Time of flight secondary ion mass spectroscopy (ToF-SIMS)

In the third chapter of this work, in order to study the loading of metallated porphyrins inside the SURMOF 2 structure, ToF-SIMS has been performed.

ToF-SIMS is a technique, which provides information on the surface composition. It consists of a high-energy ion bombardment, which leads to the removal of ions that could be neutral, positively, or negatively charged. These ions are collected to a mass analyzer, which can discriminate the ions depending on their time of flight. In this work, ToF-SIMS has been used for proving, via a depth profile, that palladium

porphyrin and platinum porphyrin dye have been successfully loaded inside SURMOF scaffold. In order to have a depth profile of the sample, ToF-SIMS has been performed in dynamic mode, which differs from the static ToF-SIMS for the presence of a second ion gun, which has the purpose of eroding the sample while the other ion gun analyzes the bottom of the crate.

The SURMOF samples for ToF-SIMS analysis are prepared on silicon, instead of glass, to avoid the charging of the substrate during the process. In this thesis, the instrument used to perform the experiments is a ToF-SIMS-100, ION-TOF, equipped with two ion beams: a 20 KeV C_{60} for eroding the sample fully interlaced with a 25 keV Bi^{3+} beam of 1.2 ns pulse width for mass spectrometry. The former beam is scanned over 500×500 μm^2 (0.6 nA pulsed beam current), while the latter scanned at a concentric field of view of 200×200 μm^2, 64×64 pixel, 0.5 pA). The obtained data are displayed with the sputtering time (s) on the x-axis, which can be converted into a sputtering depth (nm) knowing the sputtering velocity and assuming that the sputtering process in the SURMOF is constant. The intensity of the selected species is reported on the y-axis. Two examples of ToF-SIMS spectra are presented in the results, in chapter 3.

2.3.4 Film thickness determination

The sample thickness is measured using a profilometer Dektak 220-Si from Veeco. The samples are screeched and the depth of the film by scanning with the Dektak tip over the scratch and analyzed by the instrument. The average thickness for 30 cycles (corresponding to one hour of spraying) is 150 nm.

2.4 Optical characterization

2.4.1 Absorbance, transmission and reflection measurements

Absorbance, transmission, and reflection spectra of the samples are recorded with a UV-Vis spectrophotometer, Perkin Elmer lambda 950. A schematic representation of the light path inside the spectrometer is shown in Figure 2.5.

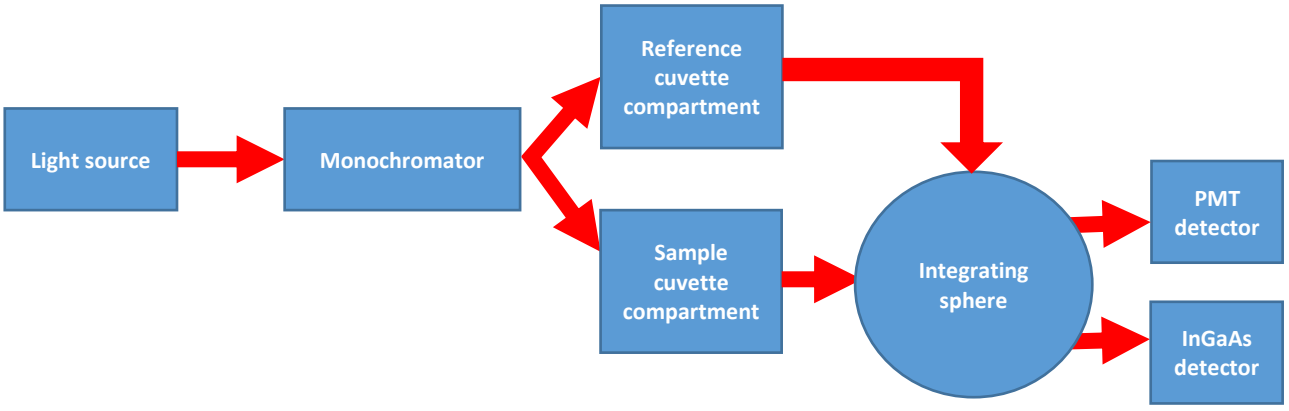

Figure 2.5: schematic representation of the UV-Vis spectrometer. The light emitted by the source is selected by the monochromator, and then split into a reference beam and a sample beam. Both beams reach the integrating sphere where the light is detected by PMT and InGaAs, for UV-Vis and NIR radiation respectively.

The instrument is characterized by two light sources, a deuterium lamp that provides the light for the UV region (175 to 320 nm) and acts as a calibration source for the detectors and a tungsten halogen lamp, which provides the light for the remaining part of UV, visible and near-infrared region (320 to 3300 nm). After the light sources, a beam of a single wavelength is produced by a double holographic grating monochromator. Then the light leaving the monochromator is split into two beams, a reference beam and a sample beam. The reference beam acts as a feedback signal, which prevents the measurement from being influenced by the fluctuation in energy of the second beam hitting the sample. Once light reaches the sample compartment, it is divided into two sections: the first one made by two cuvette compartments for measuring the absorbance of a liquid sample and the second one equipped with an integrating sphere of 150 mm coated with diffusive material (pressed PTFE) to measure transmission, reflection, and absorbance of the thin film sample. The integrating sphere is equipped with a photomultiplier detector for UV and visible light (175 to 860 nm) and InGaAs detector for near-infrared radiation (860 to 3300 nm). Reference beam and sample beam are chopped with different frequencies and therefore both are detected with the same detector. Before each sample measurement, an analytical blank (i.e. with no sample) is performed as a reference measurement. For transmission measurement, the sample is placed in front of the integrating sphere, which collects all the light transmitted by the sample, as shown in Figure 2.6 a. For reflection measurement, the sample is placed on the back entrance of the integrating sphere in order to collect only the reflected light from the sample, as shown in Figure 2.6 b. For absorbance measurement, the sample is placed inside the integrating sphere, which collects the light reflected and transmitted, as shown in Figure 2.6 b.

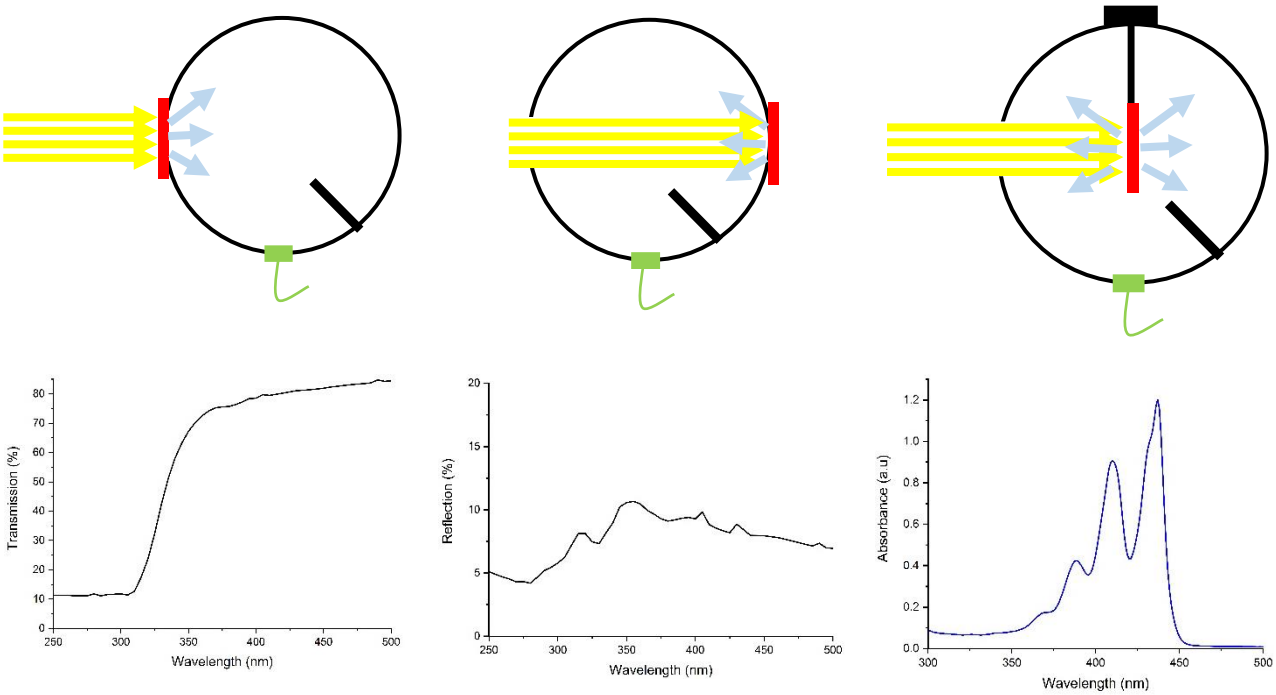

Figure 2.6: panel a) configuration for transmission measurement, the sample is placed in front of the sphere and only the light transmitted is collected. Panel b) configuration for reflection measurment, the sample is placed on the back of the sphere and only the reflected light is collected and measured. Panel c) configuation for absorbance measurment, the sample is placed inside the integrating sphere and the both transmitted and reflected light is collected. Below each specific configuration, an example of the resulting spectra is shown,ZnBDC transmission, reflection and absorbance of PMMA perylene film respectively.

The absorbance spectrum can be used to determine the concentration of a fluorophore solution. Beer-Lambert law relates the absorbance (A) or optical density, which is the attenuation of light intensity passing through a medium, with the concentration of dye (c) in this medium in molarity, the path length (l) in cm and the probability that a photon with a certain energy is absorbed by the material, named extinction coefficient. Defining I_0 as the intensity of the light that hits the sample and I the emerging light intensity from the sample, the infinitesimal decreasing of light intensity is:

$$-\frac{dI}{I} = \alpha c\, dx, \tag{2.2}$$

With α as the proportionality constant. Integrating between *x = 0* and *x = l* with α and c not depending on x, the equation becomes:

$$\log\left(\frac{I_0}{I}\right) = \alpha c l, \tag{2.3}$$

With $\varepsilon = \frac{\alpha}{2.303}$ as the molar extinction coefficient ($M^{-1}cm^{-1}$),which is constant for each dye.

$$\log\left(\frac{I_0}{I}\right) = \varepsilon c l, \tag{2.4}$$

With the transmission *T*:

$$T = \frac{I}{I_0}, \tag{2.5}$$

Re-defining *A*:

$$A = -\log(T) = \varepsilon c l. \tag{2.6}$$

The Beer-Lambert law is used to determine the dye concentration in a solution starting from *A* and *ε*. *ε* can be obtained using a calibration curve, where the solution concentration is correlated with the absorbance peak. The calibration curve displays a linear correlation that ideally passes through the origin, as shown in Figure 2.7. The slope of the curve is the extinction coefficient.

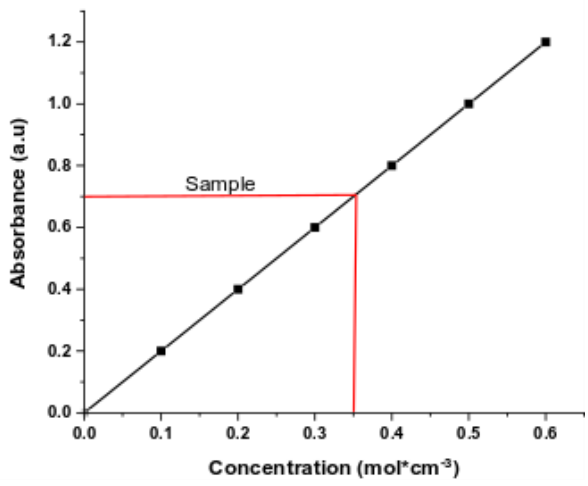

Figure 2.7: calibration curve (in black) to determine the solution concentration of a sample from the absorbance at a certain wavelength. The points reported are the result of the absorbance measurements of samples at a known concentration.

2.4.2 Emission measurements

Emission measurements are performed with a Varian Cary Eclipse fluorescence spectrophotometer. The excitation source of the spectrophotometer is a xenon lamp, and it is equipped with a photomultiplier detector with sensitivity from 250 to 900 nm.

2.4.3 Photoluminescence quantum yield measurements

Photoluminescence quantum yield (PLQY) can have two definitions. The internal PLQY (i-PLQY) defined as the ratio between the number photons emitted and the number of photons absorbed and the external PLQY (e-PLQY) defined as the ratio between the number of photons emitted and the number of the incident photons. The i-PLQY is calculated following the route described by De Mello *et al.* [57].

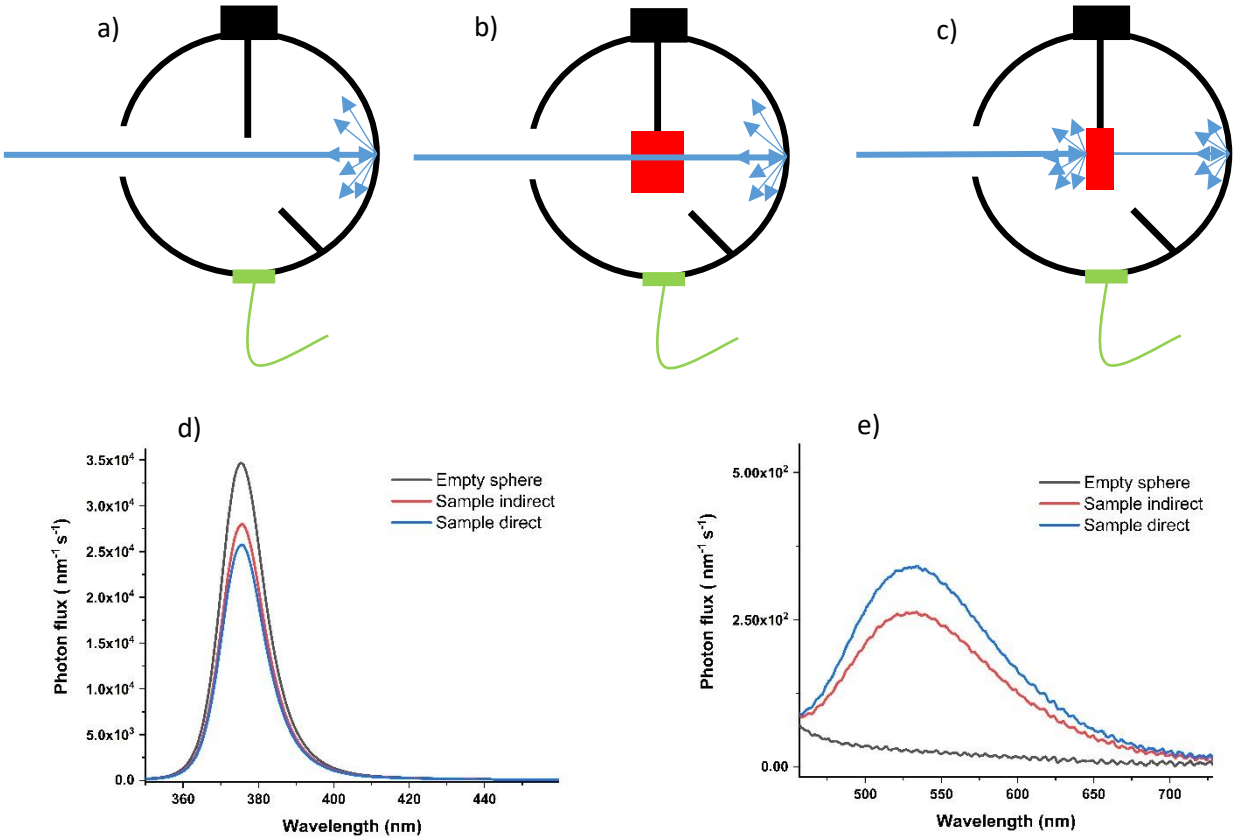

Figure 2.8: panels a), b) and c) integrating sphere with the sample holder and the buffer (avoid direct light from the laser to the detection port) in black, the detector port that brings the signal, via optical fiber, to the detector in green and the sample in red. Panel a shows the integrating sphere with no sample. In panel b), the integrating sphere with the sample inside but indirectly excited by the scattered light of the laser. Panel c) shows the integrating sphere with the sample inside hit directly by the excitation source. Panel d) shows the spectrum of the excitation source for the three measurements. Panel e shows the emission spectrum of the sample for the three configurations, as described in panel a), b)and c).

The i-PLQY of the chosen sample is determined via three consecutive measurements, which are described in Figure 2.8 a,b and c,. In detail, the first measurement (Figure 2.8 a) is performed with the empty sphere in order to measure the incident power on the sample. The second measurement (Figure 2.8 b) is made with the sample inside the integrating sphere but without a direct excitation, thus only the scattered light from the excitation source excites the sample. In this measurement, the sum of scattered excitation light and light emitted by the sample only due to the shattering excitation is detected. The third measurement, Figure 2.8 c, is collected with the sample inside the integrating sphere, directly excited by the light source. In this case, the detector measures the sum of laser light reflected , transmitted, and emitted by the sample.

Figure 2.8 d shows the excitation spectrum in the three configurations. The area under the spectrum is the integral of the curve over wavelength, defined as the photon flux of the excitation source. The quantity *P* can be defined as the area below the emission spectra of the sample (Figure 2.8 e). For the indirect measurement, μ is defined as the fraction of light obtained from the excitation, which is scattered from the sphere wall and is absorbed by the sample. While for the direct measurement, *A* is defined as the light absorbed by the sample, and consequentially *1-A* is equal to light transmitted and reflected.

$$L_B = L_A(1-\mu), \tag{2.7}$$

$$L_C = L_A(1-A)(1-\mu), \tag{2.8}$$

$$A = 1 - \frac{L_C}{L_B}, \tag{2.9}$$

In the direct measurement, the total number of photons that reaches the detector in the sphere ($L_C + P_C$) is equal to the light emitted by the sample due to the scattered radiation and the scattered excitation source $(1-A)(L_B + P_B)$ and the photons emitted by the sample $\eta L_A A$ with η equal to the i-PLQY.

$$L_C + P_C = (1-A)(L_B + P_B) + \eta L_A, \tag{2.10}$$

Solving the equation with respect to η.

$$\eta = \frac{P_C - (1-A)P_B}{L_A A}. \tag{2.11}$$

In order to calculate e-PLQY, the i-PLQY has to be multiplied by the fraction of photon absorbed by the sample.

The system used for the PLQYs measurement is composed by an integrating sphere of 150 mm in diameter coated with Spectralon diffusive painting, a UV led with emission peak at 375 nm and an Avantes spectrometer fiber coupled with the sphere.

2.4.4 Time resolved photoluminescence measurements

Time resolved photoluminescence (TRLT) set-up is composed by different modules, as shown in Figure 2.9.

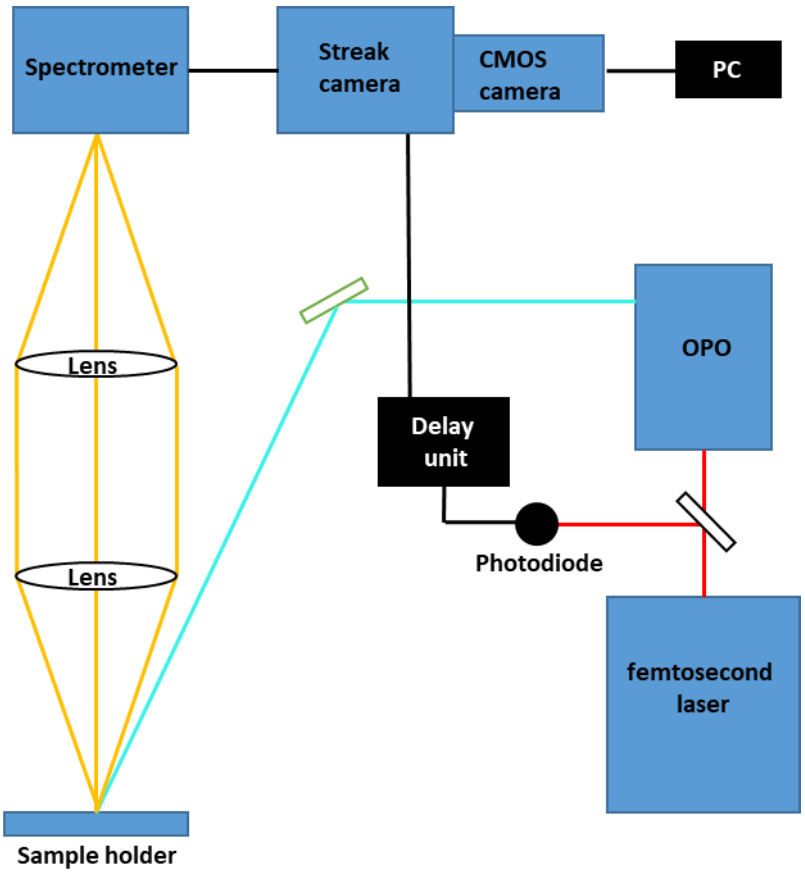

Figure 2.9: graphical representation of the set-up used for TRPL. The light generated by the femtosecond laser is split into two beams: one into the OPO and the other one into the delay unit. From the OPO the beam is directed via a mirror (in green) to the sample holder. The out coming light from the excited sample is concentrated with a pair of lenses into the spectrometer where the light is separated in its different wavelengths and successively to the streak camera for time resolution.

Excitation source: Chameleon Coherent femtosecond laser and Coherent OPO

The excitation source used in the system consists of a femtosecond laser with a frequency of 80MHz, a difference between pulses of 12.5 ns and a pulse width of 100 fs. The laser is used to pump the optical parametric oscillator (OPO). The OPO converts the pump source into two outputs: signal and idler. The sum of the frequencies of the outputs is equal to the frequency of the pump. This phenomenon is obtained via a non-linear optical crystal and an optical resonator.

Sample holder

For fluorescent samples, the sample holder consists of a clamp that keeps the sample in the beam path, while for samples that emit via phosphorescence, the sample holder is a vacuum chamber in order to decrease the excitation quenching due to the oxygen molecules. The dynamic vacuum of $< 10^{-4}$ hPa is maintained via a turbomolecular pump.

Spectrometer, Acton SpectraPro *SP2300*

The spectrometer is equipped with a grating, which separates the light in its different components and allows a wavelength resolution of the light signal.

Hamamatsu Universal Streak Camera C10910

In the streak camera, the light passes through the entrance slits and, after two lenses, it is focused on a photocathode. Here, the photons are translated into electrons via the photoelectric effect. Electrons produced are proportional to the light intensity, and the photocathode ensures the time structure of the light. Then, the electrons pass through a pair of electrodes and are accelerated to a phosphor screen. During this process, the electrons pass through a fast-varying electric field, which deflects them vertically. The electron that passes first is deflected in a different way with respect to the last. In this way, the temporal distribution becomes a spatial distribution. The electrons then hit the microchannel plate (MCP), which enhances their signals for a thousand times, and they are converted back to light within a phosphor screen, as shown in Figure 2.10.

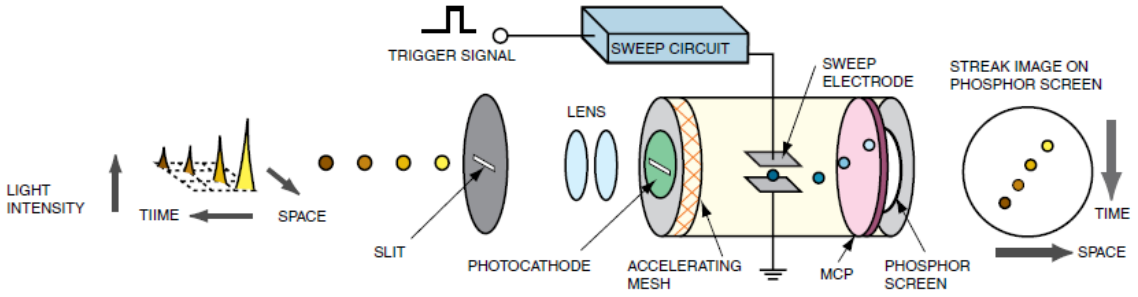

Figure 2.10: schematic representation of working principle of the streak camera. Light passing through the entrance slit is focused via a pair of lenses into the photocathode that converts the photons into electrons [58].

CMOS Camera OrcaFlash4.0 V2

Complementary metal oxide semiconductor (CMOS) camera translates the light signal coming from the phosphorus screen to an electric signal sent to the PC. This kind of camera is equipped with a photodiode and CMOS transistor switch for every pixel, which allows to reduce the noise during the reading of the electric signal and at a higher speed compared to the CCD camera.

Photodiode and delay generator

A part of the light, from the pump laser is deviated via a beam splitter into a photodiode, which translates the light signal with its frequency into an electric signal. Then, this signal is delayed using the delay generator and transferred to the streak camera with the desired delay time.

The resulting spectrum of TRPL is a 3-D graph, with time on the x-axis and wavelength on the y-axis; the different color is used to highlight the intensity of the light at specific time and wavelength. From the 3-D graph, further two 2-D graphs can be extrapolated: lifetime kinetic and lifetime dynamic, as shown in Figure 2.11. Lifetime kinetic provides the relation between light intensity and time, of a specific wavelength or

averaged over a set of wavelengths. The lifetime dynamic provides information about the relation between the light intensity and wavelength for a specific time range.

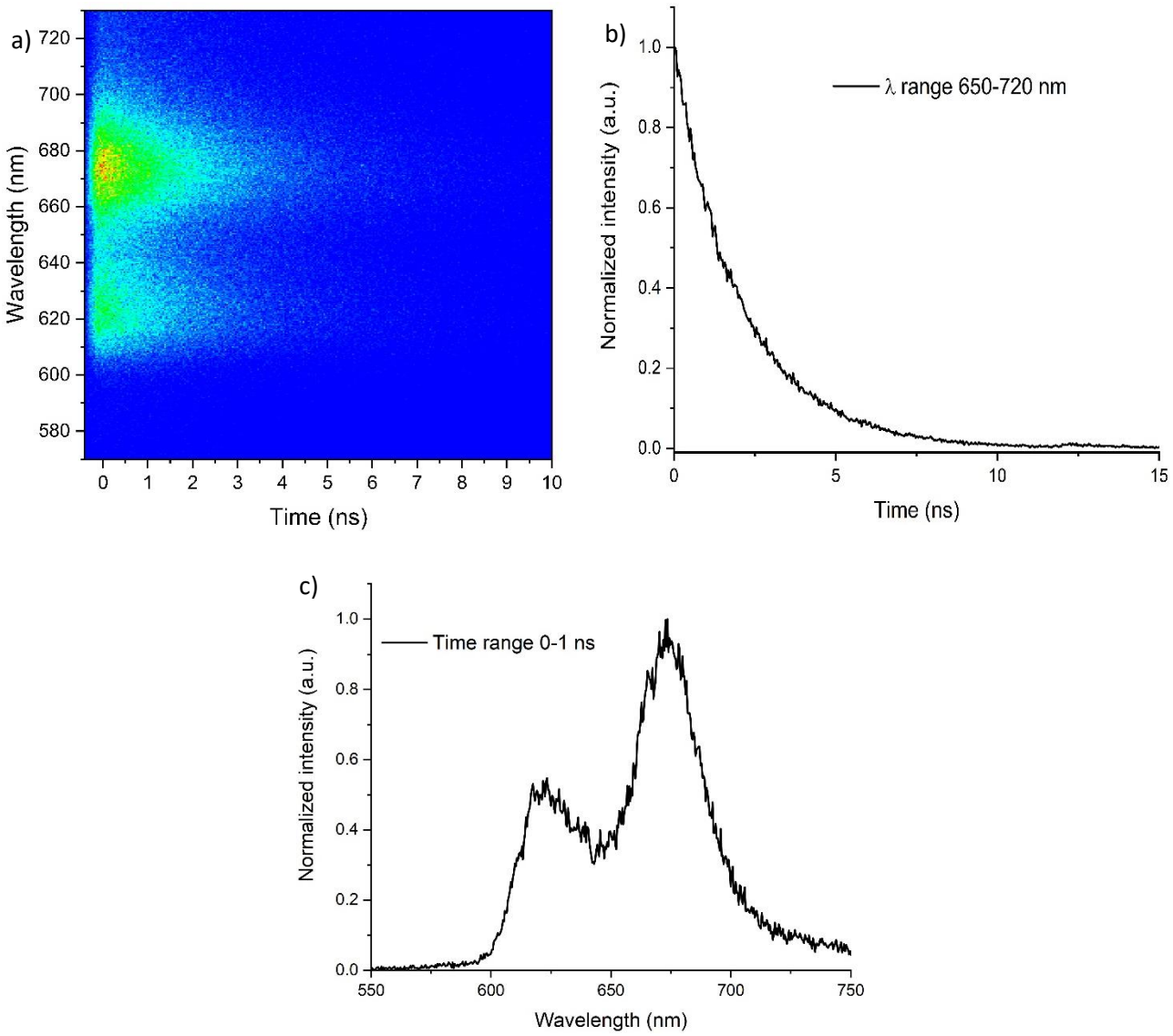

Figure 2.11: panel a) 3-D representation of TRPL of zinc porphyrin at 50 µM in ETOH solution, the time on the x-axis, the wavelength on the y-axis, and the different colors associated to life intensities. Blue color indicates the absence of light, green color a medium intensity and red color a high intensity. Panel b) lifetime kinetic, intensity vs. time for wavelengths between 650 to 720 nm. Panel c) lifetime dynamic, light intensity vs. wavelength for the time range from 0 to 1 ns.

2.5 Synthesis of H_4ETTC

4',4''',4'''',4'''''''(Ethene1,1,2,2tetrayl)tetrakis(([1,1'biphenyl]-3carboxylic acid)) (H_4ETTC) is an aggregation-induced emission dye, which is used as a guest molecule in the loading process inside the SURMOF 2 scaffold in the fourth chapter of this work. It is synthesized following the route presented by Wei *et al*. [41]. The synthesis can be dived into four steps.

The first step includes the synthesis of tetraphenylethene (TPE) from benzophenone using titanium chloride ($TiCl_4$), zinc dust, and tetrahydrofuran (THF); a schematic representation of the reaction is shown in Figure 2.12. The reaction is known as McMurry reaction, where a reductive coupling of ketones forms alkenes is made using a low valent titanium reagent (titanium chloride) and a reduction agent. For the reaction, 5.5 g of benzophenone are added to a 250 ml dry round bottle, then cycling three times vacuum/nitrogen in the flask to remove the residual water present in the powder.

The round bottle is placed in an ice bath and has been added solution (150 ml) of dry tetrahydrofuran (THF) is stirred for 10 minutes. Afterward, 5 ml of $TiCl_4$ are added to the solution drop by drop. After stirring for 10 minutes the zinc dust is added and left stirring for 5 minutes. Then the solution is removed from the ice bath and placed at 75°C in refluxing mode overnight. After the reaction mixture is cooled to room temperature, dichloromethane and water are added. The organic phase is separated using a separating funnel, washed with water three times and dried using magnesium sulfate. After removal of the solvent with a rotary evaporator, the solid is dried overnight. The reaction yield is around 73%, based on the amount of the starting material.

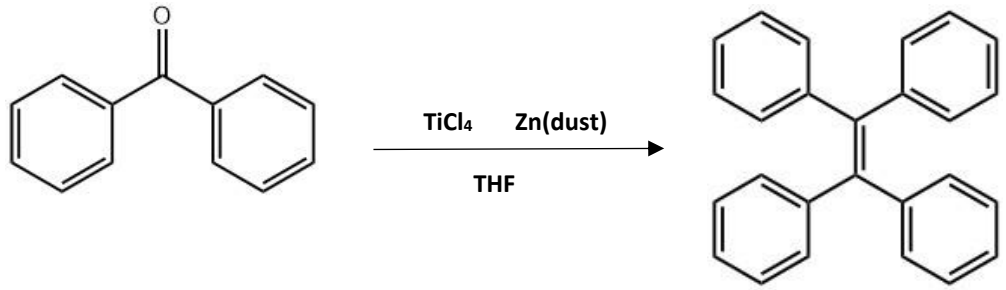

Figure 2.12: 1st step from Benzophenone to TPE.

The second step is the synthesis of Tetrakis(4-bromophenyl)ethane (TPE-Br) starting from the TPE, as shown in Figure 2.13. For this process, 5.0 g of TPE are placed in a round flask equipped with a long condenser and an additional funnel on the top; 8 ml of liquid bromine are placed into the additional funnel and added to the TPE slowly drop by drop. The mixture is left stirring for four days after the product is dissolved in dichloromethane and re-precipitate with methanol. The waste material remains in solution while the TPE-Br precipitates due to its insolubility in the methanol (MeOH). The final product is filtrated and dried overnight. The reaction yield is around 70% based on the amount of the starting material.

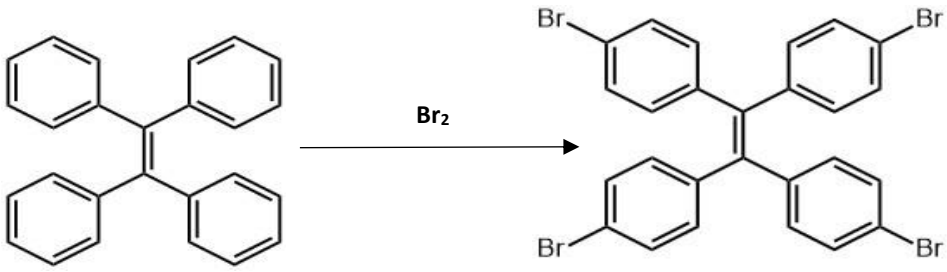

Figure 2.13: 2nd step from TPE to TPE-Br

The third step is the synthesis of Tetramethyl4',4''',4'''',4'''''''-(ethene-1,1,2,2-tetrayl)tetrakis([1,1'-biphenyl]-4-carboxylate) (Me_4ETTC), shown in Figure 2.14. For this synthesis, 1.0 g TPE-Br, 1.6 g of 4-methoxycarbonylphenylboronic acid, 2.8 g cesium fluoride and 0.135 g of tetrakis(triphenylphosphine)palladium are added to a 250 ml round bottom flask with a stir bar then cycling three times vacuum/nitrogen in the flask to remove the residual water present in the powder. Dry dimethoxyethane (DEF) (100 mL) is transferred to the flask, and the solution refluxed for 48 h. After the mixture is cooled to room temperature, the solvent is evaporated and the solid is dissolved in dichloromethane and washed with water. The organic phase is separated and dried with magnesium sulfate. After removal of the solvent with a rotary evaporator, the solid recrystallizes from acetone to yield a light yellow product. The reaction yield is 54.6% based on the amount of the starting material.

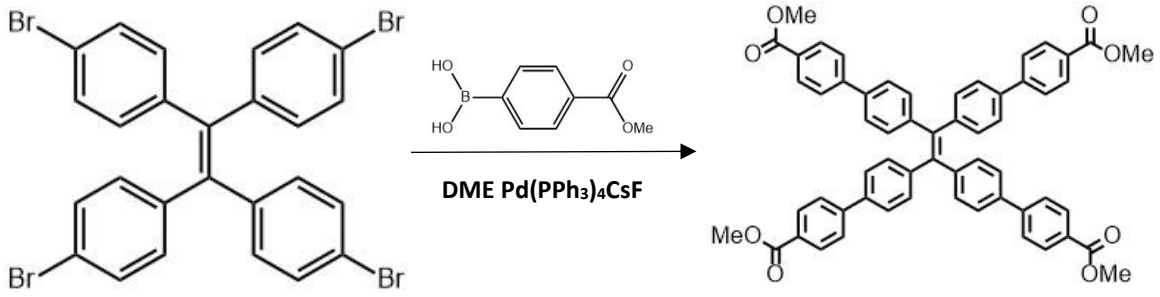

Figure 2.14: 3rd step TPE-Br to Me_4ETTC

The final step is related to the dye synthesis (Tetramethyl 4',4''',4'''',4'''''''-(ethene-1,1,2,2-tetrayl)tetrakis([1,1'-biphenyl]-4-carboxylate))(H_4ETTC). For this purpose, 0.678 g of H_4ETTC and 0.7128 g of sodium hydroxide are added to 100 ml of a mixture of THF, MeOH and water (1:1:1 in volume) and refluxed for one night. Then the aqueous layer is separated from the organic one and Hydrochloric acid (6 M) added to acidify. After filtration, the yellow powder is dried overnight to remove the water. The reaction yield is 86.7% based on the amount of the starting material.

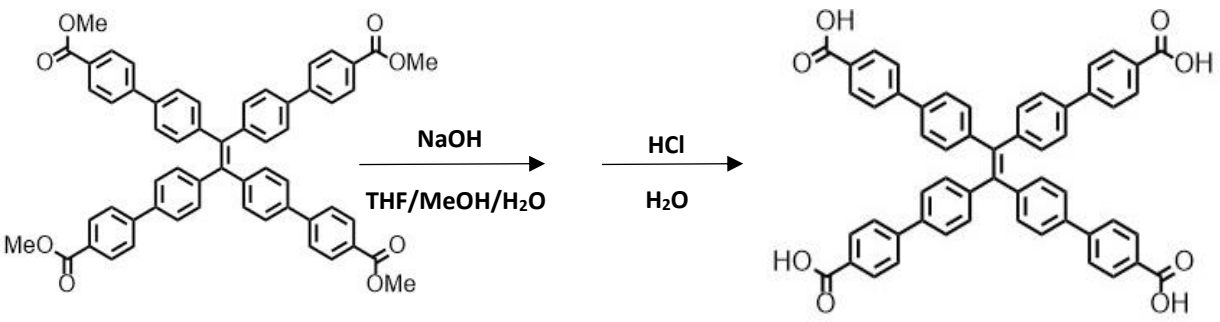

Figure 2.15: 4th step from Me_4ETTC to H_4ETTC

For the last two steps, a first pilot synthesis is conducted using small quantities of reactants to familiarize with the complexity of the reactions and avoid waste of materials. The quantities have successively been increased.

Table 2.1: reaction yields of the third and fourth step related to the amount of starting TPE-Br.

Starting quantity of TPE-Br	3rd step reaction yield	4th step reaction yield
0.2g	47.0%	54.0%
0.6g	54.0%	80.0%
1.0g	54.6%	86.7%

Such scale-up reactions increase the reaction yield, since they are less affected from materials loss during the filtration and transfer between vials.

To verify the products purity, HNMR is performed on the different products of the reaction steps. In this paragraph, for shortness, only the fourth step of the synthesis is presented in Figure 2.14. The other HNMR spectra are enclosed in the appendix (Figure A.1, A.2 and A.3). In order to perform HNMR on H_4ETTC, the dye is dissolved in deuterated dimethyl sulfoxide (DMSO). HNMR spectrum of the synthetized product is in good agreement with the one described by *Wei et al*. [41]. In Figure 2.14, the peaks related to the compound are placed between 7 to 8 ppm, while the peak at 3.34 ppm is the one referred to water in DMSO and the triplet around to 2.5 ppm is related to the DMSO itself.

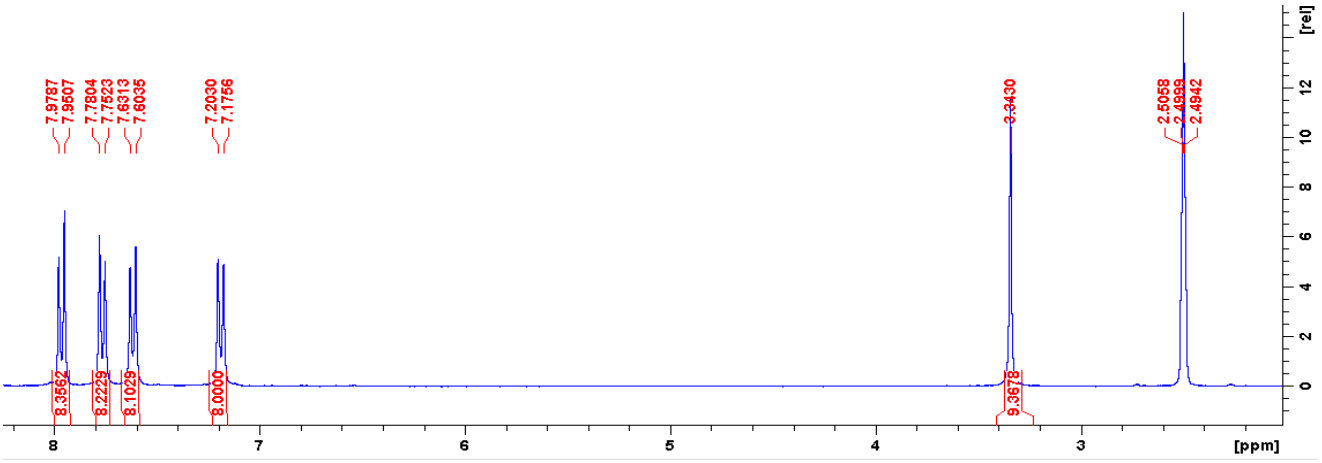

Figure 2.14: 1HNMR of H_4ETTC in deuterated DMSO

2.6 Synthesis of room temperature phosphorescent metal-organic frameworks (MOFs)

Room temperature phosphorescent MOFs are studied in the sixth chapter of this work. Zn-IPA MOF is used as a scaffold to incorporate iridium compound, while the Zn-DTA is a newly synthetized MOF that acquires novel emission properties of room temperature phosphorescence.

2.6.1 Synthesis Zn-IPA MOF

The synthesis of Zn-IPA MOF, described by *Yang et al.* [59] is made via the hydrothermal method where the starting materials are heated up at 150 °C for 24 h in 25ml Teflon-lined stainless steel vessel.

In this work, it has been kept the ratio between the MOF reactants, but Instead of the hydrothermal method, the microwave-assisted synthesis has been used. The microwave gives energy to the chemical process in a homogenous way and without the contact with the heating source. The right microwave frequency brings to collisions of the molecules in solution and to a consequential increasing of kinetic energy and rising of the temperature. The reactions carried on via microwave are faster, and in MOF synthesis, it brings to a faster crystal formation and nanometric crystal size [60]. For the synthesis of the Zn-IPA, we mixed, in a G30 vial (volume of 25 ml), 88 mg of isophtalic acid (IPA), 150 mg of Zinc nitrate hexahydrate ($Zn(NO_3)_2 \cdot 6H_2O$), 82 mg of 2-methylimidazole and 8 ml of water. The mixture is sonicated to dissolve all the components, and the vial is placed inside the microwave reactor for 3h at 180 °C. The corresponding time and temperature for the microwave reactor have been chosen using the manual of the instrument. ($Zn(NO_3)_2 \cdot 6H_2O$) is the metal ion, IPA is the organic linker. The 2-methylimidazole is not present in the final MOF, but it is added to the mixture to help the structure formation. The volume of the vial is kept the same as for hydrothermal method to have the same ratio between the reactant space and the empty space.

2.6.2 Synthesis of Zn-DTA MOF

For the synthesis of the Zn-DTA MOF, 37.5 mg of Zinc nitrate hexahydrate ($Zn(NO_3)_2 \cdot 6H_2O$) is mixed with 22 mg of dithioterephtalic acid (DTA) and 20 mg of 2-methylimidazole in a G10 vial (final volume of 10 ml). The vial is left into the microwave reactor for 3 hours at 180 °C. Such route synthesis is similar to the one applied for Zn-IPA, however for Zn-DTA, the quantities of reactants are reduced, due to the lower availability of materials.

Chapter 3: Dye loading in SURMOF

This chapter is based on parts of this publication:

Nicolò Baroni, Andrey Turshatov, Michael Oldenburg, Dmitry Busko, Michael Adams, Ritesh Haldar, Alexander Welle, Engelbert Redel, Christof Wöll, Bryce S. Richards and Ian A. Howard. Facile Loading of Thin-Film Surface-Anchored Metal Organic Frameworks with Lewis-Base Guest Molecules. Materials Chemistry Frontiers, May 2017, 9, 1888-1894.

This chapter compares the loading of porphyrin dyes with and without carboxylic pendant groups into SURMOF 2 structures. Porphyrins with a variety of metal centers, including palladium, platinum, and zinc, are used. The structure of the samples before and after the loading is characterized by X-ray diffraction. The loading of the molecules is investigated via time of flight secondary ion mass spectroscopy (ToF-SIMS). The loaded samples are characterized by steady-state and time-resolved photoluminescence spectroscopy in order to understand the molecular state of the dyes inside the SURMOF. Only dyes with the carboxylic group are successfully loaded inside SURMOF obtaining a high density of dyes that aggregate within the planes of SURMOF structure.

3.1 SURMOF 2 structure

SURMOF 2 structure is based on a linear linker with two carboxylic groups connected to a paddle wheel metal center with four anchoring points. In this work, zinc (Zn^{2+}) has been used as the metal center, and 1,4-benzenedicarboxylate (BDC) as the organic linker. These two components form a ZnBDC SURMOF. SURMOF 2 structure has a P_4 symmetry [61] and a sheet-like configuration, where for two directions the lattice parameter is given by the organic linker and the third one is smaller. The lattice parameters of the SURMOF can be estimated using XRD measurements. In Figure 3.1, the in-plane and out-of-plane diffractograms provide information on the lattice parameters of the SURMOF.

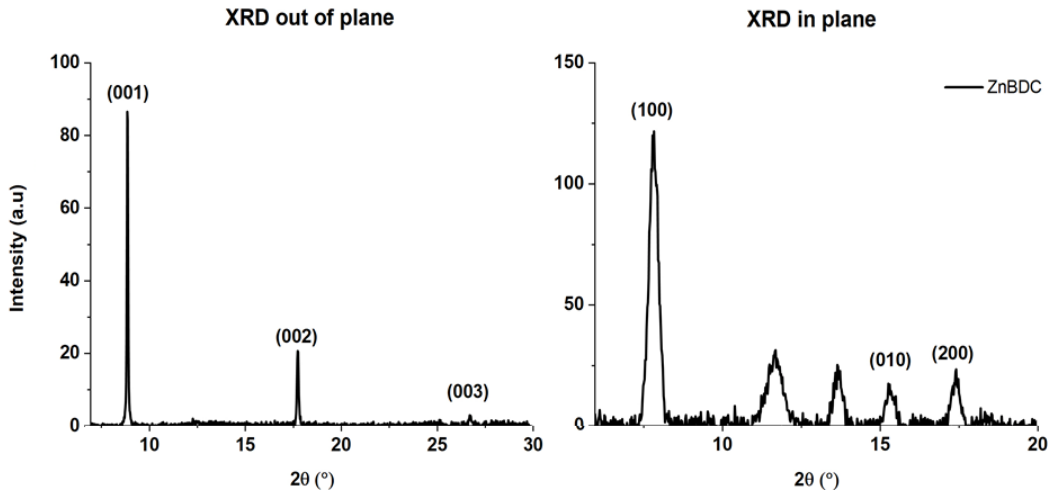

Figure 3.1: out-of-plane and in-plane XRD diffractograms of ZnBDC. The peaks provide information about the lattice parameters of the SURMOF.The (001) at 8.9° peak corresponding to 1.1nm distance, (100) at 8.7° corresponding to 1 nm distance and (010) at 15.46° corresponding to 0.6 nm.

The peak positions in the XRDs can be related to the distance between crystalline planes of the SURMOF structure using Bragg's law. For out-of-plane XRD of ZnBDC, the first order peak (001) is at 8.9°, which corresponds to a distance approximatively of 1.0 nm. Out-of-plane diffractograms show reflections only from one crystal orientation, thus the samples are well-oriented in the direction perpendicular to the substrate.

The in-plane diffractogram, in Figure 3.1, shows two first order peaks, (100) and (010). The (100) is at 8.7 and corresponds to a lattice parameter approximately of 1.0 nm (the same as the spacing in the out-of-plane direction). The peak for (010) is at higher angles, at 15.6° and corresponds to approximatively 0.6 nm. In-plane XRD of ZnBDC shows additional peaks, related to other crystalline orientations due to different crystalline domains. Given the polycrystalline nature in the XY directions, ZnBDC Figure 3.2 shows how the constituents of the SURMOF are arranged in 2D planes and in the 3D structure of SURMOF 2.

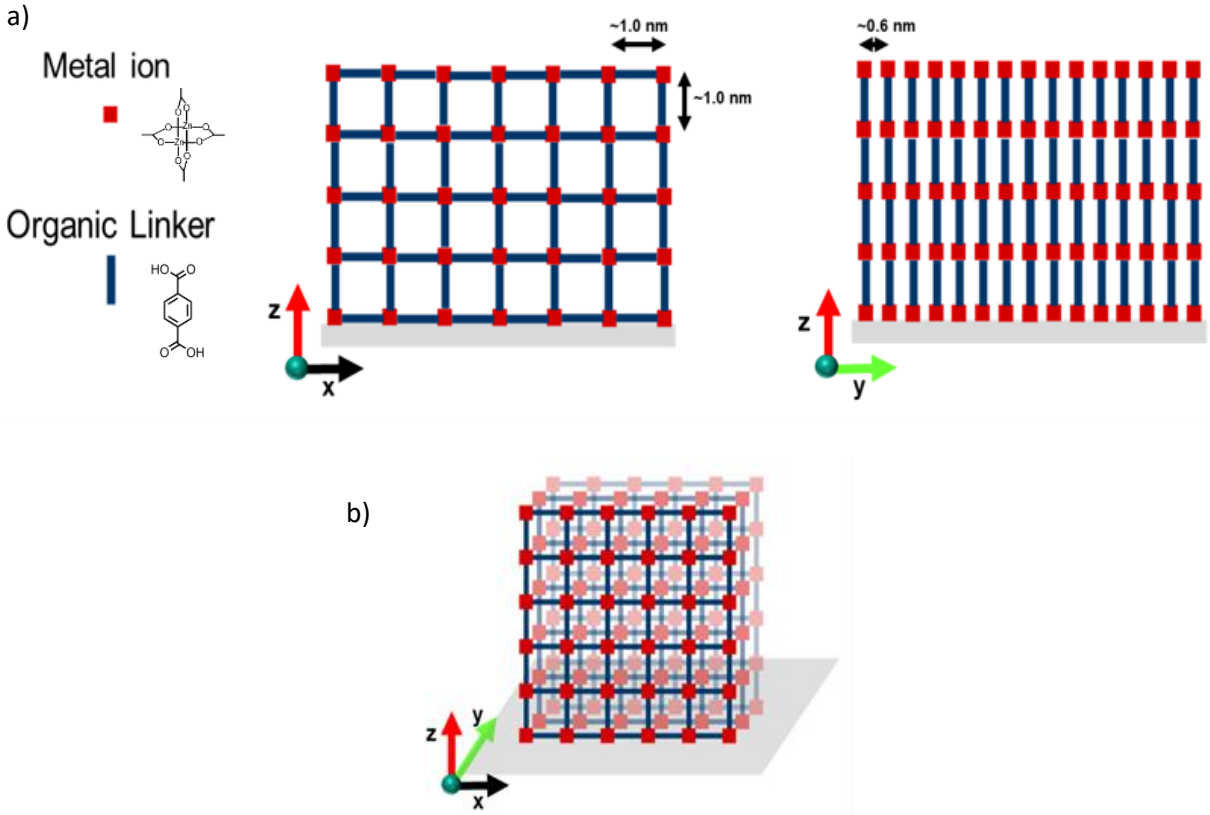

Figure 3.2: Schematics of 2D and 3D views of the SURMOF 2 crystal with lattice spacing obtained by XRD. Panel a) the two constituents of the SURMOF: zinc metal ion and BDC organic linker and 2D representations, XZ plane and YZ plane of the structure configuration of the SURMOF with lattice parameters. The organic linker (~ 1 nm) provides two lattice parameters while the third one is smaller (~0.6 nm). Panel b), the 3D structure of the SURMOF.

CuBDC SURMOF has the same structure of ZnBDC but it is not presented in this work due to the quenching properties of copper metal ion [62]. Dye loaded in CuBDC scaffold will have its emission quenched by the metal ion.

3.2 Porphyrin loading via drop-casting

The first candidates chosen for dye incorporation into SURMOF 2 are porphyrin dyes with different metal centers (zinc, palladium, and platinum) with and without carboxylic groups. Two kinds of porphyrins are loaded inside SURMOF 2 scaffold via drop-casting technique, described in the second chapter.

a)

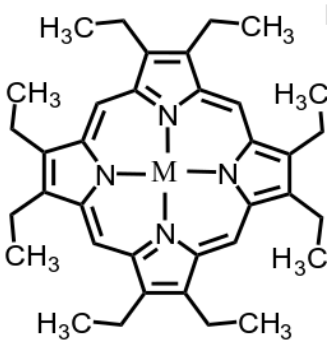

M	Zn	Pd

b)

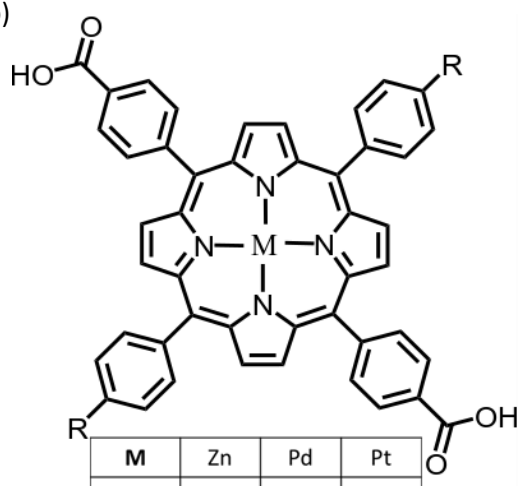

M	Zn	Pd	Pt
R	COOH	H	COOH

Figure 3.3: Panel a) two porphyrins without carboxylic groups with zinc metal center or palladium metal center. 2,3,7,8,12,13,17,18-octaethyl-21H,23H-porphine zinc(II) and 2,3,7,8,12,13,17,18-octaethyl-21H,23H-porphine palladium(II). Panel b), three porphyrins with zinc, palladium or platinum metal centers with carboxylic groups. For the Zn and Pt metal centers are meso-tetra (four-carboxyphenyl) porphine containing 4 carboxylic groups and the structure for the Pd metal center is 5,15-diphenyl-10,20-di(4-carboxyphenyl) porphine with only two carboxylic groups. Pictures adapted from Baroni *et al.* [56].

3.2.1 Proof of dye loading: color change

The variation in samples color is the first effect of the dye loading, as shown in Figure 3.4.

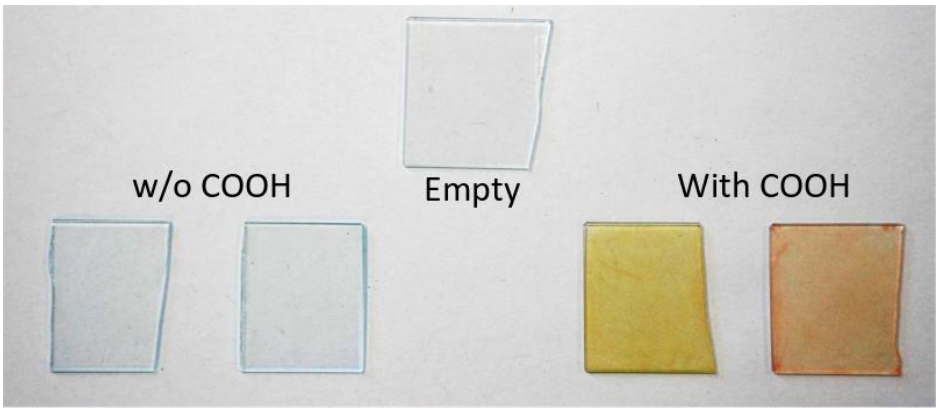

Figure 3.4: Photograph of ZnBDC SURMOF films on glass before and after drop-casting and rinsing. After rinsing, colored films are left for dyes containing carboxylic groups (right), while the ones without functionalization are washed away, leaving the original transparent film (left). Pictures adapted from Baroni *et al.* [56].

Figure 3.4 shows how the samples loaded with carboxylated dyes have changed colors, while the ones without this functionalization are washed away after the cleaning process. Herein, for shortness, the carboxylated porphyrins dyes are referred as Zn-Pr in the case of the porphyrin with zinc as the metal center, Pd-Pr as the one with palladium metal center and Pt-Pr as the one with platinum metal center.

The carboxyl-containing dyes are the ones leaving colored films, and for this reason, they are chosen for a deeper characterization of the loading process.

3.2.2 Proof of dye loading: time-of-flight secondary-ion mass spectroscopy (ToF-SIMS)

ToF-SIMS analysis is performed for a deeper understating of the dye loading and to determine if the dyes are loaded into the SURMOF scaffold or anchored on top of the surface. Figure 3.6 shows the ToF-SIMS analysis on ZnBDC SURMOF loaded with palladium metallated porphyrin. The resulting ToF-SIMS spectrum has four signals. In red, the sum of palladium isotopes (^{104}Pd, ^{105}Pd, and ^{106}Pd), which represents the loaded dye. In black, the zinc isotope (^{66}Zn) signal represents the zinc used as metal center in the SURMOF scaffold, therefore it can be related to the SURMOF. In green, the silicon hydroxide (SiOH) signal characterizes the native silicon oxide generated when the silicon substrate is exposed to air. SiOH signal together with the silicon isotopes signal (^{29}Si and ^{30}Si), in blue, represent the silicon substrate. Furthermore, ToF-SIMS spectrum can be divided into three parts. In the first part (from 0 nm to 25 nm), the palladium signal starts from zero at depth = 0 nm while the zinc signal is already present. The absence of porphyrin dye on the top surface indicates that the palladium dye is washed from the top surface via the rinsing process.

In the second part (from 25 nm to 125 nm), the SURMOF bulk is exposed, and there is a rise in the palladium signal combined with the rise in the zinc signal, confirming an homogenous loading of the sample through all the depth. In the third part (from 125 nm to 150 nm), a decrease in the palladium and zinc signals is found simultaneously with the rise in silicon signal and silicon hydroxide. The sputtering time of the ToF-SIMS process can be related to the depth of the sample, assuming a constant sputtering rate from the ion gun and measuring the thickness of the sample via profilometry. The depth scale is stopped when the interface between SURMOF and substrate (Zn signal decreases and SiOH rises) is reached, from the moment that the eroding rate on silicon oxide and silicon is much slower than the SURMOF and then it is not possible to relate the sputtering time to this part.

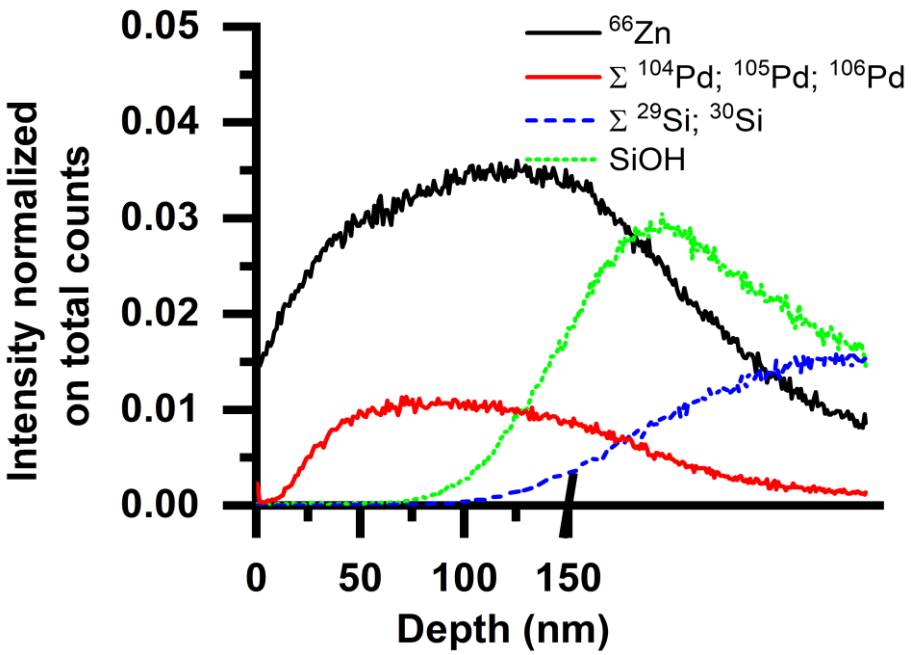

Figure 3.5: Depth profile resulting from ToF-SIMS analysis on the ZnBDC SURMOF loaded with Pd-Pr. There are four signals in the profile. The palladium signal (in red), related to the dye, is absent at the surface (depth = 0 nm) but it is all through the sample depth. The zinc signal (in black) is related to the SURMOF while the silicon hydroxide and the silicon (green and blue) are related to the substrate where the SURMOF is deposited. Picture adapted from Baroni *et al.* [56].

ToF-SIMS confirms that the Pd-Pr dye is loaded through the SURMOF depth and it is not only anchored on the surface. The palladium signal is parallel with the zinc signal, apart from the first nanometers where the palladium is absent. ToF-SIMS is also performed on the ZnBDC loaded with Pt-Pr and Zn-Pr. For ZnBDC loaded with Pt-Pr, Cesium (Cs) has been used as a sputtering ion in order to improve the collection probability of the platinum.

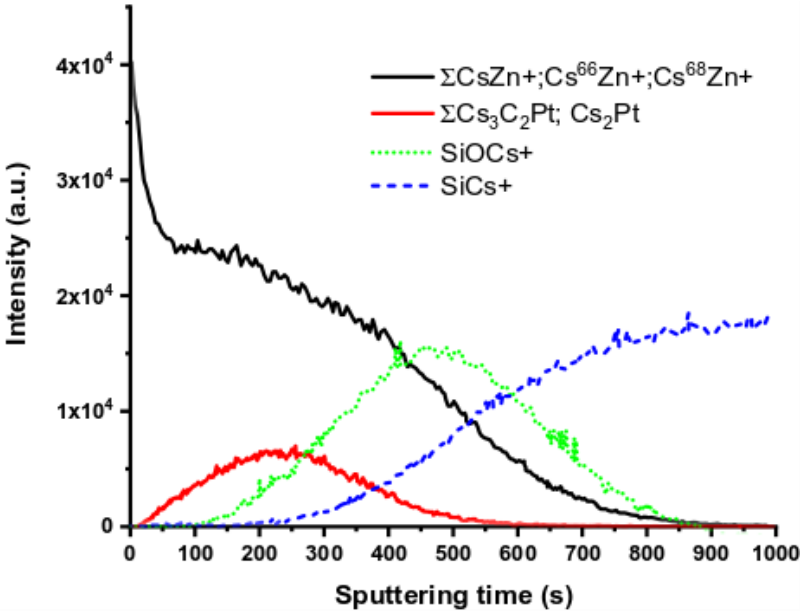

Figure 3.6: depth profile from ToF-SIMS analysis on ZnBDC loaded with Pt-Pr dye. The zinc signal (in black) represents the SURMOF, already present at t=0. The platinum signal (in red), represents the presence of dye, absent at the surface but found in all the SURMOF depth. The silicon oxide signal (in green) rises already at the maximum of Pt signal due to the forward implantation of the Pt atoms in the native oxide layer.

In Figure 3.7, the SURMOF signal, in black, is the sum of the CsZn+, $Cs^{66}Zn+$ and $Cs^{68}Zn+$ isotopes, while the dye signal, in red, is the sum of Cs_3C_2Pt and Cs_2Pt and the substrate signal is the sum of SiOCs+ and SiCs+. ToF-SIMS analysis shows how, as for Pd-Pr, Pt-Pr signal is absent on top of the surface indicating that all the dyes on the top are washed out via the rinsing process. Then the dye signal is parallel respect to the SURMOF signal, which indicates a constant loading through the sample depth. In Figure 3.6, the x-axis is kept as sputtering time because there is no sharp separation between the decrease in the SURMOF and silicon oxide signal. The observed mismatch can be explained via different forward implantations *i.e.,* the Pt atoms are more prone to forward implantation through the SURMOF and hence accumulate at the SURMOF/SiO interface during the erosion and therefore it is not possible to relate the sputtering time with depth.

For ZnBDC loaded with Zn-Pr, the metal from the SURMOF cannot be discriminated from the metal of the dye itself.

In order to understand the effects of the loading on the SURMOF crystal structure, XRD out-of-plane and in-plane are performed on the ZnBDC samples before and after the loading of the metallated porphyrins.

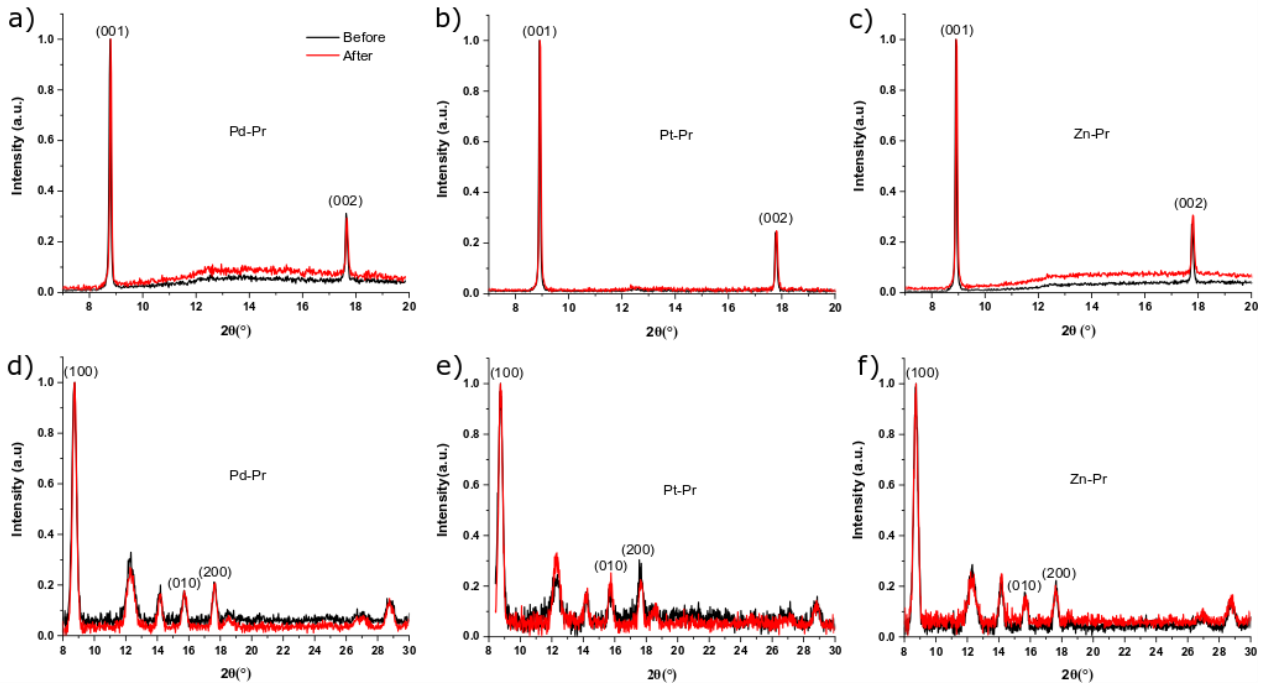

Figure 3.7: panels a),b),c) out-of-plane XRD diffractograms and panels d),e),f) in-plane XRD diffractograms of ZnBDC before (in black) and after (in red) the loading of Pd-Pr, Pt-Pr and Zn-Pr. The crystallinity peaks remain in the same positions before and after the loading indicating that the molecule loading not affect the crystal structures of the SURMOF. The data are partially adapted from Baroni *et al.*[56].

Figure 3.7 shows the diffraction patterns, both for out-of-plane and in-plane, before and after the dyes loading. XRD spectra remain unvaried after the loading, and in particular, the (010) peak, related to the distance of 0.6 nm, between the SURMOF sheets remains unchanged. Therefore, the porphyrin dyes are arranged in a sheet-like configuration, as shown in Figure 3.8, where the dye molecules are loaded between the crystalline planes of the SURMOF, since there is not sufficient space in SURMOF structure to have co-facially arranged molecules [63].

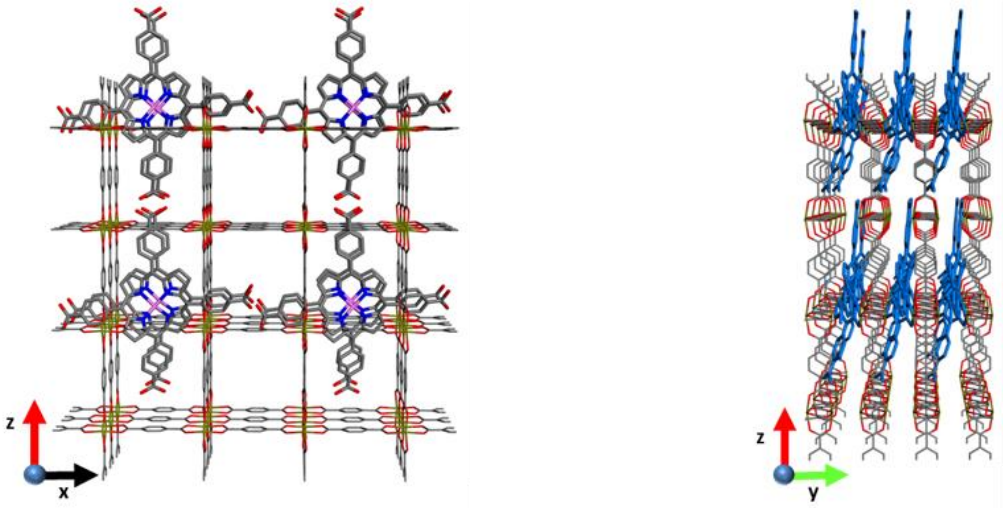

Figure 3.8: schematic representation of metallated porphyrin molecules within SURMOF scaffold. The dye molecules form a layer between the SURMOF sheets. The distance between the SURMOF planes allows intercalating only a single molecule. Picture reproduced from Baroni *et al.* [56].

3.3 Optical characterization

Optical characterization is performed on the loaded samples in order to provide a better understanding of dye state, once it is present in the SURMOF environment.

3.3.1 Absorbance measurements

The absorbance measurements are performed on SURMOF samples before and after the dye loading, and then compared to the absorbance of a dilute solution of porphyrin dye in ethanol (0.1 mM).

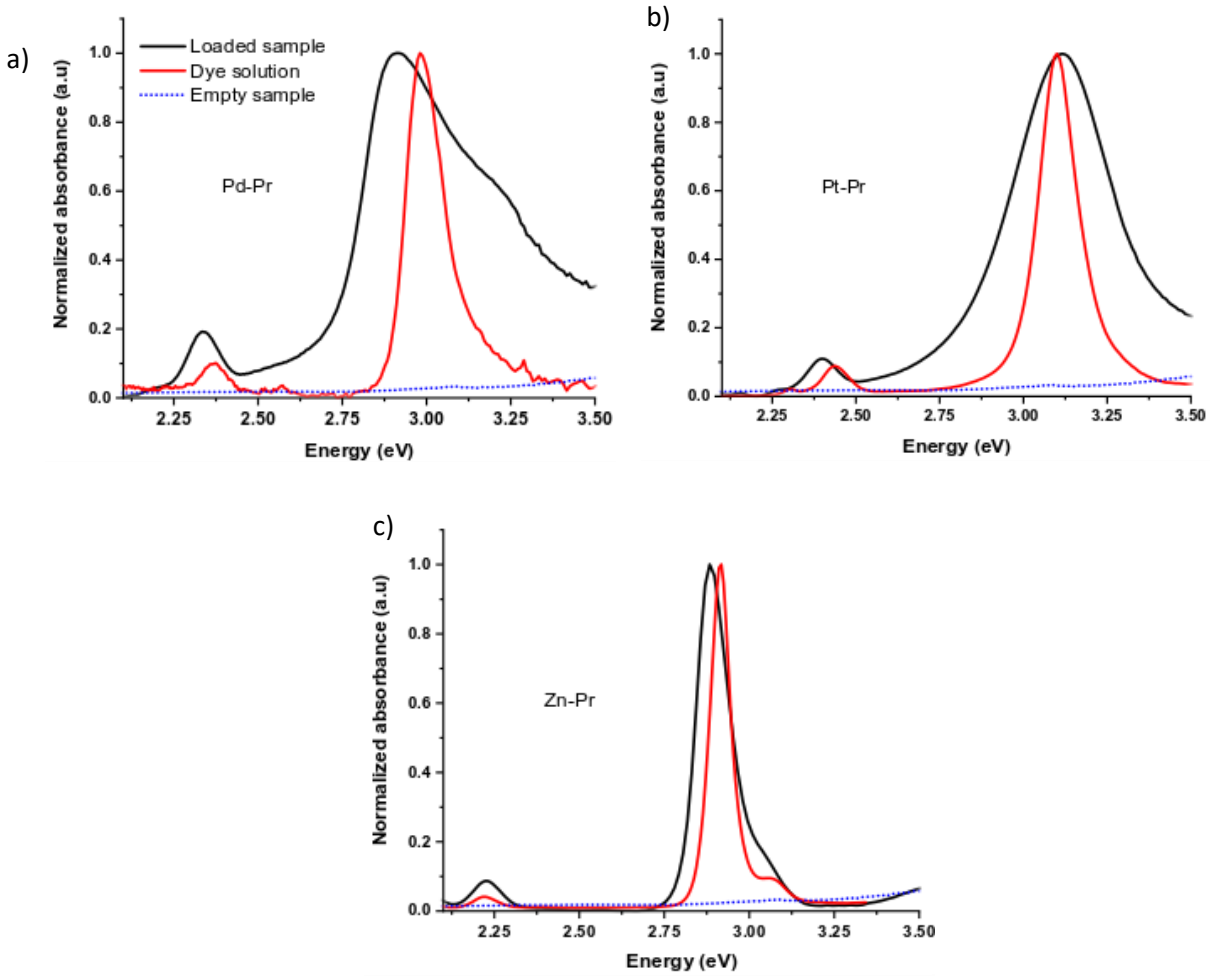

Figure 3.9: In black, the normalized absorbance spectra of ZnBDC loaded with Pd-Pr, panel a), Pt-Pr, panel b), and Zn-Pr dye, panel c) compared with the absorbance of dye solution, in red, and empty SURMOF, in blue. The spectral shapes of the dyes within SURMOF scaffold are broadened and shifted with respect to spectra in solution showing a strong influence of the SURMOF structure on the dye absorbance. Data adapted from Baroni *et al.* [56].

The ZnBDC scaffold modifies the absorbance spectra of the loaded dyes. For all absorbance spectra present in Figure 3.9, two regions can be identified. The first one is associated with the highest energy part of the spectra related to the molecular transition S_0->S_2 corresponding to the Soret band/B-band. The second, at lower energy, is associated to the contribution of S_0->S_1 gives rise of Q-bands. The bands of the dyes are

broadened with a red-shifting in the absorbance peaks of Pd-Pr and Zn-Pr and a blue-shift in the peak of Pt-Pr. Porphyrin molecules possess two transition dipole moments laying in the same molecular plane, one orthogonal to the other. Therefore, the sheet-like structure of the dyes acquired inside the SURMOF leads to the formation of both H- and J- aggregates, as shown in Figure 3.10.

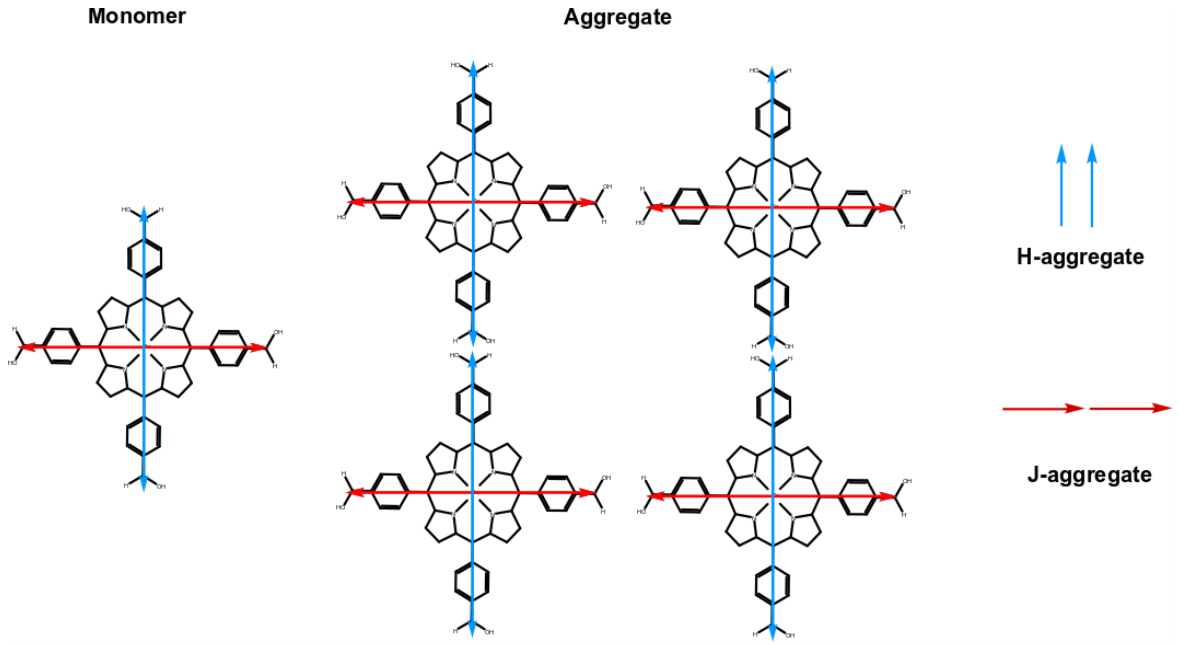

Figure 3.10: schematic representation of a porphyrin molecule with the two orthogonal dipoles that originates H- and J- aggregates, when different molecules are closed together in a plate configuration. Picture adapted from Baroni *et al.* [56].

3.3.2 Time-resolved spectroscopy on loaded SURMOFs

An in-depth investigation through time-resolved spectroscopy is performed in order to study the emission properties of the samples.

For palladium and platinum metallated porphyrins, the presence of a heavy atom in the molecules induces a near-unity yield intersystem crossing, responsible for the excitation transfer from the singlet state to the triplet state with consequent phosphorescence emission. In order to measure the photoluminescence lifetime, the samples are kept under dynamic vacuum (10^{-4} hPa), to prevent the oxygen quenching of the phosphorescence. The samples are excited via a quasi-CW laser combined with an acousto-optic modulator (AOM) giving a square signal at 500 Hz. The samples are excited for 1 ms with the laser, followed by 1 ms of darkness. The streak camera measurement preformed on the Pd-Pr loaded sample is shown in Figure 3.11. Before zero time, the laser is on, with emission from the loaded sample, while after zero time, the laser is turned off and only the long-living component of the emission is left.

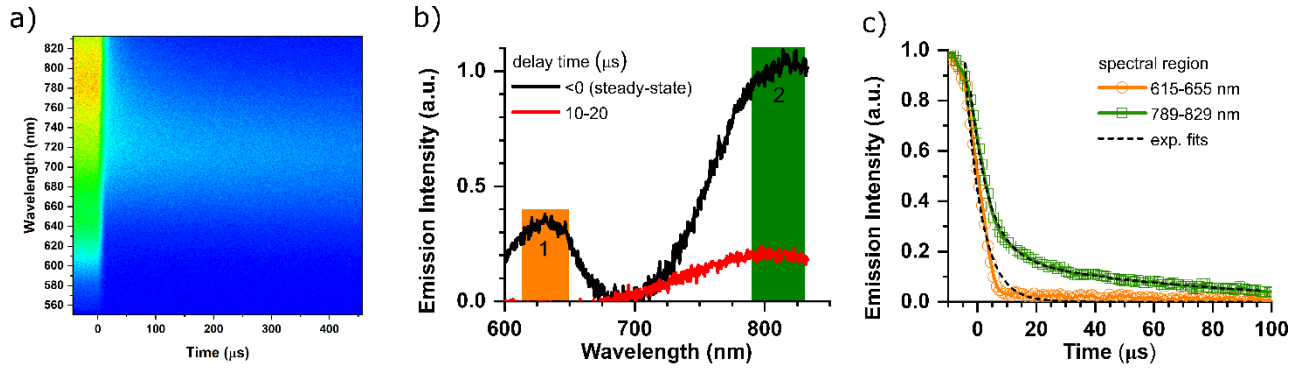

Figure 3.11: panel a) streak camera measurement with excitation wavelength at 410 nm. The strong signal before t=0 is the sum of the signal coming from the laser and the emission of the sample. After t=0, the laser is turned off and the signal comes from the sample only. Panel b) emission dynamic of ZnBDC loaded with Pd-Pr. In black, the steady-state emission and in red the emission in the time interval from 10 to 20 µs. In orange, the first region is indicated as the emission peak related to the monomer and in dark green, the second region is shown as the emission peak related to dye aggregation. Panel c) kinetics of the two spectral regions. In orange, the kinetic of the Pd-Pr monomer from 615 to 655 nm and in dark green the kinetic of the aggregate from 789 to 829 nm. Panel b) and panel c). Data partially adapted from Baroni *et al.* [56].

The lifetime dynamic of emission in the steady-state (before zero time) and between 10 and 20 µs is reported in Figure 3.11 b. The emission spectrum of Pd-Pr is the sum of two peaks: the peak in the first region (from 615 to 655 nm) is the emission from the triplet monomer, while second region (from 789 to 829 nm) is the emission from the triplet aggregate. The monomer has a shorter lifetime than the aggregate, which is still present in the time range from 10 to 20 µs. The lifetime difference between the two components of the emission spectrum can also be appreciated in the kinetics shown in Figure 3.12 c. The monomeric emission (orange curve) has a lifetime approximately of 3.6 ± 0.2 µs strongly quenched with respect to the monomer in solution that is around 1 ms [64, 65], suggesting that the majority of the porphyrins are in the aggregate state. The aggregate emission (green curve) has a bi-exponential decay with an average lifetime of 55 ± 5 µs calculated via $\tau_{av} = (\alpha_1\tau_1^2 + \alpha_2\tau_2^2)/(\alpha_1\tau_1 + \alpha_2\tau_2)$. The aggregate lifetime exceds the one of a triplet aggregate in a solid film, which is 10 µs [66], however most of the triplets are already decayed after 10 µs, as shown in Figure 3.11 b.

Pt-Pr loaded sample displays a similar behavior, as shown by the comparison between the Pt-Pr loaded in the SURMOF and the Pt-Pr embedded in a polymer film of poly(methyl methacrylate) (PMMA) (Figure 3.12), is taken as an example of low concentrated sample. Pt-Pr is a triplet emitter that must be kept under vacuum to avoid oxygen quenching, thus the dye solution cannot be measured with the available set-up. The steady-state emission spectra of the Pt-Pr in polymer film is shown in Figure 3.12 a, and compared to the one is the SURMOF. The SURMOF emission is strongly red-shifted (around 100 nm) with respect to the one in of the dye embedded in the polymer, suggesting a strong aggregation of the dye in ZnBDC. The same information can be extrapolated from Figure 3.13 b, from the comparison of the two kinetics of Pd-Pr in polymer and ZnBDC. The emission decay of Pt-Pr in the polymer film can be fitted with a mono-exponential decay with a lifetime of 45.9 ± 0.2 µs, while the emission decay of the dye in the SURMOF is characterized by a bi-exponential behavior, where the lifetime has two contributions with an overall lifetime of 11.1 ± 0.5 µs. In conclusion, the lifetime of the dye inside the SURMOF scaffold is strongly quenched with respect to the one in the polymer film.

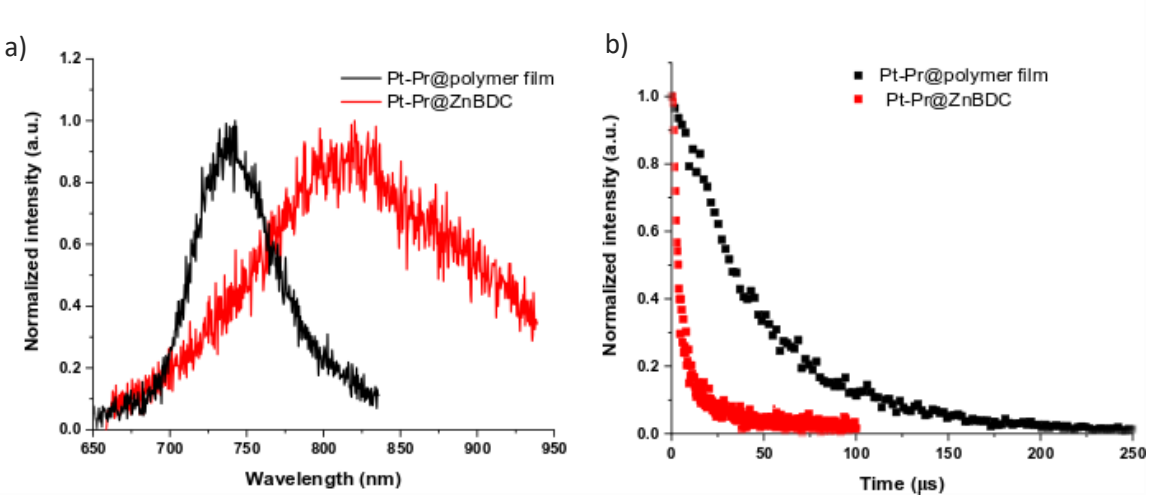

Figure 3.12: time-resolved photon luminescent measurements of a ZnBDC sample loaded with Pt-Pr and of a Pt-Pr in PMMA excited with a 430 nm laser under dynamic vacuum. Panel a) steady-state emissions of Pt-Pr dye embedded in a PMMA (in black) film and within the ZnBDC (in red). The emission of the Pt-Pr@ZnBDC has a strong red-shifting with respect to the one of the Pt-Pr in the polymer film. Panel b) Comparison between the kinetics of the Pt-Pr dye in polymer film (in black) and SURMOF (in red). The kinetic of Pt-Pr in polymer film can be approximated with mono-exponential decay has longer lifetime with respect to the dye in the SURMOF approximated with a bi-exponential decay. Data reproduced from from Baroni *et al.* [56].

For Pd-Pr and Pt-Pr dyes, the obtained results are consistent with previous studies on porphyrins interaction: it has been already observed a red-shifting and a bi-exponential emission behavior for both the singlet and the triplet [66-68]. The Pd-Pr loaded in ZnBDC displays a similar behavior to the one reported by Daniel *et al.* in 2004, where porphyrin aggregate is characterized by a monomer triplet emission around 650 nm and a near infra-red emission originating from the triplet aggregates at 780 nm with longer tail [68]. The zinc metallated porphyrin reveals a fluorescence emission, where the intersystem crossing is slow and cannot compete with emission from the singlet state [69]. However, the emission properties of the Zn-Pr embedded in the ZnBDC scaffold are affected in a similar way as the Pt-Pr and Pd-Pr dyes. The steady-state emission of the dye inside the SURMOF is red-shifted with respect to the one in a solution (50 µM dye in ethanol) and thus losing its features, as shown in Figure 3.13 a. Dye incorporation inside SURMOF modified the emission lifetime as well. The difference in lifetime between the two samples containing the Zn-Pr dye is reported in Figure 3.13 b. The dye inside the SURMOF is characterized by a shorter lifetime with respect to the one in solution: specifically, in solution, the kinetic displays a mono-exponential decay with a lifetime is 2.06 ± 0.05 ns, while the Zn-Pr inside the SURMOF has a bi-exponential decay with an average lifetime of 0.12 ± 0.02 ns.

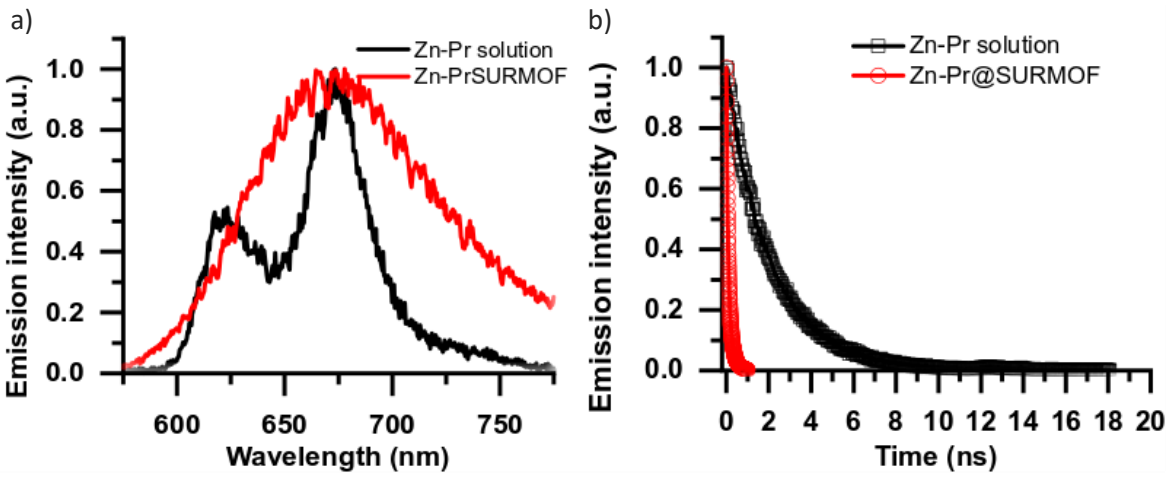

Figure 3.13: time-resolved photoluminescence measurements of the Zn BDC SURMOF loaded with Zn-Pr, excited with a 410 nm under dynamic vacuum. In black, Zn-Pr dye in a 50 µM ethanolic solution and in red, the Zn-Pr loaded in SURMOF. Panel a) Steady-state emission spectra. The emission spectrum of the Zn-Pr in the SURMOF is broadened with respect to the Zn-Pr and red-shifted. Panel b) Kinetics of Zn-Pr in solution in black, and SURMOF in red. The lifetime of Zn-Pr in SURMOF is strongly quenched with respect to the one in solution, due to aggregation.

For all the three dyes considered, the encapsulation in the SURMOF scaffold induces a significant changing in absorption, emission spectrum and photoluminescent life-time. Absorption and emission are broadened with a red-shifting, blue shifting, and the photoluminescent life-time is strongly quenched. These modifications in the dye behaviors are due to a strong dye aggregation within the SURMOF sheets.

Summary

In this chapter, the loading of metallated porphyrin dyes in SURMOF is described. Using the direct drop-casting from ethanol solution, the ZnBDC SURMOF can be selectively loaded with metallated porphyrin molecules with carboxylic groups. Similar dyes with no the carboxylic groups cannot be loaded into the SURMOF showing that the carboxylic pendant groups are essential to bound the dye inside the SURMOF structure and to obtain a high-density loading. ToF-SIMS analysis confirmed the dye loading, showing the presence of the chromophores not on the surface but throughout the whole thickness of the sample confirming that the dyes were loaded between the SURMOF 2 planes. The dye and the SURMOF structures suggest that the only possible configuration of the dye inside the SURMOF is a planar structure between the SUROMF sheets. Drop-casting technique provides remarkable results with respect to the previous loading techniques applied to SURMOFs [53, 70]. Drop-casting process does not required any activation procedure, the loading process is straightforward and fast without any long soaking in the dye solution and without involving any high temperature which, in some case, can damage the SURMOF itself. Optical characterizations are performed on the samples in order to study the behavior of the dyes inside the SURMOF structure and their aggregation state. The absorption and emission spectra have shifted in the peak position and is observed a general broadening. Time-resolved measurements show a reduction of photoluminescence lifetime, also suggesting that dyes aggregate in the SURMOF structure forming both H- and J- aggregates.

Contributions to the chapter

Nicolò Baroni (Author):

- Synthesis, structure and optical characterization of ZnBDC SURMOF and of the ZnBDC loaded samples
- Development of dye loading technique
- Design of the figures and main text

Dmitry Busko and Michael Adams:

- Discussion on optical characterization

Alexander Welle:

- ToF-SIMS measurements

Ritesh Haldar, Engelbert Redel and Christof Wöll:

- Introduction to SURMOF and spray coating technique

Andrey Turshatov and Bryce S. Richards:

- Discussion of the results

Ian A. Howard and Michael Oldenburg:

- Development of dye loading technique and discussion of the results

Chapter 4: Aggregation-induced-emission dye loading in SURMOF

This chapter is based on parts of this publication:

Nicolò Baroni, Andrey Turshatov, Michael Adams, Ekaterina A. Dolgopolova, Stefan Schlisske, Gerardo Hernandez-Sosa, Christof Wöll, Natalia B. Shustova, Bryce S. Richards and Ian A. Howard. Inkjet-Printed Photoluminescent Patterns of Aggregation-Induced-Emission Chromophores on Surface-Anchored Metal-Organic Frameworks. ACS Applied Material and Interfaces 2018, 10, 25754–25762.

Following the results of the previous chapter, in the fourth chapter the characteristics of 4',4''',4''''',4'''''''-(Ethene-1,1,2,2-tetrayl)tetrakis-(([1,1'-biphenyl]-3-carboxylic acid)) (H_4ETTC) are studied, once loaded inside SURMOF 2 scaffold. H_4ETTC belongs to the TPE-family of aggregation-induced emission dyes, switching-on its emission properties when it is embedded in the SURMOF scaffold. If the dyes density loaded in the SURMOF increases, the photoluminescence quantum yield of the emission increases accordingly. The dye in solid-state powder, and SURMOF with higher dye concentration show almost the same photoluminescence quantum yield but with different emission properties, such as emission spectrum and photoluminescence lifetime showing how the SURMOF scaffold plays an important role for an efficient emission of the aggregation-induced emission dye.

In the third chapter, it has been shown that the main effect of the SURMOF 2 structure on the incorporated dye is aggregation. For most of the molecules, aggregation acts as a non-radiative de-excitation channel as described in the first chapter. Metallated porphyrins loaded in the SURMOF are not suitable for the production of optical devices due to the inefficient emission. Emission of AIE dyes is enhanced in solid state, which makes this dyes the perfect candidates to be incorporated in SURMOF 2.

4.1 H_4ETTC dye loading

H_4ETTC has been chosen as aggregation-induced emission candidate essentially for three characteristics. i) Its planar shape, which allows intercalating inside the sheet structure of the SURMOF 2. ii) The carboxylic group that, as highlighted in the previous chapter, is an essential requirement for dye loading in the SURMOF2. iii) The emission properties that can be tuned depending on the degree of aggregation, as shown in Figure 4.1. In solution, H_4ETTC has a bluish emission with an internal photoluminescence quantum yield (i-PLQY) of 2%. On the other hand, in solid-state, the emission is red-shifted, and it is characterized by a yellowish emission with an i-PLQY that reaches the value of 51.2% [71].

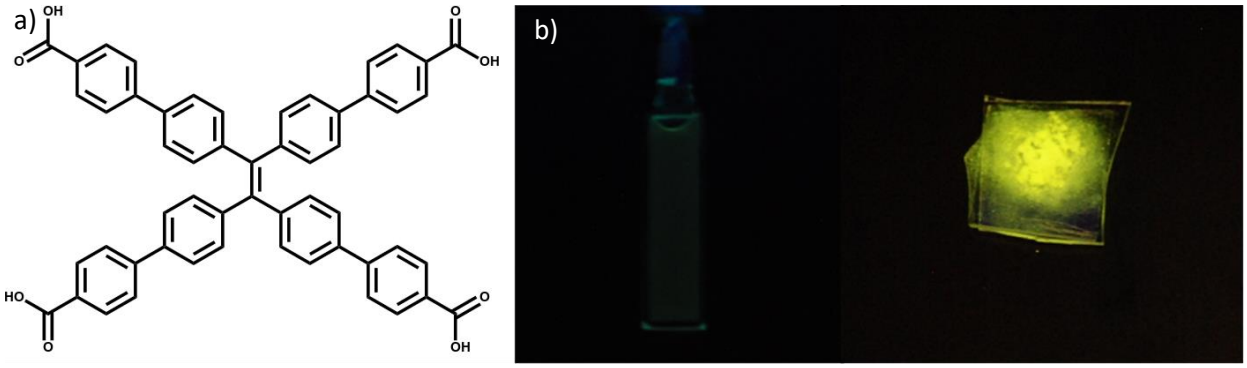

Figure 4.1: panel a) the molecular structure of H_4ETTC, the molecule has a flat shape, carboxylic groups, and tunable emission properties. Panel b), H_4ETTC at 0.1 mM ethanol solution and in solid-state (powder between two glass plates) under UV lamp at 365 nm. The solution results in a weak emission with respect to the strong one of solid-state.

The loading process of the H_4ETTC inside SURMOF follows the same procedure adopted for the metallated porphyrins, described in the second chapter. Figure 4.2 a shows the XRD in-plane of the ZnBDC sample before and after the loading process. The incorporation of H_4ETTC molecules does not interfere with the SURMOF structure, as highlighted by the positions of diffraction peaks in the XRD before and after the loading. . A possible configuration of the dye molecules between the SURMOF planes is shown in Figure 4.2 b and c. Dye molecules have formed planar structures within SURMOF planes.

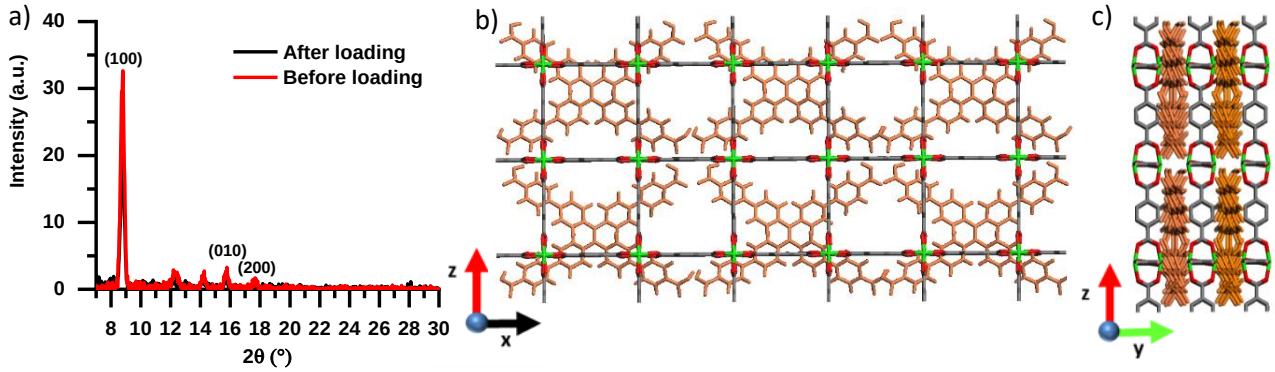

Figure 4.2: panel a) in-plane XRD of ZnBDC sample before and after loading of H_4ETTC. The dye incorporation does not change the structure of the SURMOF. Panel b) 2D representation of H_4ETTC within the SURMOF structure in the XZ plane. Panel c) 2D representation of H_4ETTC in the SURMOF structure in the YZ plane. H_4ETTC molecules form a planar structure within SURMOF scaffold.

Figure 4.3 shows a ZnBDC SURMOF on glass infiltrated with H_4ETTC, under UV illumination (UV LED with emission peak at 375 nm). The sample is characterized by a bright greenish emission. SURMOF structure immobilizes the dyes suppressing the rotational motions of the benzene rings along with the ethane, blocking the non-radiative de-excitation channel of the molecule and switching-on the molecular emission.

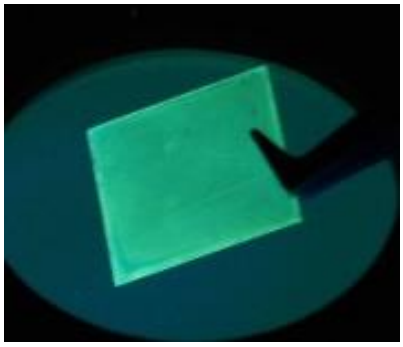

Figure 4.3: ZnBDC loaded with H_4ETTC under UV LED (375 nm) showing a greenish luminescence. Dye molecules, embedded in the SURMOF, are constrained forming aggregates and switching on their fluorescence.

The loading process is repeated in several times in order to increase the amount of incorporated dyes. The samples are drop-casted with 0.2, 0.8, 1.2, 2.5, 3.5 and 4.5 ml of 0.1 mM dye ethanol solution.

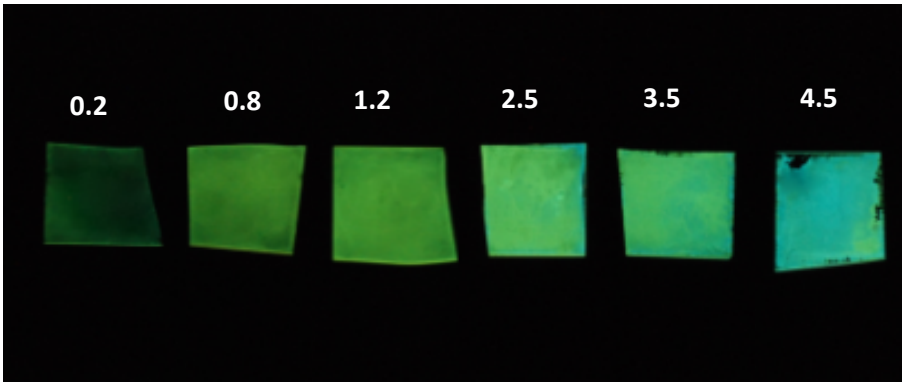

Figure 4.4: ZnBDC samples drop-casted with 0.2, 0.8, 1.2, 2.5, 3.5 and 4.5 ml of 0.1 mM H_4ETTC solution under UV lamp (365 nm). From 0.2 ml to 4.5 mL, a changing in intensity and color emission from greenish to light blue emission is observed. The process is stopped at 4.5 ml because the SURMOF starts to peel off from the substrate. Picture adapted from Baroni *et al.* [71].

With the increasing amount of drop-casted solution, an increase in light intensity from the samples and a change in the color emission is observed, as shown in Figure 4.4. The sample drop-casted with 0.2 ml of dye solution has a weak green emission. The emission intensity starts to increase in the samples drop-casted with 0.8 and 1.2 ml dye solution. From the sample drop-casted with 2.5 mL, the color starts to change until the sample is drop-casted with 4.5 mL, with a light blue emission. The drop-casting process is stopped once reaching 4.5 ml since the loading process starts to peel off the SURMOF from the substrate. The optical properties of these samples are analyzed in detail in the 4.3 paragraph.

4.2 Dye density evaluation

The different quantities of dye solution drop-casted do not provide any real information on the dye density inside loaded SURMOFs since some of the drop-casted dyes are washed via the rinsing process. To

extrapolate the amount of dye loaded inside each sample, they are digested using ethylenediaminetetraacetic acid (EDTA). EDTA is a ligand with six coordination groups (COOH), which can bind the metal ions and remove them from the SURMOF. EDTA allows dissolving the SURMOF structure, maintaining intact the dye molecules.

The samples are digested using a 1 ml of 0.1 M EDTA solution in water. The solution is dropped on top of the loaded samples until the SURMOF is removed from the glass. The action of EDTA is almost instantaneous; therefore, it does not require a prolonged soaking of the samples in the EDTA solution. On the obtained solutions the absorbance is measured and compared with standard samples with known dye concentration.

The standards are produced dissolving an empty SURMOF and adding a known amount of dyes to obtain a solution at known concentrations of 0.2, 0.4, and 0.6 mM. In the UV-Vis spectrophotometer, the samples are measured in the cuvette compartment, where 0.6 mM solution is measured using a 0.1 mm cuvette, instead of a 1 mm cuvette which signal would saturate the detector. Then, the measured absorbance is multiplied by a factor of ten.Figure 4.5 a shows the calibration curve, which correlates the dye concentration with absorbance peak at 290 nm of the solutions. The slope of the linear fitting is the molar extinction coefficient of the H_4ETTC dye in EDTA/waster/SURMOF solution, as described in the second chapter. The molar extinction coefficient is used to calculate the dye concentration in the solutions of dissolved SURMOF starting from their absorbance at 290 nm, as shown in Figure 4.5 b.

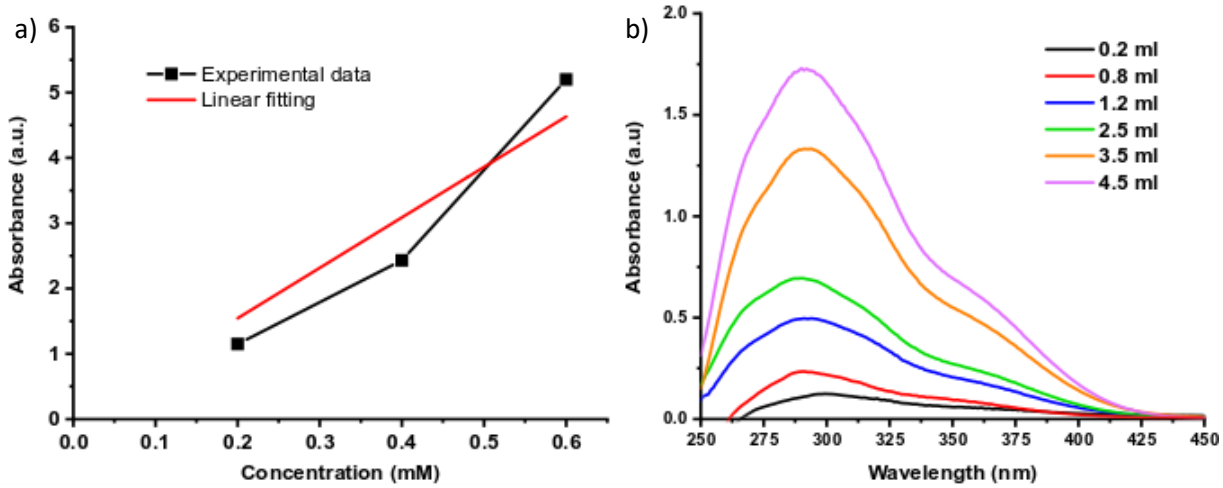

Figure 4.5: panel a) calibration curve for AIE dye dissolved in SURMOF/H_2O/EDTA solution, the experimental data (in black) are made by solution samples with a known concentration of 0.2, 0.4 and 0.6 mM. The curve is correlating the concentration to absorbance at 290 nm of the solutions. The slope of the linear fitting (in red) provides the extinction coefficient to calculate the concentrations of the solutions of the dissolved SURMOF. Panel b) absorbance spectra of dissolved SURMOFs drop-casted with different amounts of dye solution. Higher is the solution drop-casted higher is the absorbance of the sample, indicating a first correlation between the drop-casted solution and absorbance. Figure partially adapted from of Baroni *et al.* [71]

The dye densities inside SURMOFs (mmole/cm^3) are calculated using the concentration of the H_4ETTC solutions. Solutions concentration are calculated as the product between the dissolved samples absorbance @290 nm and the extinction coefficient (7.64 mM^{-1} mm^{-1}) of the dye in EDTA/waster/SURMOF solution.

$$Sol\ concentration\ (mmole/L) = absorbance * extitniton\ coefficent, \quad (4.1)$$

The number of molecules inside the solutions are obtained multiplying the concentration by the solution volume (1 ml).

$$N\ molecules\ (mole) = Concentration\ \left(\frac{mmole}{L}\right) * solution\ volume\ (L), \tag{4.2}$$

The SURMOF volume (Vol_{SURMOF}) is calculated using the area of the substrate (A_{sub}) multiplied by the thickness of the SURMOF (T_{SURMOF}):

$$Vol_{SURMOF} = A_{sub} * T_{SURMOF}, \tag{4.3}$$

Assuming SURMOF thickness as a constant over all the structure and equal to 150 nm and with a substrate area equal to the product of glass density (ρ_{glass} =2.203 g/cm^3), the mass of the substrate (m_{sub}) and its thickness (T_{sub}):

$$A_{sub} = \rho_{glass} * T_{sub} * m_{sub}, \tag{4.4}$$

Then the SURMOF volume is

$$Vol_{SURMOF} = \rho_{glass} * T_{sub} * m_{sub} * T_{SURMOF} \tag{4.5}$$

The dye density is given by:

$$Dye\ density = \frac{N\ molecule\ (mmole)}{Vol_{SURMOF}(cm^3)}. \tag{4.6}$$

Table 4.1: dye density in the loaded SURMOF related to the drop-casted solution

Drop-casted solution in ml	Dye density in mMole/cm^3
0.2	0.2
0.8	0.3
1.2	0.5
2.5	1.0
3.5	1.8
4.5	2.6

Calculations show that an increase in drop-casted solution leads to an increase in the dye density within SURMOF scaffold. The increase in dye density leads to a modification of light emission, as shown in Figure 4.6.

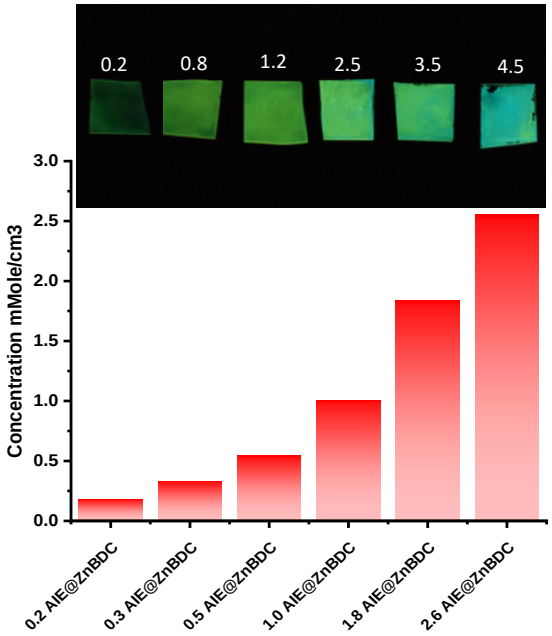

Figure 4.6: dye density correlated to the amount of solution drop-casted on the sample. Increasing the drop-casted solution, an increase in the dye density in the SURMOF is observed. Figure partially adapted from Baroni *et al.* [71].

4.3 Optical characterization

Measurements of internal and external PLQY, absorbance, emission, and TRLT are performed to acquire more information to get a deep insight into the optical properties Vs dye concentration of the synthetized SURMOF.

4.3.1 PLQY

PLQY measurements are performed before the digestion of the samples using the three measurements methods described in the second chapter of this work. The excitation source is a UV LED with an emission peak at 375 nm. The data from the loaded samples are compared with the ones both from 0.1 mM dye solution in ethanol and from the dye in solid-state powder, as a reference of the lowest and the highest values of i-PLQYs respectively, but also for a visual comparison under the UV illumination, as shown in Figure 4.7.

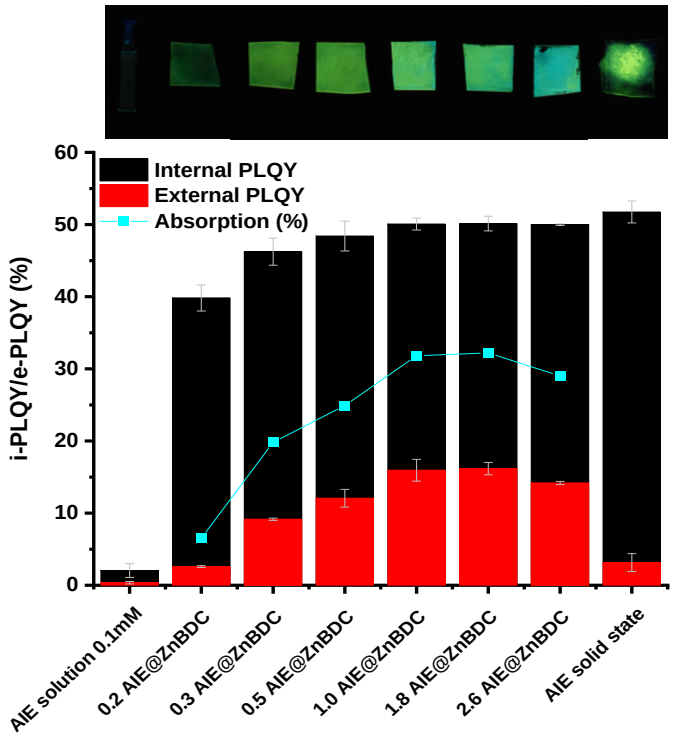

Figure 4.7: AIE@ZnBDC samples compared with H_4ETTC 0.1 mM solution, and H_4ETTC powder, under UV lamp (365 nm). Below each sample, the internal and external PLQY are shown. i-PLQY increases with the increase in dye density, until a saturation point is reached and further addiction of the dyes has almost no effect. The i-PLQY of the highest concentrated sample almost reaches the same value of solid-state powder. e-PLQY follows the same behavior, except in the highest concentrated sample where it decreases due to the lower light absorbed by the sample. Figure adapted from Baroni *et al.* [71].

Figure 4.7 shows an overall increase in internal and external PLQY with the increase in dye concentration. A remarkable increase in i-PLQY and e-PLQY is found already at the sample with the lowest dye density (0.2 mmole/cm^3) compared to the dye solution. i-PLQY rises from 2.0 % in solution, to 40.2 % in the SURMOF, while the e-PLQY increases from 0.4 % to 2.6 %. The packing effect of the SURMOF on the dyes provides an increase of 20-fold for i-PLQY and 5-fold for e-PLQY. The smaller increase in the e-PLQY can be attributed to the moderate absorption of the light by the loaded thin film. These results show that, already at the lower dye density, the SURMOF scaffold plays a critical role in switching on dye emission, obtaining high i-PLQY due to molecular motion restrictions related to the interactions with the SURMOF scaffold.

The growth of both internal and external PLQYs is associated with the increase in dye density. For 1.0 mmole/cm^3, i-PLQY reaches the value of 50.0 %, that corresponds to 25-fold of the value of the solution. The packing increases with the chromophore concentration and an e-PLQY of 15.9 %, equal to 40-fold of the e-PLQY of the solution. With the increase in dye concentration, the dye emission become more efficient. This can be explained via an additional steric hindrance generated by the dyes interaction. Furthermore, the increase in e-PLQY is enhanced by the increase in absorption due to the higher number of molecules involved.

After the 1.0 mmole/cm^3, the further addition of dyes leads to only a slight increase in the i-PLQY, reaching a saturation point where the i-PLQY of the loaded dye is approaching the i-PLQY of the solid-state. After this, the drop-casting of more solutions does not bring to additional enhancement to i-PLQY. An increase in the number of molecules involved and thus in the sample absorbance is observed with the increase in e-

PLQY. In the same way, the decrease in the e-PLQY after 1.8 mmole/cm^3 can be attributed to the lower absorption, as shown in Figure 4.7 in light blue. In the next section, such reduction in absorption will be attributed to a shift in the absorbance peak, and a consequent decrease in absorbed photons of the LED.

The SURMOF scaffold does not interfere in the absorption process from the moment the ZnBDC and AIE dye do not show any overlap between their absorptions, as shown in Figure 4.8. The absorbance of the empty SURMOF is in the range between 250 and 315 nm while the excitation source in PLQY measurements is peaked at 375 nm therefore, in PLQYs measurements there is no excitation of the SURMOF scaffold but only the excitation of the dye. For an excitation source, which excites the SURMOF, the overlap between linker emission and loaded SURMOF can lead to an energy transfer from ZnBDC to AIE dye.

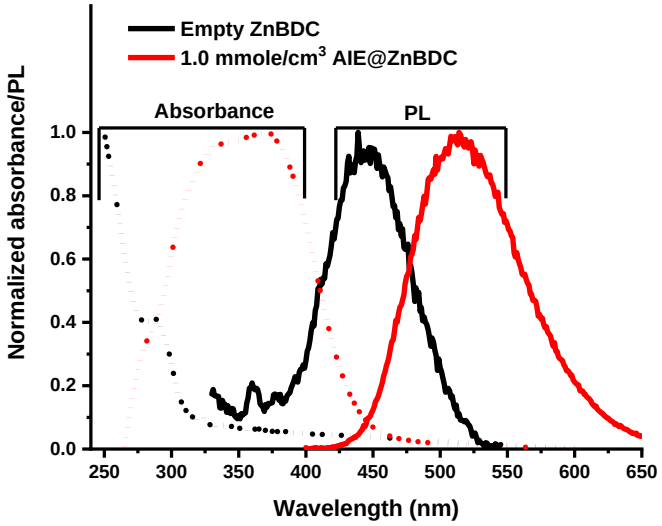

Figure 4.8: absorbance and photoluminescence of empty ZnBDC and 1.0 mmole/cm3 AIE loaded ZnBDC. The empty SURMOF does not absorb in the wavelength range of the excitation source; therefore, it does not play any role in the PLQYs of the samples. When SURMOF is excited, the overlap between emission of SURMOF empty and the absorbance of the loaded SURMOF can lead to energy transfer between the two components of the sample. Figure adapted from Baroni et al. [70].

4.3.2 Absorbance and emission characterization

In this section, the effects of the increase in the loaded dye concentration to absorbance and emission of the AIE dye molecule embedded in the SURMOF are studied.

Figure 4.9 shows the normalized absorbance of ZnBDC loaded with different dye density compared with the ones of 0.1 mM dye solution and the one of dye in solid-state (powder). A red-shifting in the absorbance is found Increasing the dye concentration, indicating a high density in the dye loading as a result of two contributions. i) The vibrational motion constraints by the SURMOF scaffold and ii) the presence of the other adjacent AIE dyes. Dye solution shows a series of vibronic peaks in the visible spectrum that is maintained in the loaded SURMOF where a change in the ratio between the strength of vibronic peaks is observed. Samples with higher dye concentration have stronger low energy vibronic peaks. These observations are consistent with the molecule adopting a similar ground-state structure in solution and in

the SURMOF, however in the SURMOF the rigidity of the surroundings effectively constrains the molecule to stay in a configuration less deformed causing the activation of lower vibrational energy states.

This geometrical constraint is further increased with the concentration of guest molecules, explaining the domination of the lowest energy vibronic peak in the samples with higher loading. The absorbance spectrum of the dyes in the SURMOF is also different from the one of solid-state as crystalline powder indicating that the ground-state molecular structure of the intercalated dyes differs from the normal, 'propeller-like' configuration of such TPE-based AIE dyes in the solid-state. In SURMOF, the preferential configuration to intercalate the dyes between SURMOF sheets is the planar configuration.

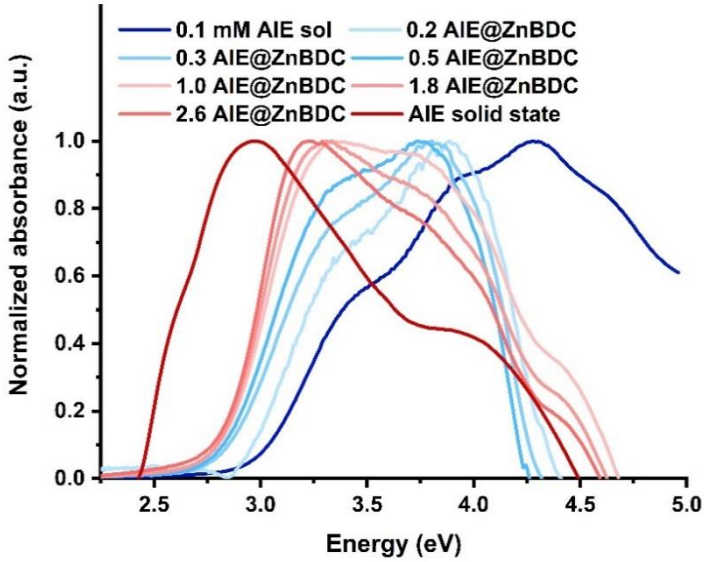

Figure 4.9: normalized absorbance spectra of AIE loaded SURMOF with different dye densities compared with dye in 0.1 mM solution and solid-state (powder). Increasing the dye concentration, a red-shifting in the absorbance spectrum of the loaded sample is observed. The ratio between vibronic peaks of the spectrum can differ depending on the number of loaded molecules, showing that the geometrical constraints of the SURMOF together with the increase in the number of the molecules are able to induce a change in the absorbance spectra. Data reproduced from Baroni *et al.* [70].

Moreover, the emission spectra change with the increase in dye concentration. The emission shifting is not monotonic, but it is characterized by a red-shifting up to the concentration of 0.5 mmole/cm^3 followed by a blue-shift up to the highest concentration, almost reaching the emission of the one in solution. Figure 4.10 a shows the comparison between the loaded samples and, as a reference, the emission of AIE dye in solution (having highest energy emission in deep blue) and the emission of solid-state powder (with lowest energy emission in deep red). The sample with the highest dye concentration has an emission spectrum similar to the AIE solution while the i-PLQY approaches 50%, similar to the value in solid-state. High PLQY indicates a rigid configuration of the molecules, although the emission properties indicate a difference from the solid-state powder. The progressive change in the emission peaks is shown in Figure 4.10 b. A similar emission behavior can be found in aggregates of TPE based metallocages that aggregate, adding a non-solvent to the solution. In the metallocages, the dye is immobilized with a configuration different from the one in solid-state, having high PLQY but different emission [72]. This is an additional confirmation of the strong aggregation of the dyes inside the SURMOF, provided from dye-MOF interaction and dye-dye interaction, but with a different configuration compared to the solid-state.

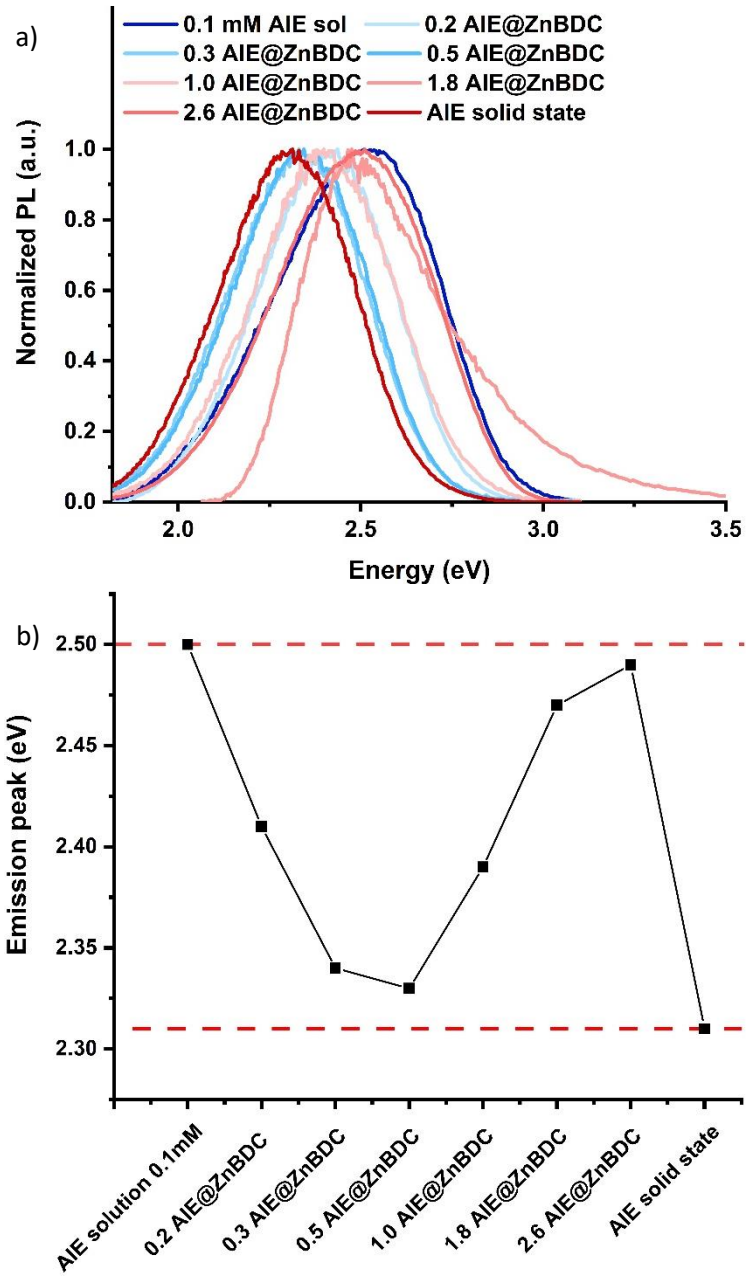

Figure 4.10: panel a) normalized photoluminescence of ZnBDC loaded with different dye densities. In deep blue, the emission spectrum of 0.1 mM AIE dye solution and in deep-red the emission of powder solid-state. Panel b) the behavior of the emission peaks of the loaded samples. Emission peaks do not have a unique behavior; they start with a red-shifting in the low concentrated samples reaching almost the peak position of the solid-state then blue-shifted approaching the solution emission peak. The dashed lines highlight the emission peaks limit of the solid-state and solution. Data adapted from Baroni *et al.* [71].

The energy difference between the half-rise of the absorption spectrum and the half-rise of the emission spectrum can be identified as a quantity related to the Stokes shift and indicating the loss in energy between the absorbed and emitted photons, mainly affected by two factors. First, a higher difference can be found with an increase in the reorganization of the molecule between the ground and excited-state geometries. Second, a higher energy difference can be found increasing the inhomogeneous broadening of the energy levels and the energy transfer in the solid-state. On the other hand, in H4ETTC, the energy difference between absorption and emission decreases from solution to the SURMOF and further

decreases with the increase in the dye concentration. This behavior provides the evidence that the dyes inside the SURMOF are not in the powder form with the increasing concentration, but there is an increase in steric interaction between the dye molecules and the SURMOF scaffold and between the dye molecules themselves.

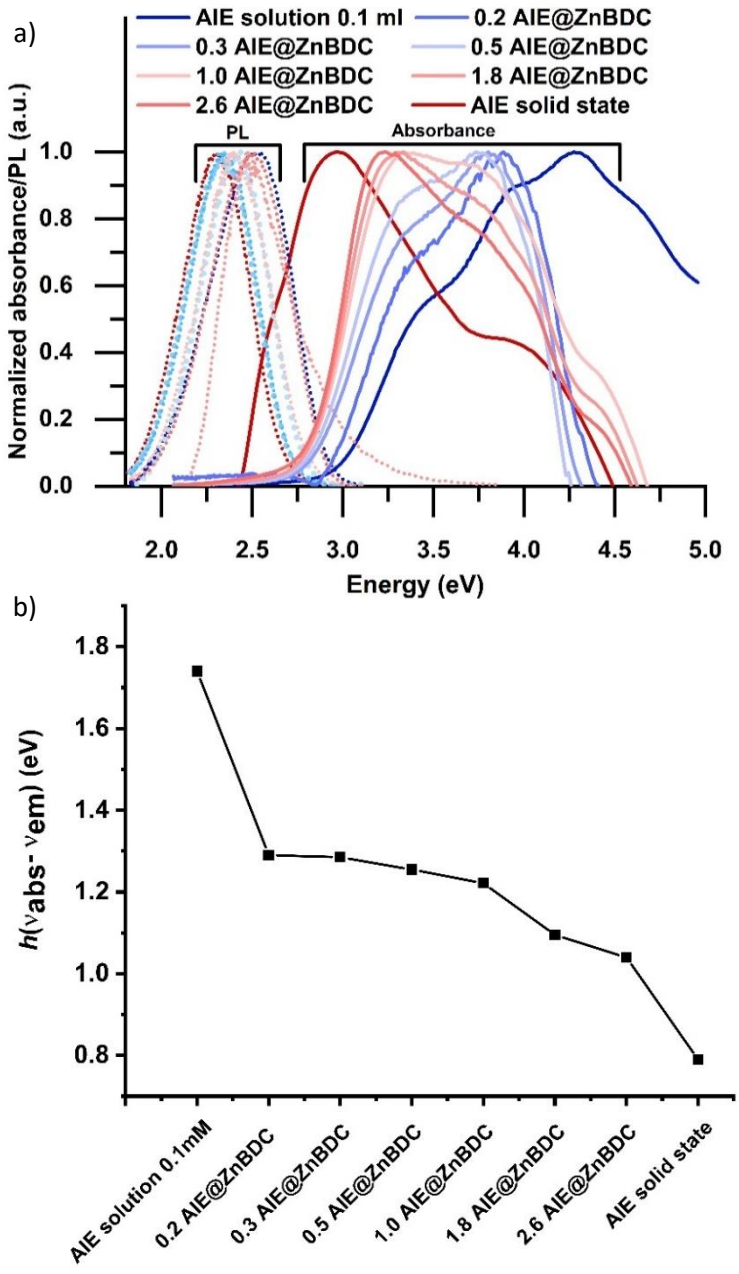

Figure 4.11: panel a) comparison between normalized emission and normalized absorbance of SURMOF loaded with different dye density, 0.1 mM dye solution and dye in solid-state. Panel b) The shift in energy between the half-rise of the absorbance and the peak of the emission energy depending on amount of AIE chromophore loaded into the SURMOF. The difference decreases with the increase in dye concentration due to the increase in the stiffening of the molecules. Data adapted from Baroni *et al.* [71].

A further investigation on the origin of the phenomena has been conducted performing time-resolved PL. Figure 4.12 shows the lifetimes of AIE dye solution (monoexponential decay with $\tau = 150$ ps) and solid-state (bi-exponential decay with $\tau_1 = 139$ ps and $\tau_2 = 614$ ps) in dark blue and dark red respectively, compared with the ones of SURMOF loaded with the highest (bi-exponential decay with $\tau_1 = 93$ ps and $\tau_2 = 375$ ps), in light blue, and lowest dye density (bi-exponential decay with $\tau_1 = 124$ ps and $\tau_2 = 630$ ps), in light red. At the lowest concentration, the PL lifetime is closer to the solid-state powder as found for the emission spectra, where the emission peak is closer to the solid-state. When the SURMOF is loaded with an high dye concentration, the lifetime shortens and approaches the one in solution, also following the same behavior of the emission spectrum where the emission peak moves to higher energies as the one in solution. The difference in lifetime between the most concentrated sample and the solid-state is the experimental evidence which confirms that the SURMOF environment holds the AIE to turn-on their bright emission with an emissive state that differs from the one of solid state.

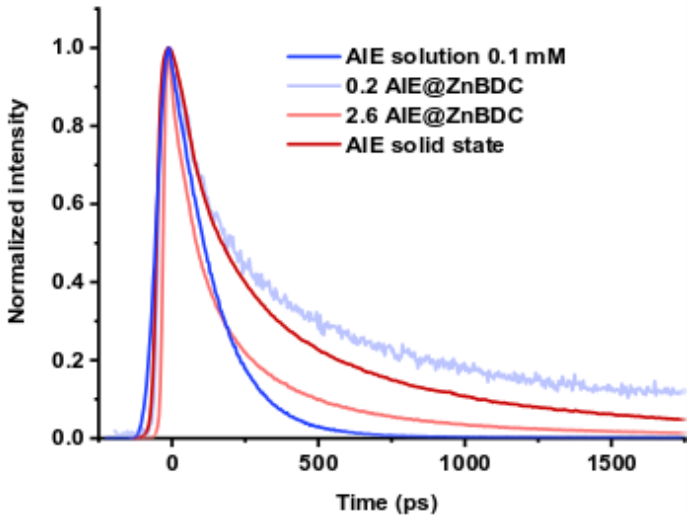

Figure 4.12: Time-resolved PL decays showing the lifetime of the emissive state in the AIE dye-loaded SURMOFs compared to that in solution and solid-state (powder). At low dye density, the excited-state lifetime is similar to that in the solid-state. On the other hand, at high concentrations the lifetime is shorter and similar to the solution. The different lifetimes of emitting states between the highest concentration and the solid-state is further indication that the nature of the emitting states are different. Data adapted from Baroni *et al.* [71].

The optical analysis provides the final proof that the AIE dyes are intercalated between SURMOF sheets rather than anchored onto the surface. In the case of chromophores attached on the SURMOF surface forming a dense film, the optical properties of the loaded samples should approach the ones of the solid-state. However, the loaded samples show an absorption, emission and photonluminence lifetime which differs from the solid-state. On the other hand, the i-PLQY almost reaches the one of the solid-state showing that the SURMOF structure holds the molecules tied sufficiently to switch on their luminescence.

Summary

The fourth chapter shows the loading of AIE chromophores inside the SURMOF 2 scaffold via direct drop-casting. The density of dyes between SURMOF sheets is found to increase with the amount of drop-casted solution on top of the SURMOF. i-PLQYs of the loaded samples is shown to reach an high value already at the low concentrated samples indicating that the SURMOF plays an important role in switching on the luminesces of the dyes. In detail, the SURMOF is blocking the molecular motions and thus reducing the non-radiative channels of the AIE molecules. i-PLQY of the highest concentrated sample reaches almost the i-PLQY of the dye in its solid-state. e-PLQY increases as well due to the increase in the light absorbed, reaching 15.9% for the highest concentrated sample, which is characterized by a dye density of 2.6 mmole/cm^3. Absorbance, emission and PL lifetime show distinct shifting with respect to the solid-state providing the final proof that the dyes are not anchored on the top of the SURMOF surface as a solid-state film but loaded in the SURMOF. The achieved results are relevant in terms of dye density loaded and emission properties of the samples. Previous works on dye loading in SURMOF have shown emission detectable only with optical microscope [53].

Contributions to the chapter

Nicolò Baroni (Author):

- Synthesis, structure and optical characterization of ZnBDC SURMOF and of the ZnBDC loaded samples
- Synthesis of H_4ETTC dye
- Design of the figures and main text

Ekaterina A. Dolgopolova and Natalia B. Shustova:

- Introduction to the synthesis and characterization of H_4ETTC dye

Dmitry Busko and Michael Adams:

- Discussion on optical characterization

Ritesh Haldar and Christof Wöll:

- Discussion on SURMOF

Andrey Turshatov and Bryce S. Richards:

- Discussion of the results

Ian A. Howard:

- Development of dye loading technique and discussion of the results

Chapter 5: Device application

This chapter is partially based on parts of this publication:

Nicolò Baroni, Andrey Turshatov, Michael Adams, Ekaterina A. Dolgopolova, Stefan Schlisske, Gerardo Hernandez-Sosa, Christof Wöll, Natalia B. Shustova, Bryce S. Richards and Ian A. Howard. Inkjet-Printed Photoluminescent Patterns of Aggregation-Induced-Emission Chromophores on Surface-Anchored Metal-Organic Frameworks. ACS Applied Material and Interfaces 2018, 10, 25754–25762.

This chapter shows two device applications of the SURMOF 2 structure loaded with the aggregation-induced emission dyes H4ETTC. The first one consists of a precise loading of the AIE dye in the SURMOF scaffold using different printing methods. Over the three methods presented, the one that allows making a precise pattern is the inkjet-printing, reaching feature size down to 70 µm. The second application is as an active film in thin-film luminescent solar concentrator (LSC). Here, SURMOF shows scattering properties that, together with the total internal reflection of the dye emission, increase the light output from the edge reaching efficiencies, which is a fourth of traditional LSC.

The fourth chapter has shown how the SURMOF 2 structure can be infiltrated with aggregation-induced emission dye. SURMOF substrate loaded with AIE dye can be applied as a down-converting layer for LED, and in particular, under the condition of making a precise pattern of the dye, it can be used in the field of displays with the chance to compete with new technologies as printed quantum dots [73]. The properties of aggregation-induced emission dye combined with the fast and easily scalable deposition of the SURMOF can be applied for producing thin film luminescent solar concentrator.

5.1 Display application: dyes patterning on the SURMOF

In order to print dyes patterns on the SURMOF substrate, three different approaches have been investigated:

5.1.1 Dye patterning via drop-casting mask

The first method for dye patterning includes a plastic mask attached to the top of the SURMOF during the drop-casting process. The mask allows for the infiltration of the dye solution only in certain portions of the SURMOF.

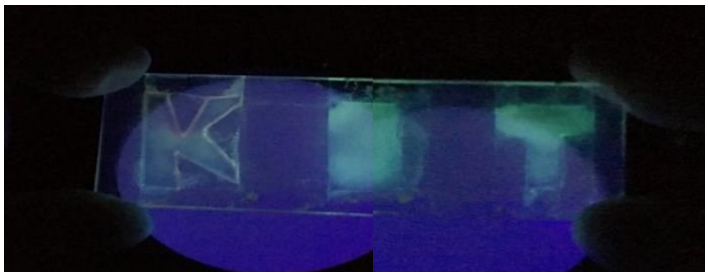

Figure 5.1: SURMOF sample coated with a plastic mask during the loading process in order to form the KIT logo. The solution undergoes the mask showing an unexpected loaded portion of the sample.

Figure 5.1 highlights the main problem of this technique, since the dye solution undergoes the plastic mask and infiltrates other portions of the SURMOF, resulting in an imprecise dye pattern.

5.1.2 Dye patterning via mask during SURMOF spraying.

In the second method considered, a different approach is used: instead of inducing a dye pattern on the SURMOF, the SURMOF itself has been patterned. The dye molecules can penetrate the SURMOF and are removed from portions containing only glass, during the rinsing step. The SURMOF pattern is produced using a plastic mask attached to the glass substrate during the SURMOF spraying.

Figure 5.2 a shows an exemplification of the mask used for inducing a pattern during the SURMOF spraying. In black, the part of the SURMOF covered by the mask and in light blue the part exposed to the sprayed solution. The drop-casted dye solution is spread all over the sample surface and then rinsed with ethanol. Figure 5.2 b shows how AIE chromophores are retained only in part coated with the SURMOF while the part with bare quartz glass is clear after the rinsing step. This result is an additional evidence that the dyes are loaded into the SURMOF structure and not only deposited on the surface.

This method resulted in a better resolution in the printed structure compared to the previous one, without any evident leaking of the solution, mainly due to the directionality of the spraying process. Figure 5.2 c reports in detail the edge between SURMOF and quartz glass showing that the edge has still some imperfections and it is not straight.

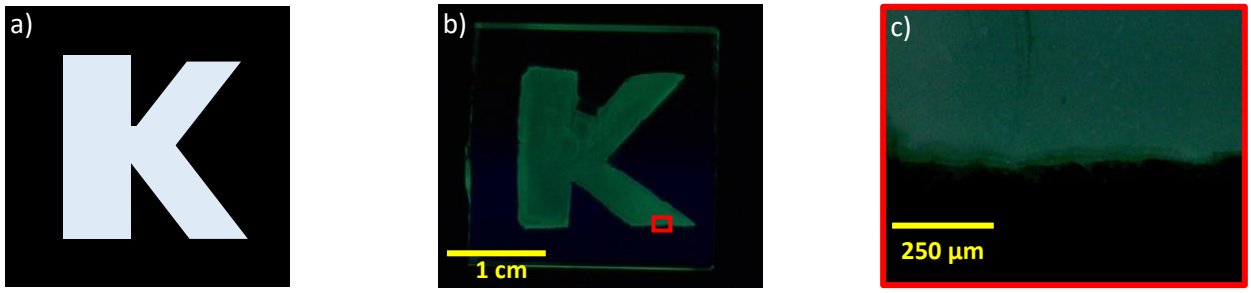

Figure 5.2: panel a) scheme of the mask used during the spraying deposition. In black, the part of the sample covered by the plastic mask and in light blue the exposed part of the glass substrate able to receive the reactant solution. Panel b) SURMOF patterned with "K-shape" and loaded with AIE dye under UV illumination. Panel c) magnification of the structure in panel b) with an optical microscope under UV lamp (365 nm). Picture reproduced from Baroni *et al.* [71].

5.1.3 Dye patterning via inkjet-printing

The inkjet-printing processes are performed at the Innovation Lab in Heidelberg with the cooperation of Dr. Stefan Schliβke under the supervision of Dr. Gerardo Hernandez-Sosa.

The last method for dye *patterning* performed in this work is the inkjet-printing. The functional material chosen for deposition is dissolved to form an ink and then it is loaded into a printhead that releases a fixed amount of ink through a nozzle, Figure 5.3 a. The ink solution in the shape of a droplet falls via gravity on a substrate, Figure 5.3 b, where, after the heating process used to remove the solvent, forms the desired

pattern, Figure 5.3 c. The main difference of the inkjet printing with respect to the other deposition methods is that the pattern can be obtained directly without involving any masks in the process.

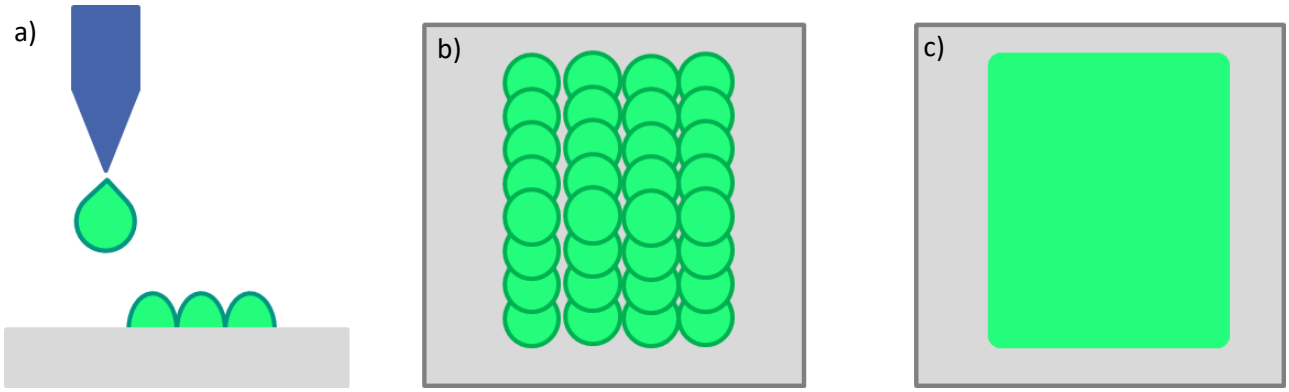

Figure 5.3: panel a) the droplet of the ink are released from the printhhead, in blue, and deposited onto the substrate, via gravity, in grey. Panel b) the ink droplet are deposited on the substrate in the desired position. Panel c) after heating the solvent is removed from the ink to have the final shape of the patterning.

The Inkjet-printing technique is an established technique in thin-film deposition, widely used for a fast and low cost deposition on a large area. In the past, inkjet-printing has been used for several applications in different fields. In 2007, Hoth *et al.* used inkjet-printing in organic solar cell fabrication, focusing on the deposition of the active layer mixture of poly(3-hexylthiophene) (P3HT)blended with fullerene [6,6]-phenyl C61 butyricacid methyl ester (PCBM) dissolved in a Tetra-lene and oDCB:mesitylene [74]. An additional application of inkjet-printing is in the field of organic light-emitting diode (OLED) with the demonstration of high controllability in the deposition of red green and blue OLED derived from the inkjet-printed dopants of tris(4-methyl-8-quinolinolato)Al(III) ($Almq_3$) [7]and DCM (4-(dicyano-methylene)-2-methyl-6-(4-dimethylaminostyryl)-4H-pyran) on the PVK buffer layer [75].

Two kinds of inkjet-printing can be distinguished depending on the method of drop ejection: continuous inkjet printing (CIJ) and drop on demand (DoD) inkjet printing. In CIJ, the ink is continuously dropped on the substrate, and the drops pass through a system of charging plates inducing charges in the droplets. The charged ink droplets are deflected to the desired position with a variable electromagnetic field. When the ink is not required, the flow of droplets is not deflected and is recollected in a recirculation system. In DoD, on the other hand, the ink ejection is not continuous but is regulated via a piezoelectric transducer that is biased via a voltage waveform. The deformation of the piezoelectric element induces the emission of the droplets from the nozzle, as shown Figure 5.4 b. The piezoelectric element changes from idle position to a shrink shape in order to induce a pressure in ink and start the jetting. When the pressure from the piezoelectric is released, the ink is released. In this work, the DoD inkjet-printing has been chosen preferred with respect to CIJ, due to the production of smaller drops and for the higher precision in the drop positioning [76].

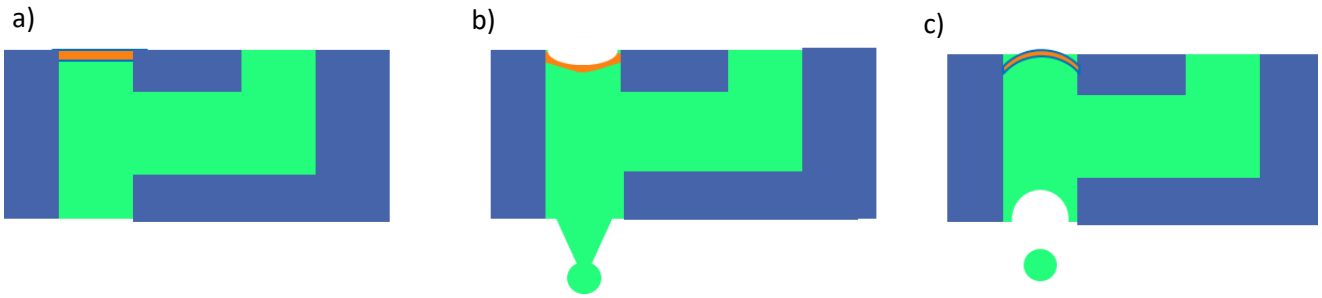

Figure 5.4: representation of ink droplet generation inside the printhead. In orange the piezoelectric component, in green the ink solution and in blue the walls of the prinhead. Panel a) the piezoelectric element is in the idle configuration no ink is released. Panel b) the piezoelectric element receives the voltage impulse, changes its configuration inducing a pressure in the ink, and starts to produce the droplet. Panel c) the piezoelectric elements returning to its starting position is removing the pressure and the droplet is released.

The most critical parameters in inkjet-printing are related to the jettable ink and includes: viscosity, density, and surface tension of the ink. Low viscosity is needed in order to have a fast refill of the reservoir (around 100 ms), thus the ink can be pushed out from the nozzle via pressure transient. The viscosity should be maintained in the range of 1-25 mPa·s. The surface tension should be sufficiently high in order to prevent unwanted ink dripping from the printhead, although low enough to allow the droplet to spill from the nozzle. For these reasons, the optimal surface tension should be between 25-50 $mN \cdot m^{-1}$ [77].
To fulfill these requirements, a solution of 2-butoxyethanol has been added to the stock solution of 0.1 mM H_4ETTC ethanol solution has been (2-butoxyethanol corresponding to 30% volume).
In this work, the Inkjet printer used is the Dimatix DMP-2831 inkjet printer equipped with Fujifilm Dimatix 10 pl cartridge at a maximum jetting frequency of 1 kHz with a custom-designed waveform and a drop spacing of 25 µm at ambient conditions. The printing process is performed under cleanroom conditions (20 °C, 50% RH) and the substrate and the printhead are kept at 25 °C. After the printing process, the samples are transferred into a vacuum oven for 10 min at 15 mbar [71]. Finally, the samples are rinsed with ethanol, as described in the second chapter, to remove the unreacted ink.

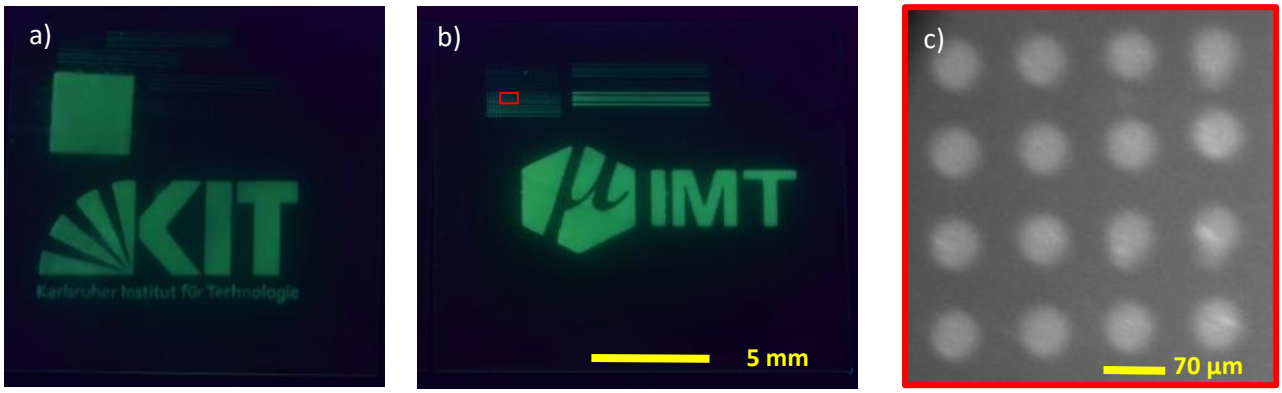

Figure 5.5 panel a) and b) patterns of AIE chromophore on SURMOF substrate under UV lamp (365 nm). Panel c) optical microscope magnification of the structure in figure 5.5 panel b) in red square. Figure reproduced from Baroni *et al.* [71].

In this work, the inkjet-printing has been successfully applied allowing to "write" with AIE ink different patterns on the SURMOF substrate (shown in Figure 5.5), similar to the result of a normal inkjet-printer on

paper. Such application of SURMOF has not been reported previously. Figure 5.5 a shows the logo of the Karlsruhe Institute of Technology (KIT) and some smaller features such as a square structure and dotted lines. Figure 5.5 b shows the Institute of Microstructure Technology (IMT) logo with smaller features as a sequence of dots and lines. In Figure 5.5 c (corresponding to the red square of Fig. 5.5 b) the detailed structures at higher magnification under optical microscope are reported in Figure 5.5 c. The ink-jet printing method allows writing features with a minimum diameter of 70 µm, which consists of a single droplet from the printhead.

5.2 SURMOF based Luminescent solar concentrator

The second device application for SURMOF loaded with AIE dye is the production of a thin film SURMOF-based LSC. As described in the first chapter, in order to obtain a thin film LSC, SURMOF 2 is deposited via spray coating on top of a borosilicate slab (5.00 x 5.00 x 0.55 cm) glass BOROFLOAT® 33 from Schott. This kind of glass has been chosen for the low absorption from AIE dye and for the material flatness of the top and bottom faces. The edges of the sample are polished to have flat edges, as well. On one edge, a monocrystalline silicon solar cell strip (0.5 x 6 cm), provided by National Renewable Energy Center (NaREC), is attached via bi-component glue, , covering all the edge surface. The silicon solar cell has an efficiency of 14.7 % (under standard condition and AM1.5 global) and its I-V curve and EQE are reported in the appendix in Figure A.4 and A.5. The part of the solar cell that exceeds the edge is covered via black tape in order to avoid light from other source rather than the LSC. SURMOF 2 is deposited via spray coating on the borosilicate glass and then is infiltrated with AIE dyes using the drop-casting technique as described in the previous chapters.

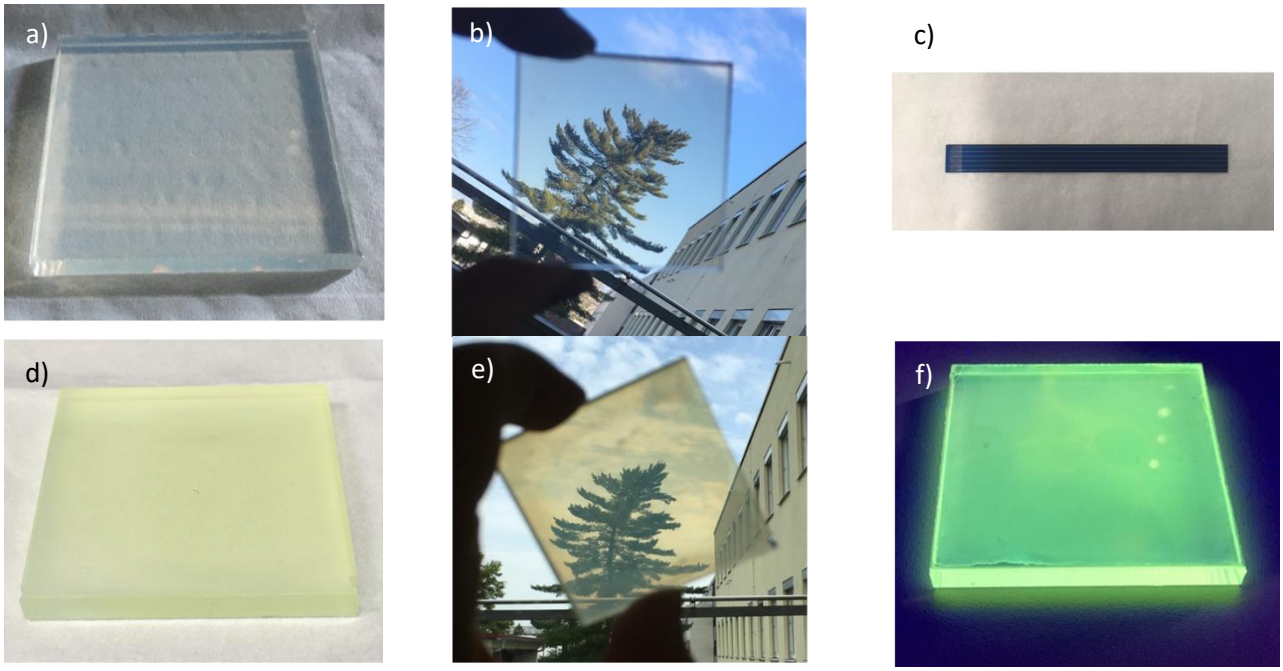

Figure 5.6: Panel a) borosilicate glass sprayed with the ZnBDC SURMOF. Panel b) borosilicate glass sprayed with the ZnBDC SURMOF in transparency. Panel c) silicon solar cell strip used in the LSC device. Panel d) glass slab coated with ZnBDC and loaded with AIE dyes. Panel e) glass slab coated with ZnBDC and loaded with AIE dyes in transparency, the loaded sample looks opaque after the dye loading with respect to the one before the loading in panel b). Panel f) glass slab coated with ZnBDC loaded with AIE dyes under UV illumination (365 nm).

5.2.1 Optical characterization

The dyes density in the sample is increased by successive drop-casting of dye solution. As reported in the fourth chapter, increasing the dye concentration, a higher i-PLQY and e-PLQY, are found with a consequent overall higher absorption and red-shift of absorbance. PLQY is even more critical in the LSC due to the phenomenon of re-absorption, where the light emitted by a molecule can be absorbed again by another one, undergoing further emission [78]. The red-shifting of absorbance brings a positive impact on the LSC when the device is exposed to the solar radiation, since the absorption peak of the sample is shifted towards the emission peak of the sun. The amounts of dye solution drop-casted are 0.8, 2.4, 5.6, 8.0, 11.8, 16.8, 22.0 and 24.8 ml. Figure 5.7 shows how the sample aspect changes depending on the amount of solution drop-casted, with increasing luminescent properties and a change in the emission color. After 24.8 mL, no more solution is drop-casted on the sample because, as shown in Figure 5.7 h, small portions of the sample are peeling off from the surface. The silicon solar cell is attached on the top edge of the sample. The bi-component glue absorbed a little portion of the dye as well, showing some characteristic luminescence.

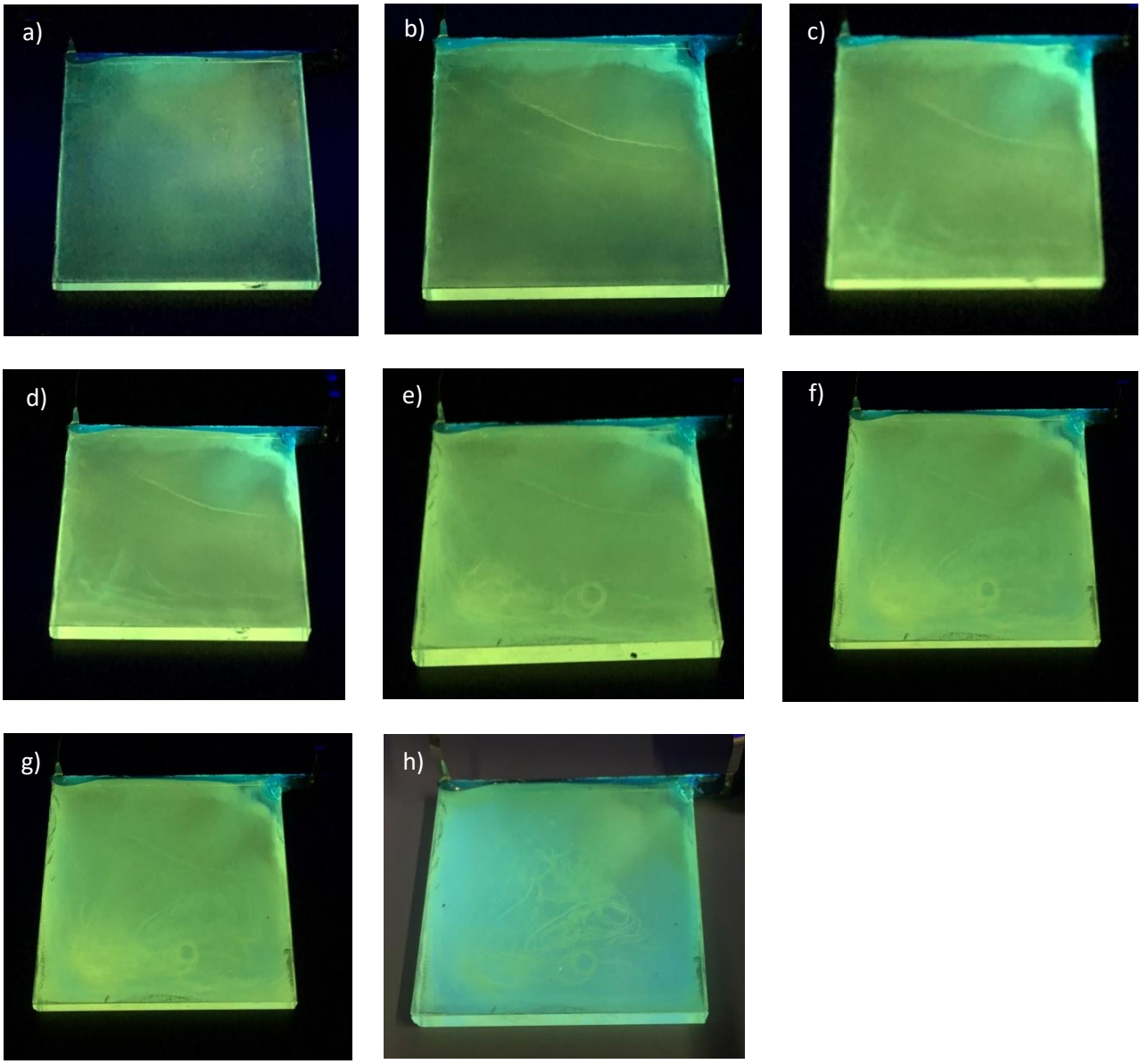

Figure 5.7: panel a) to h) SURMOF deposited on borosilicate glass drop-casted respectively with 0.8, 2.4, 5.6, 8.0, 11.8, 16.8, 22.0 and 24.8 ml under UV illumination. The sample changes the intensity and color of the emitted light with Increasing the amount of drop-casted solution.

Figure 5.7 also shows how the loading in the samples is inhomogeneous, having spots with different concentrations highlighted by different colors. This behavior is caused by the dimension of the sample, 25 cm^2 compared with ~ 4 cm^2 of the samples in the fourth chapter. During the drying step of the loading process, the dye solution tends to stain in some spots due to its surface tension and consequentially parts with different concentration are found.

Comparing the shape and the position of the peaks of the absorbance spectra of the samples, shown in figure 5.8, with the absorbance spectra of the samples loaded with AIE dye (reported in Figure 4.9, fourth chapter) a rough estimation of the dye density in the LSC samples can be obtained.

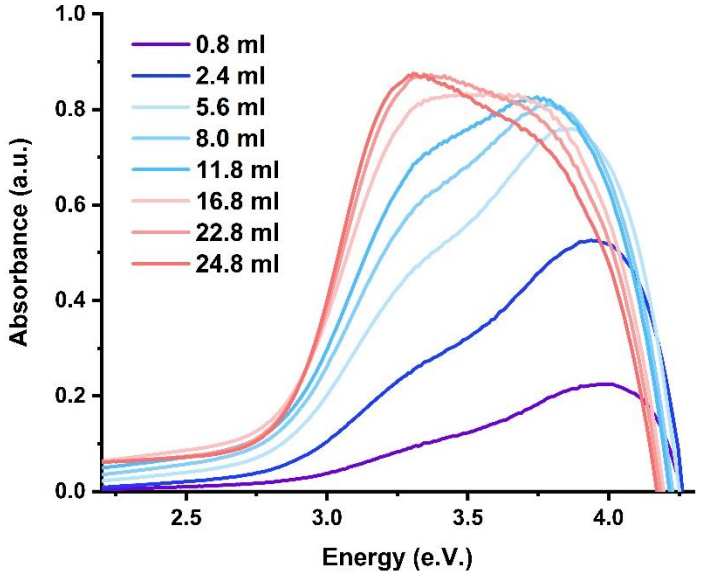

Figure 5.8: absorbance spectra of the LSC drop-casted with an increasing amount of solution. Increasing the drop-casted solution increases the absorbance and red-shifts the spectra.

The relation between the drop-casted solution and dye density can be established for 5.6, 8.0, 11.8, 16.8, 22.8 and 24.8 mL, while for 0.8 and 2.4 mL, the absorbance spectra are not comparable with the one recorded in the previous chapter.

Table 5.1: dye density related to the amount of drop-casted solution on top of the SURMOF.

Drop-casted solution (mL)	Dye density (mmole/cm^3)
5.6	0.2
8.0	0.3
11.8	0.5
16.8	1.0
22.8	1.8
24.8	2.6

5.2.1 Device characterization

For all the measurements, the edges of the LSC not covered by the solar cell are blackened with black tape and as well the part of the solar cell that is not fitting with the LSC edge to avoid contamination from other light sources.

In order to characterize the system LSC with a solar cell, the I-V curve of the solar cell attached to the LSC has been measured using an Oerlkon SUS V2.0 sun simulator [79], which mimics the light from the sun, providing a constant irradiance of 1000 W/m^2 on 9x9 cm^2. The light is generated by two lamps, a Xenon lamp for the UV region of the spectrum and a Halogen lamp for the visible and infra-red region. The spectrum of the light generated by the sun simulator is the one for Air Mass 1.5 global (AM 1.5 G) that is the light passing through the atmosphere at 48° from the vertical (Zenith angle) that is a good approximation of the light spectrum at the Germany latitude. The sun simulator spectrum is reported in Figure A.6 in the appendix. The I-V curves are recorded with a Keithley 2400 source meter. Figure 5.9 shows the I-V curve of the samples obtained at different dye concentrations. For all the curves, open-circuit voltage (V_{OC}) can be defined as the voltage at zero current, short circuit current (I_{SC}) as the current at zero voltage and the maximum power (P_{MAX}) as the product of the maximum voltage and the maximum current. The I-V curves increase both in I_{SC} and P_{MAX} with the increasing dye density, demonstrating that a higher flux of light reaches the solar cell. From these measurements, , the light has been found to reach the solar cell even in the case of the empty SURMOF, probably due to the light scattered by the SURMOF itself.

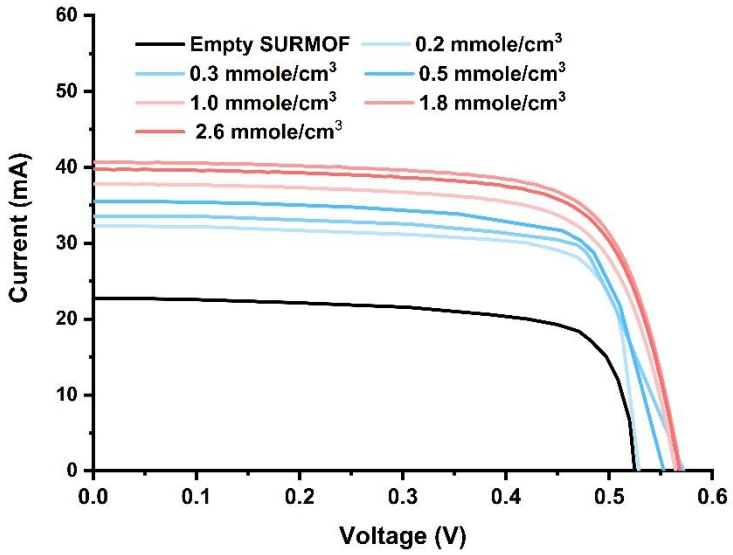

Figure 5.9: I-V curve of the sample Vs the dye concentration. In black, the I-V curve of the sample (glass + SURMOF) without any loading. Increasing the dye concentration, an increase in V_{oc}, I_{sc} and P_{MAX} is observed, until reaching a saturation for the highest concentrations.

The efficiencies (η) of the samples have been calculated with the ratio between the power out (P_{out}) from the system and the power introduced in the system (P_{in}).

$$\eta = \frac{P_{out}}{P_{in}}, \tag{5.1}$$

Defining P_{out} as the maximum power coming out form the solar cell.

$$P_{out} = P_{\max solar\ cell}, \tag{5.2}$$

And P_{in} as the power of the light hitting the surface of the LSC obtained as the product of the irradiance (Ir), provided by the sun simulator, and the area of the LSC (A_{LSC}).

$$P_{in} = Ir \cdot A_{LSC}. \tag{5.3}$$

The calculated efficiencies are related to only one solar cell attached. Assuming the same behavior for all the four edges, from the moment that the other edges have been blackened. Then the efficiency with four solar cells can be obtained multiplying the single efficiency of a cell by four.

Table 5.2: device efficiencies, for one and four solar cells, related to the dye density

Dye density (mmole/cm^3)	Device efficiency one cell	Device efficiency four cells
0.2	0.5%	2.1%
0.3	0.6%	2.2%
0.5	0.6%	2.3%
1.0	0.6%	2.4%
1.8	0.7%	2.7%
2.6	0.6%	2.6%

The device efficiencies with one solar cells are a fourth of the efficiency of a bulk LSC device with similar dimension and monocrystalline silicon solar cells but made by Lumogen red 305 dye made by Desmet *et al*.[80].

A further efficiency related only to the LSC, is the optical efficiency, with two possible definitions. The external optical efficiency ($\eta_{ext.opt.}$) defined as the ratio between the power coming out from the LSC edges and the power hitting the surface of the LSC and the internal optical efficiency ($\eta_{int.opt.}$) defined as the ratio between the power coming out from the LSC edges (P_{edges}) and the power absorbed by the LSC ($P_{abs.}$).

$$\eta_{int.opt.} = \frac{P_{edges}}{P_{abs.}} \quad \eta_{ext.opt.} = \frac{P_{edges}}{P_{LSC\,surf.}}. \tag{5.4}$$

These internal and external optical efficiencies are calculated only for the sample with highest concentration and not for all the samples. In order to calculate the photocurrent coming out from the edge of the LSC, the solar cell can be used as a detector using the definition of the EQE:

$$EQE(\lambda) = \frac{I_{ph}\,(\lambda)}{q\phi_{ph,\lambda}}, \tag{5.5}$$

With $I_{ph}\,(\lambda)$ the photocurrent generated by the solar cell, $\phi_{ph,\lambda}$ the photon flux on the solar cell and q the elementary charge. For short-circuit current condition, Equation 5.5 can be written:

$$I_{SC} = q \int \phi_{ph,\lambda} EQE\,(\lambda)\; d\lambda. \tag{5.6}$$

For the LSC, the photon flux can be expressed as the normalization of the emission spectrum of the sample ($\phi_{Nor.Em.\lambda}$) multiplied by a factor K.

$$I_{SC} = q\,K \int \phi_{Nor.Em.\lambda}\, EQE\,(\lambda)\; d\lambda, \tag{5.7}$$

Considering the sample with the highest concentration (2.6 mmole/cm^3). I_{SC} can be found from the I-V curve of the sample and in particular for this calculation has been used the difference between the I_{SC} of the I-V of the sample and the I_{SC} of the empty SURMOF. I_{SC} of the empty SURMOF gives a contribution to the I_{SC} but it is not due to the dye loading.

$$K = \frac{I_{SC}}{q \int \phi_{Nor.Em.\lambda}\, EQE\ (\lambda)\, d\lambda'}, \tag{5.8}$$

The proportionality constant *K* then can be used in the Equation 5.9 to obtain the total photocurrent that hits the solar cell.

$$I_{ph.edge} = qK \int \phi_{Nor.Em.\lambda}\ (\lambda)\ d\lambda = 20.1\ mA \tag{5.9}$$

To calculate the $\eta_{int.opt.}$ the AM_G 1.5 spectrum provided by the sun simulator has to be weighted with the absorption spectrum of the AIE dye loaded in the sample to obtain the photocurrent absorbed by the dye molecules.

$$I_{abs.} = A_{LSC}\, q \int AM_G 1.5\ (\lambda) A(\lambda) \frac{\lambda}{hc} d\lambda = 75.0\ mA. \tag{5.10}$$

The term $q\frac{\lambda}{hc}$ is needed to change the unit of measurement from W/m^2 to A/m^2 in order to be consistent with the other data for calculating efficiency. A_{LSC} is the area of the LSC.

The photocurrent at the edge multiplied by four is much larger than the photocurrent absorbed by the LSC. For this reason, there should be another contribution to the photocurrent edge, which is not coming from the dye molecule. To have a better understanding of this phenomenon, the emission from the edge of the sample is compared with the one of the dye.

.

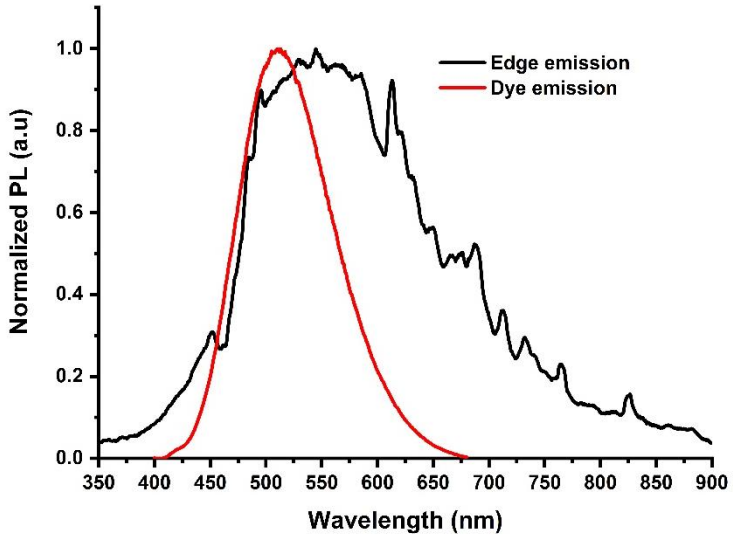

Figure 5.10: comparison between the normalized emission from the AIE dye loaded in the SURMOF at the highest concentration and the emission obtained from the edge of the LSC. The emission from the edge is clearly different from the dye emission indicating an additional contribution a part from the emission from the dye.

Figure 5.10 shows the comparison between the dye and edge emissions. The shape of the two spectra is different, which is a clear sign of different contributions to the edge emission rather than only from the dye. A possible reason for this difference is the light scattering from loaded SURMOF. Figure 5.9 shows that even in the empty SURMOF, the scattered light reaches the solar cell and then produces an output power. It can be hypothesized that the light scattered increases with the dye concentration in the LSC. In order to distinguish the two possible contributions of the scattered light and the dye, the sample at the highest concentration of dye? has been placed under a sun simulator with a long pass filter RG630, between the light source and the sample, recording. The RG630 filter cuts ideally all the wavelengths below 630 nm, allowing to pass the other wavelengths (see transmission spectrum Figure A.7 in the appendix). For this measurement, the collected photocurrent has been related to the scattering, since all the useful light that can be absorbed by the dye is cut off. Using the formula from Equation 5.5, modified with AMG1.5 of the sun simulator instead of the photon flux of the dye and adding the transmission of the filter.

$$I_{SC\ Red} = q\ K_{red} \int AM_G 1.5_{Nor.\lambda}\, T(\lambda) EQE\ (\lambda)\ d\lambda, \tag{5.11}$$

From Equation 5.11 K_{red} can be obtained

$$K_{red} = \frac{I_{SC\ Red}}{q \int AM_G 1.5_{Nor.\lambda}\, T(\lambda) EQE\ (\lambda)\ d\lambda} = \frac{1}{q} 0.077. \tag{5.12}$$

Assuming a constant scattering for all the wavelengths, the K_{red} can be used to calculate photocurrent related to the scattering

$$I_{scat} = q\ K_{red} \int AM_G 1.5_{Nor.\lambda}\, EQE\ (\lambda)\ d\lambda = 35.7\ mA, \tag{5.13}$$

From the difference between the I_{SC} measured in the I-V curve (Figure 5.9) and the I_{scat} scattering the photocurrent related only to the dye I_{Dye} can be obtained.

$$I_{Dye} = I_{SC} - I_{scat} = 39.7 - 35.7 = 4.0\ mA. \tag{5.14}$$

As a consequence, the internal optical efficiency is calculated as the ratio between the calculated dye contribution to the photocurrent and the absorbed photocurrent calculated in Equation 5.10

$$\eta_{int.opt.} = \frac{4\ I_{Dye}}{I_{abs.}} = 21\% \tag{5.15}$$

The calculation of internal optical efficiency is essential to understand the different factors that contribute to edge emission of the LSC. SURMOF based LSC works in a different way with respect to the standard LSC combining the total internal reflection of dye emission with the light scattered, as shown in Figure 5.11.

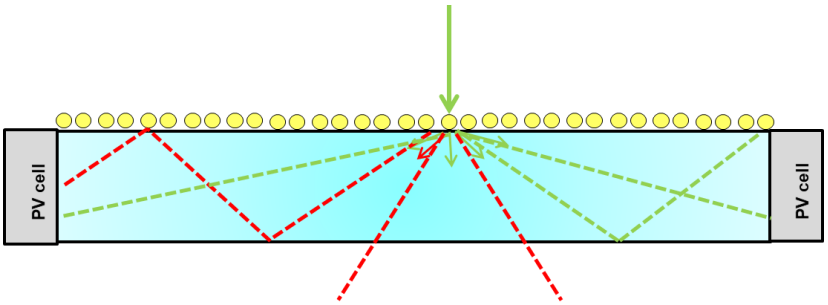

Figure 5.11: schematic representation of the SURMOF based LSC working principle. The two contributions of the edges emission are the light from the dye emission total internal reflected (in red) and the light scattered by the loaded SURMOF (in green).

For external optical efficiency instead of the photocurrent absorbed by the dye the photocurrent that hits the LSC surface has been used.

$$I_{LSC\ surf.} = A_{LSC}\, q \int AM_G 1.5\ (\lambda) \frac{\lambda}{hc} d\lambda = 1.7\ A \tag{5.16}$$

Then the external optical efficiency is:

$$\eta_{ext.opt.} = \frac{4 I_{dye}}{I_{LSC\ surf.}} = 0.9\% \tag{5.17}$$

The external optical efficiency of the SURMOF-based LSC is 0.9 % that is lower with respect to the external optical efficiency of LSC with the same dimension and monocrystalline solar cell but built using the Lumogen Red 305. The LSC sample made with Lumogen Red 305 has an external optical efficiency of 14.2% [80]. This difference is mainly due to the different PLQYs of the AIE dye and Lumogen Red. Another factor that differentiates the two dyes is the absorption region; the Lumogen Red absorption is broader and peaked in a region where the sun sends a higher number of photons. A different factor that has a negative influence on the external optical efficiency is the scattering, which increases the overall efficiency of the system, but is a disadvantage for the total internal reflection, since it couples out the light from the transparent slabs.

Summary

The fifth chapter has shown two possible optical applications for the AIE loaded SURMOF. The first application is in the LED/display field, using the loaded SURMOF as a down-converting layer. The SURMOF can be easily deposited on different shapes of the substrate, and the dyes can be loaded to form different patterns. Among the three possible approaches to pattern AIE dye inside the SURMOF, the best method is inkjet-printing, being able to print precise patterns on the SURMOF substrate and down to 70 µm features. The second application is in the field of luminescent solar concentrator, where, following the design of the thin-film LSC, the AIE loaded SURMOF is deposited on a glass slab with a solar cell attached on one edge. The device shows an overall efficiency lower with respect to a standard LSC made by Lumogen red 305 with the same dimension and an equivalent solar cell attached. The investigation of the internal optical efficiency provides a deeper understanding of the working mechanisms in the SURMOF-based LSC, where

the emission from the edges is a combination of emitted light by the AIE dye and scattered light from the loaded SURMOF film.

Contributions to the chapter

Nicolò Baroni (Author):

- Synthesis, structure and optical characterization of ZnBDC SURMOF and of the AIE@SURMOF samples
- Ideas for dye patterning on the SURMOF
- Production and characterization of LSC samples
- Design of the figures and main text

Stefan Schliβke and Gerardo Hernandez-Sosa:

- Introduction to inkjet-printing technique and production of the inkjet-printed samples.

Dmitry Busko and Michael Adams:

- Discussion on optical characterization

Andrey Turshatov and Bryce S. Richards:

- Discussion of the results

Ian A. Howard:

- Development of dye loading technique and discussion of the results

Chapter 6: Room temperature phosphorescence MOFs

In this chapter, the preliminary characterization of two room-temperature phosphorescence (RTP) MOFs is shown. The first RTP MOF considered is Zn-IPA, previously reported by Yang *et al. [59] and synthesized with a microwave-assisted method. XRD measurement shows that the obtained Zn-IPA MOF has the same structure as the one in literature. RTP is detected in this MOF with the same emission peak but shorter lifetime. Zn-IPA is then used as a loading site for an Iridium complex with two methods: the first one with the addition of the Iridium compound during MOF synthesis, while the second one with the immersion of the MOF in a dye solution. Based on absorbance measurements, the loading is unsuccessful for both techniques. Zn-DTA is a novel MOF designed to have red-shifted phosphorescence with respect to Zn-IPA introducing two sulfur atoms in the coordination groups of the linker molecule. The preliminary test shows a crystal structure comparable with the one of other RTP MOF and a phosphorescent emission around 580 nm with an average lifetime of 5.93 ms.*

Organic materials that exhibit RTP phenomenon, described in the first chapter of this work, have been investigated in different fields of research as organic light-emitting diode (OLED) [81], sensor [82] and photosensitizer [83]. Organic RTP materials have been studied for the ease in processing and their flexibility in deposition and fabrication that make them good candidates for a device application.

Furthermore, their RTP efficiencies highly depend on the crystalline state of the organic molecules as shown by Yuan *et al.* [84] and for this reason, MOFs have been investigated as an efficient system for RTP due to their intrinsic coordination of the chromophore used as an organic linker. MOF structure reduces the flexibility of the organic linker conformation, leading to a reduction in the molecular motion and vibration that, act as non-radiative deactivation channels for the triplet excitation. Another factor that could influence the RTP in MOF is the presence of the metal ion that can act as a heavy atom and increase the efficiency of the spin-orbit coupling [59]. MOF metal ion and in particular Zn^{2+} , as reported by *Liu et al.,* can also acts as an antenna with a metal to ligand energy transfer [85].

6.1 Zn-IPA

Zn-IPA MOF is composed of zinc as metal ion and isophtalic acid (IPA) as the organic linker. In this work, Zn-IPA is synthesized following the quantity of reactants described by Yang *et al* [59] but using microwave-assisted synthesis as described in the second chapter. Residual trace of synthesis solvent in MOF pores could change the material and optical properties of the sample. Water, used as a solvent in the reaction, is difficult to remove from MOF pores due to its high boiling point. For this reason, MOF powder is washed with acetone in order to substitute the residual water in the pores. Acetone is more volatile than water and then is easier to remove. MOF powder is then activated using rotavapor, for removing the residual acetone.

6.1.1 Zn-IPA characterization

The obtained Zn-IPA crystal is reported in Figure 6.1 b, and characterized via XRD shown in Figure 6.1 c.

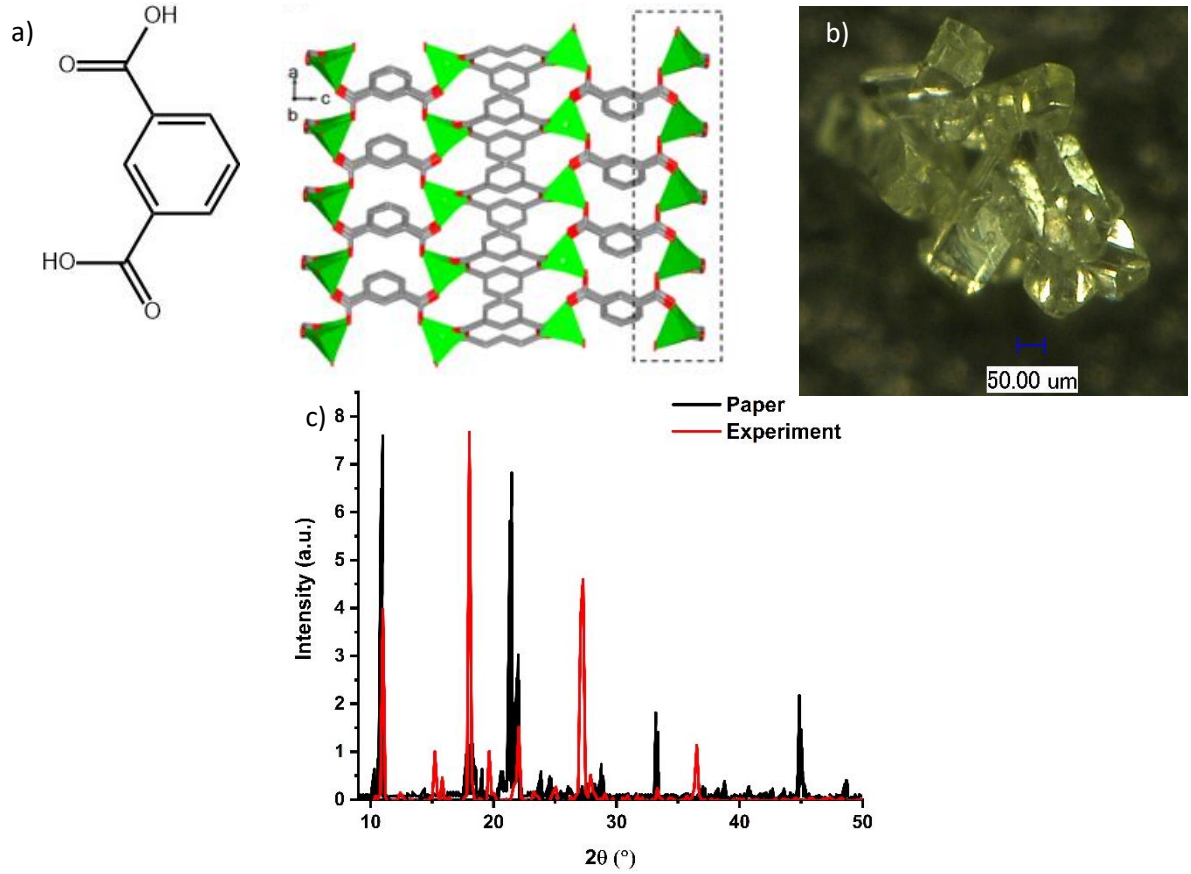

Figure 6.1: panel a) IPA molecular structure and Zn-IPA MOF crystal structure, in green the zinc metal ion, structure reproduced with permission from [59]. Panel b) Zn-IPA crystal, synthetized via microwave-assisted method, magnified under optical microscope. Panel c) comparison between XRD of Zn-IPA MOF synthetized and the one reported in the work of Yang *et al.* [59]. The peaks position are comparable between the two spectra and the two MOFs synthetized with different methods have a similar crystal structure.

The comparison between the XRD spectrum of the synthetized Zn-IPA with the one of the MOF reported by Yang *et al.* is reported in Figure 6.1 c. The peak positions are in good agreement confirming that the Zn-IPA

MOF synthetized has the same structure of the one described in literature. Zn-IPA has a tetragonal system with space group $P4_12_12$ [59]. A comparable behavior can be appreciated in the optical properties as well. Under UV illumination (365 nm) the MOF powder is characterized by a blueish emission, as shown in Figure 6.2 a; when the light is switched off, only the contribution of phosphorescence persists with a greenish emission. In Figure 6.2 from b to f the phosphorescence of the sample at different time intervals from 1 second to 7 seconds is reported.

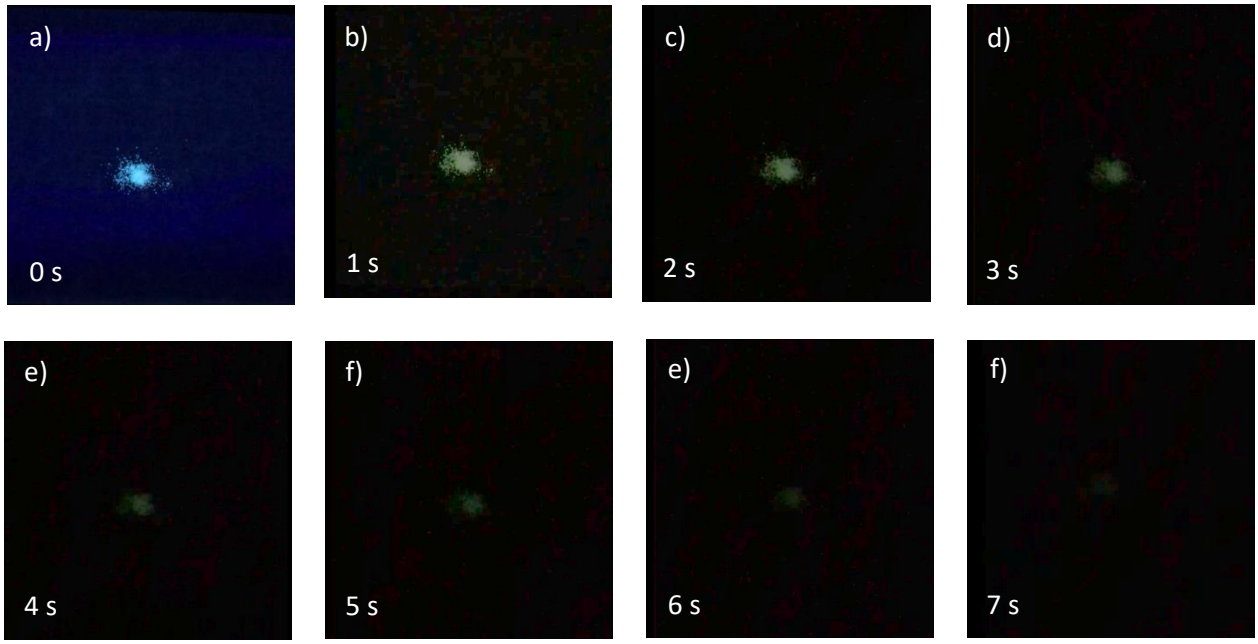

Figure 6.2: panels from a) to f) RTP of Zn-IPA MOF at different time intervals. Panel a) is identified as zero time before the UV illumination (365 nm) is turned off. A weak phosphorescence of the sample can be appreciated even after 7 second of the light turning-off. Photographs in panels from b) to f) have enhanced contrast to highlight the behavior of Zn-IPA phosphorescence.

The two components of the emission spectrum of the Zn-IPA MOF are studied in detail via the Cary eclipse spectrophotometer. In Figure 6.3, the fluorescence and phosphorescence spectra of the synthesized Zn-IPA is shown. Comparing the two components of emission spectrum of the synthesized Zn-IPA with the one reported, the phosphorescence of the synthesized sample is in agreement with the one reported with a peak around 487 nm, while the fluorescence peak of the sample, at 431 nm, is red-shifted with respect to the one in literature, at 387 nm. The lifetime of the Zn-IPA emission is measured in dynamic vacuum and it is shorter with respect to the one synthetized in the literature $\tau = 1321$ ms. The kinetic of the phosphorescence can be fitted with a mono-exponential decay; the lifetime of the phosphorescence emission (487 nm) is 366 ms. A possible reason for the reduction in lifetime is constituted by residual of solvent molecules present in the MOF pores, which quenches the phosphorescence and reduces its lifetime.

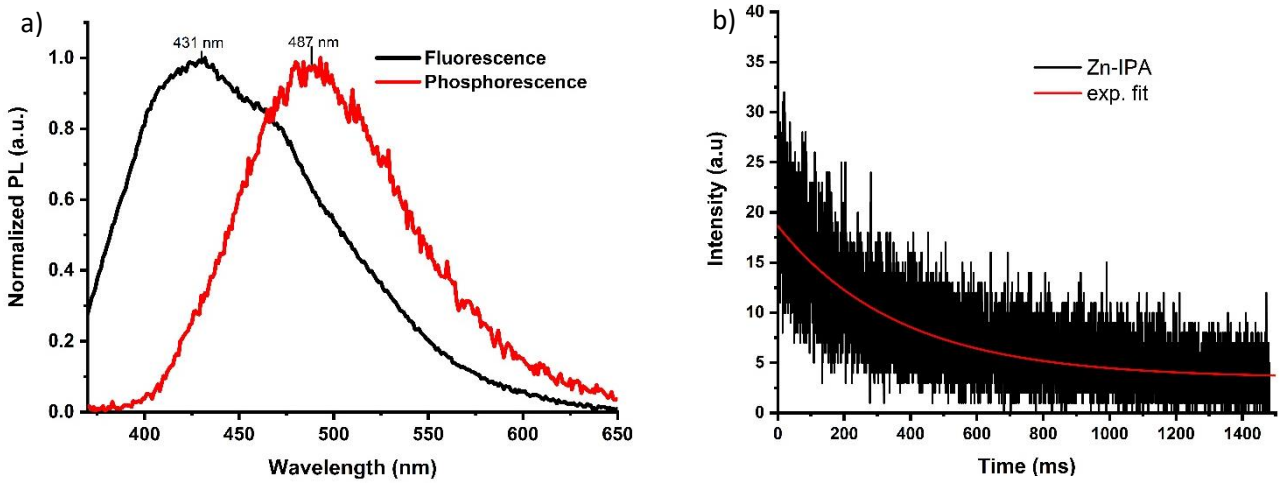

Figure 6.3: panel a) fluorescence (in black) and phosphorescence (in red) of the Zn-IPA measured with Cary Eclipse spectrometer, excitation 350 nm. Panel b) lifetime kinetic of Zn-IPA, the curve can be fitted with a monoexponential decay with a lifetime of 366 ms.

6.1.2 Iridium complex loading in Zn-IPA

Zn-IPA is then used as scaffold to incorporate guest molecule. The chosen guest molecule is (2-carboxypyridyl)bis(3,5-difluoro-2-(2-pyridyl)phenyl)iridium(III) (FIrpic) an Iridium complex that was already used as guest molecule loaded in the MOF [44]. FIrpic is part of a family of Iridium complex that with their emission properties covers a wide range of wavelength [86]. The purpose of the loading complex mentioned above is obtaining energy transfer between MOF and the loaded molecule to change the emission of the overall system. In case of positive results, the system could be extended to other Iridium complex. Two processes of loading have been investigated. The first one consists of a long soaking process of the MOF powder in FIrpic solution (1 mM in ethanol) at 60°C for 24 hours as already reported in [70]. The second process consists in adding the FIrpic during the MOF synthesis. The loading processes do not change the XRD of the MOF, as shown in Figure 6.4, the peaks position in XRD are maintained.

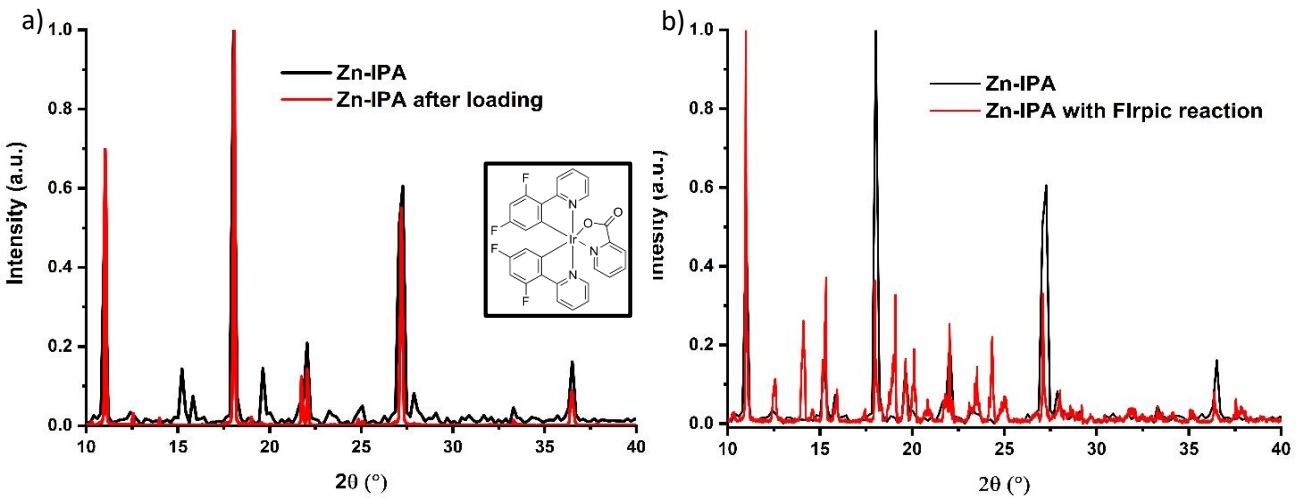

Figure 6.4: panel a) comparison between the Zn-IPA XRD before and after the loading of FIrpic via solution. Panel b) comparison between XRD of Zn-IPA synthesized with and without the presence of FIrpic during the synthesis process. For both methods, the peak position XRDs do not change when the FIrpic is added. Inset the molecular structure of FIrpic molecule.

Measurements of absorbance are performed on the samples and compared with the characteristic absorbance of the iridium compound, to establish the success of the loading processes. In order to measure the absorbance of the MOFs, the MOF powders are immobilized between two quartz glass plates.

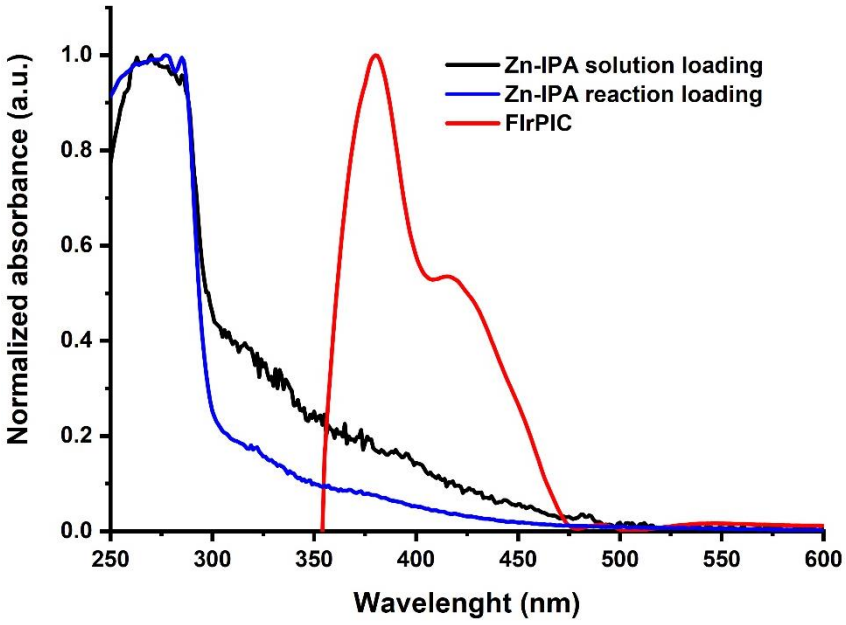

Figure 6.5: normalized absorbance spectra of the Zn-IPA loaded with FIrpic complex using solution loading in black, and reaction loading, in blue. In red the absorbance of the FIrpic is reported. In the absorbance of the two Zn-IPA, no trace of the absorbance of FIrpic is found.

Figure 6.5 shows that there is no trace of the characteristic absorbance of FIrpic complex in the loaded MOF samples. This result is the first proof that the compound molecules are loaded in an undetectable amount or are not loaded in the MOF pores.

6.2 Zn-DTA

Following the example of the RTP Zn-BDC MOF shown by Yang *et al.* [59], n-DTA MOF has been synthesized adopting the procedure described in the second chapter. Zn-IPA is composed by zinc as the metal ion and dithioterephthalic acid (DTA) as the organic linker. DTA has a similar molecular structure of BDC, however CSOH substitute COOH as one of coordination groups of the molecule and where a sulfur atom substitutes an oxygen atom, as shown in Figure 6.6 a and b. The purpose of using a DTA linker in the MOF structure is to maintain the same structure of the Zn-BDC MOF and ensuring the RTP properties to the MOF and red-shifting the emission. The emission red-shifting is due to the presence of the sulfur atom. The substitution of oxygen with the sulfur changes the length of the bond. The carbon-sulfur bond (C-S) is longer than the carbon-oxygen bond (C-O) and leads to a different framework configuration reducing the energy that molecule can release [87]. Zn-DTA is activated, with the same process used for the Zn-IPA, using acetone to substitute the water and then rotary vapor to remove the acetone. Emission from the Zn-DTA sample can be already appreciated under UV illumination (365 nm), where the sample emits a reddish light, as shown in Figure 6.6 c.

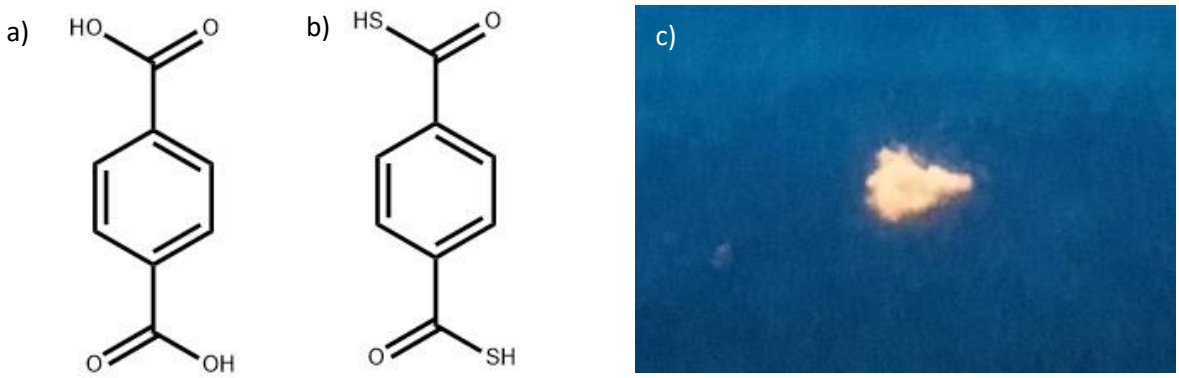

Figure 6.6: panel a) molecular structure BDC linker. Panel b) molecular structure of DTA linker. Panel c) Zn-DTA MOF powder under UV illumination (365 nm).

XRD measurement is performed on Zn-DTA crystal and compared with the XRD diffractogram of Zn-BDC MOF, as shown in Figure 6.7. Zn-DTA XRD is in partial agreement with the Zn-BDC XRD. In XRD, the angles related to a peak depend on the distance of molecular planes. A possible reason for the differences between the two XRD spectra is the different length of the coordination group COSH and COOH, which brings to different angles in XRD pattern.

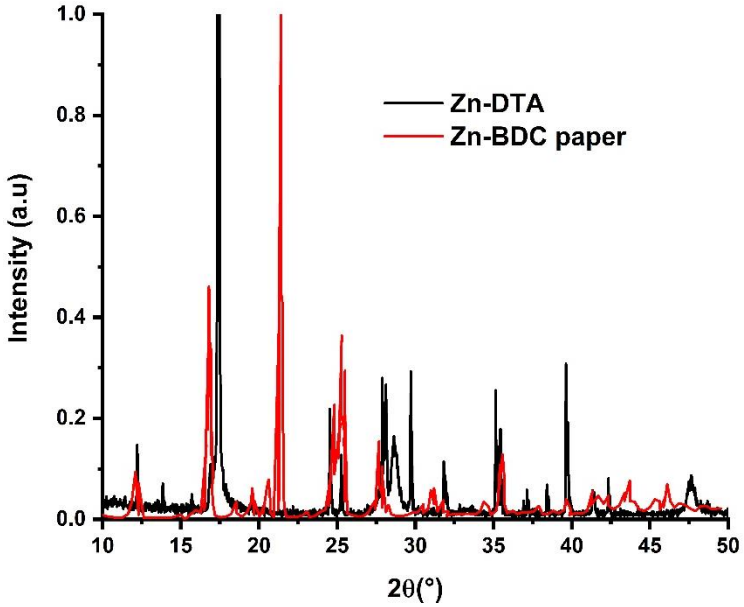

Figure 6.7: comparison between the XRD of Zn-DTA MOF and XRD of Zn-BDC MOF [59]. Zn-DTA XRD is in partial agreement with the Zn-BDC XRD. The difference arises from the different length of the linker.

Optical characterization is performed on Zn-DTA to understand the nature of its emission. The emission of the Zn-DTA has two components: fluorescence and phosphorescence, as shown in Figure 6.8 a. Fluorescence emission is characterized by a peak around 355 nm, while for phosphorescence is around 580 nm. Both components are red-shifted with respect to the reported fluorescence and phosphorescence peaks of Zn-BDC, which are 330 nm and between 482 nm and 508 nm respectively [59]. Further investigation on phosphorescence lifetime (in vacuum) shows how the kinetic of Zn-DTA can be approximated by a bi-exponential decay with τ_1 =1.58 ms and $\tau_2 = 14.13$ ms and a consequential average lifetime $\tau_{av} = (\alpha_1\tau_1^2 + \alpha_2\tau_2^2)/(\alpha_1\tau_1 + \alpha_2\tau_2) = 5.93$ ms.

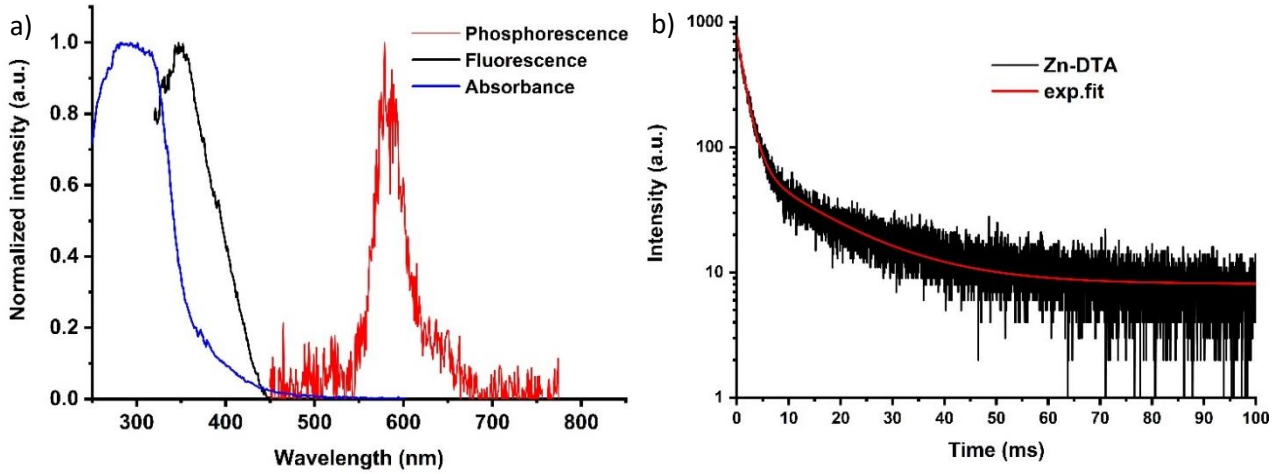

Figure 6.8: panel a) absorbance (blue), fluorescence (black) and phosphorescence (red) of Zn-DTA MOF. Panel b) kinetic of phosphorescence emission (580 nm), in black, bi-exponential decay fit, in red. The two components of the bi-exponential decay are τ_1 =1.58 ms and $\tau_2 = 14.13$ ms.

Summary

This chapter showed the material and optical characterization of the Zn-IPA MOF and Zn-DTA MOF. Zn-IPA is synthesized via a microwave-assisted method showing the same crystal structure of Zn-IPA synthesized via the hydrothermal method. The optical properties of the synthesized Zn-IPA are in partial agreement with the one described in the literature. Zn-IPA shows both fluorescence and phosphorescence emission. While the phosphorescence spectrum matches with the literature, its lifetime is shorter and equals to 366 ms, compared to 1321 ms reported by *Yang et al.* [59]. On the other hand, fluorescence is red-shifted with respect to the Zn-IPA synthesized via hydrothermal method. Zn-IPA MOF is then used as a host material for the iridium complex in order to obtain energy transfer between the MOF and the guest molecule. The attempts of molecule loading are performed in two ways: by introducing the iridium complex during the MOF reaction and via solution loading, immerging the MOF powder in a dye solution. Both methods gave negative results in terms of absorbance measurements, with no sign of iridium complex absorbance in the absorbance of the loaded MOFs.

Zn-DTA MOF is a brand new MOF synthesized by the microwave-assisted method, showing an XRD pattern in partial agreement with respect to the Zn-BDC MOF. The main reason for this discrepancy between the two XRDs is the presence of two sulfur atoms in the coordination group of the organic linker (CSOH), where the C-S bond is longer than the C-O bond. This characteristic also affects the emission of the MOF with a fluorescence peak around 350 nm and a phosphorescence peak around 580 nm, showing general red-shifting with respect to the emission of Zn-BDC and an average lifetime of its emission equals to 5.93 ms. This is the first MOF reported with a red RTP emission.

For both MOFs, these are only preliminary results. MOF synthesis via the microwave-assisted method needs to be studied in detail to obtain the optimal parameters in terms of reaction yield, crystal quality and, for Zn-IPA, to achieve the same optical properties of the MOF in the literature. For Zn-IPA another loading technique that has to be tested is the loading via gas-phase, already shown by Müller *et al.* [44] for iridium complex. This technique was not possible to perform in this work, but it gave positive results for the iridium complex loaded in UMCM-1 MOF. Regarding Zn-DTA, single crystal XRD has to be performed to resolve its exact structure and additional optical characterization will elucidate how the excitation travels in the MOF i.e., from metal to linker. This can be achieved measuring the lifetime of the MOF depending on the difference fluences of the excitation source. It can be measured how the phosphorescence changes depending on the metal center in order to understand the contribution of the metal center to the overall emission.

Contribution to the chapter

Nicolò Baroni (Author):

- Synthesis, structure and optical characterization of Zn-IPA and Zn-DTA MOFs
- Design of the experiment
- Design of the figures and main text

Andrey Turshatov and Ian A. Howard:

- Design of the experiments
- Discussion of the results

Bryce S. Richards:

- discussion of the results

Chapter 7: Conclusion and Outlook

7.1 Conclusion

This PhD thesis showed how molecules with carboxylic pendant groups and planar molecular structure could be infiltrated in the SURMOF 2 structure. Equivalent molecules without carboxylic groups do not infiltrate into the SURMOF. The drop-casting method allows organic molecules to be loaded directly from ethanolic solution in a straightforward and fast fashion and does not require any activation step as in the previous methods [53]. The confirmation that the dyes are loaded through all the sample depth, and not only attached on the surface, is provided by time-of-flight secondary ion mass spectroscopy. ToF-SIMS provides a depth profile of the composition of the sample, showing the presence of dye in the different portions of the sample.

Metallated porphyrins have been chosen as first candidates, since they are optically active dyes that confer novel optical properties to the SURMOF via guest molecule loading. Once loaded in the SURMOF structure, metallated porphyrins show strong signs of aggregation, characterized by broadening and shifting in the absorption and emission spectra, and a strong quenching in the emission lifetime.

In order to use the disadvantage of aggregation as an advantage for making SURMOF samples with emissive properties, the H_4ETTC dye has been intercalated between SURMOF sheets. H_4ETTC is a dye from the family of aggregation-induced emission dye that fulfills all the requirements to be loaded in the SURMOF 2 structure. Once loaded inside the SURMOF scaffold, H_4ETTC is optically active with a strong emission and high i-PLQY even at low concentrations. Increasing the dye concentration inside the SURMOF substrate leads to an increase of internal and external PLQY. The highest dye density that has been loaded inside a 150 nm SURMOF film is 2.6 mmole/cm^3. Further optical characterization showed that SURMOF plays an essential role in the emission properties of the loaded AIE chromophore. SURMOF has a double role: acting as a substrate for the loading and immobilize the dye blocking the non-radiative channel of the AIE dye.

AIE loaded SURMOF has been used for two optical applications. The first is the use of AIE dye as ink to print different patterns inside the SURMOF. This is a proof of principle that the SURMOF can be used as a good ‘ink-receiving layer’ to allow wavelength shifting AIE dyes to be printed. This could be exploited in for printing luminescent security markers, or potentially for a patterned color-shifting layer in display-like devices. The three printing methods investigated in this thesis are the drop-casting mask, the SURMOF spraying mask, and the inkjet-printing method. Among these, the inkjet-printing method is the one that provides the best results, allowing to design different patterns on the SURMOF and to print features with a size down to 70 µm. The size of the printed AIE features are comparable with respect to LED of a pixel in standard LCD monitor, as shown in Figure 7.1.

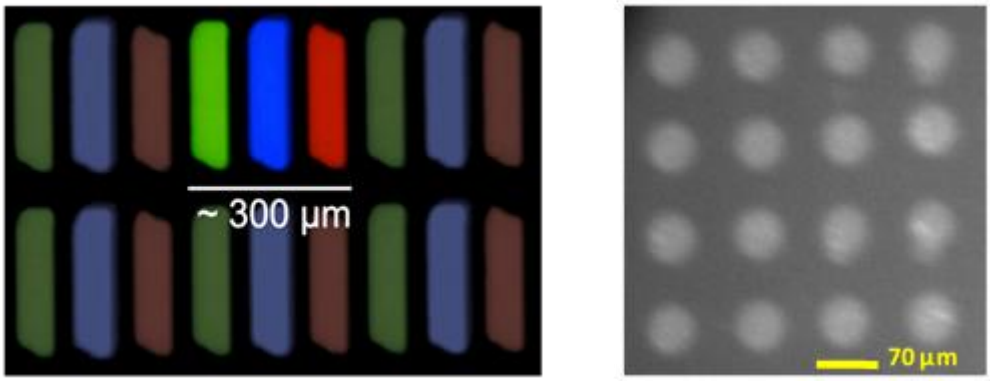

Figure 7.1: comparison between a pixel of 300 µm composed by three LED (green, blue and red) and the dots of 70 µm produced with the AIE ink-jet printed features. LED picture taken from [88].

The second application for AIE-loaded SURMOF is a thin-film LSC. The produced system (LSC + solar cells) show a lower efficiency compared to the standard bulk LSC. However, the study on internal and external optical efficiency shows a significant contribution to the edges emission derives from the light scattered by the loaded SURMOF. The scattering, in this case, has a positive effect on the LSC efficiency on the small scale, whereas for a larger sample, it could have a negative effect on the LSC, destroying the total internal reflection and decreasing the dye emission at the edges. This suggests that LSCs for applications that require only small area energy harvesting, such as power internet-of-things (IOT) devices, could be feasible [89].

Furthermore, two MOFs having room-temperature phosphorescence have also been investigated: Zn-IPA and Zn-DTA. Both MOFs are synthesized using a microwave-assisted synthesis; Zn-IPA showed the same phosphorescence emission but with different lifetime with respect to the one reported in the literature. Zn-IPA has been used as a scaffold for the Iridium complex to have energy transfer between MOF and loaded molecule. Two loading attempts were performed: via solution loading and via reaction loading. Both attempts gave negative results, with no sign of characteristic absorption of the iridium molecule found in the absorption spectrum of the loaded MOF. On the other hand, in this work Zn-DTA was successfully synthesized for the first time as a brand new MOF showing the room temperature phosphorescence and red emission due to the presence of sulfur atom in the organic linker molecule. These are interesting materials in relation to the current push to develop unique markers and sensor materials. RTP molecules applied as a linker in MOF structure can have a great potential in oxygen sensing. RTP is highly influenced by the presence of oxygen and MOF pores provides the necessary proximity between RTP dye and oxygen molecule. A porous RTP system for sensing the oxygen has been already presented in the work of Zhou *et al.* showing a direct relationship between the presence of oxygen and the decreasing of RTP lifetime [90].

7.2 Outlook

In this work has been taken into account only H_4ETTC AIE dye. This dye absorbs mainly in the UV region and its emission is peaked around 500 nm. In order to increase the efficiency of the SURMOF based LSC, SURMOF can be infiltrated with a different AIE dye that has an absorption spectrum in the wavelength region where more photons from the sun are available and an emission spectrum that matches the spectral response of the silicon solar cell [91]. A good candidate is TTPEBTTD, synthetized by Zhao *et al*. [23], formed by 4,7-di(thiophen-2-yl)benzo-2,1,3-thiadiazole core and tetraphenylethene peripheries with a broad

absorption spectrum from 300 nm to 600 nm and an emission, when is cast in thin-film, peaked at 646 nm, as shown in Figure 7.2 b. The three TPE provides the AIE properties to the molecule and can be used as sites for functionalization with carboxylic groups, as is done during the synthesis of H_4ETTC, in order to make the dye loadable.

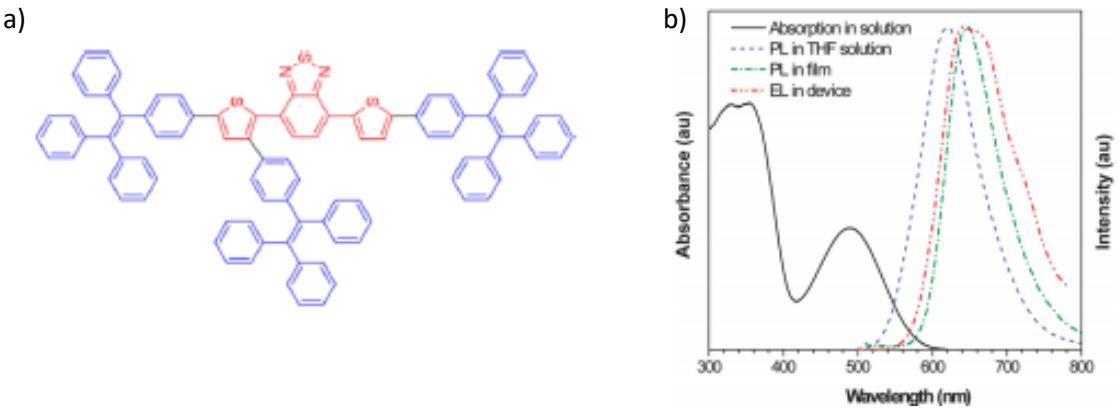

Figure 7.2: panel a) molecular structure of TTPEBTTD, in blue tetraphenylethene peripheries and in red the ,7-di(thiophen-2-yl)benzo-2,1,3-thiadiazole core. Panel b) absorption, emission spectrum (THF solution and thin-film) and electroluminescence spectrum of TTPEBTTD. Reproduced with permission [23].

An additional method for increasing the portion of the absorbed spectrum and the overall e-PLQY of the system is using SURMOF with an optically active linker, but the same structure of the SURMOF 2 that can be infiltrated with AIE chromophore. The ideal linker should be characterized by an overlap between its emission and the absorption spectrum of the loaded dye in order to have energy transfer between the two species. An example of a SURMOF with an optically active linker has been produced by Oldenburg *et al.* The SURMOF is made by zinc acetate as metal ion and 4,40-(anthracene-9,10-diyl)dibenzoate (ADB) as the organic linker [92, 93], as shown in Figure 7.3.

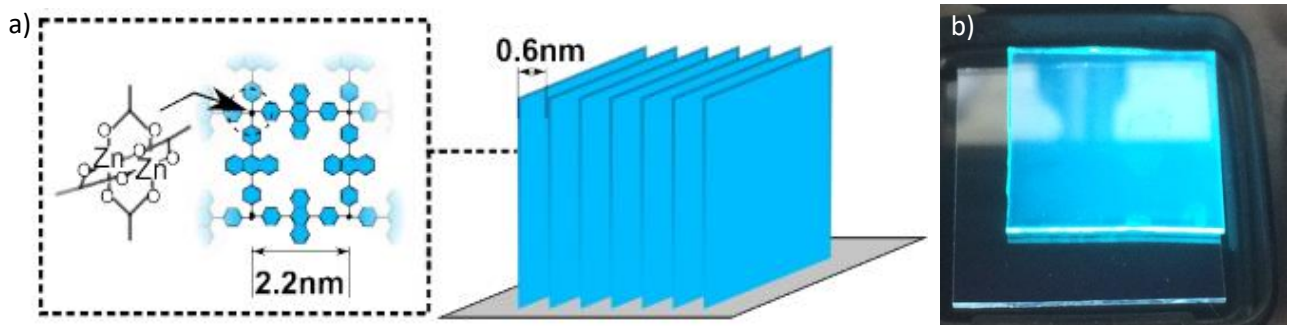

Figure 7.3: panel a) ZnADB SURMOF components and sheet-like structure, as for ZnBDC , with the same spacing of 0.6 nm between the molecular planes. Panel b) ZnADB sample on glass under UV illumination (365 nm). Picture reproduced and adapted with permission of [92].

In order to have a uniform loading and scattering reduction, the loading process in the LSC sample can be performed by inkjet-printing technique with the SURMOF substrate can be fully printed. In this direction, some tests have already been performed. In Figure 7.4 a four portions of the printed sample are reported: the top left portion is printed only with one printing step, the top right portion by two consecutive printing steps, the bottom left by three printing steps and the bottom right by four printing steps. The dye density

increases with the number of printing steps. A comparison between the printed sample and the drop-casted sample at the highest concentration is reported in Figure 7.4 b, where the latter one is characterized by a brighter emission indicating that several printing steps are required to achieve a comparable concentration.

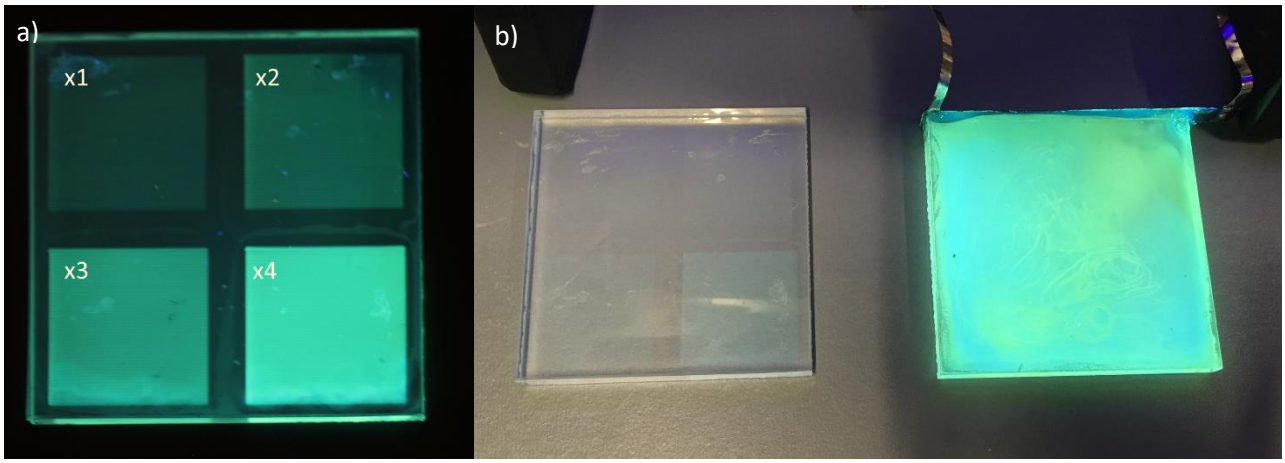

Figure 7.4: Panel a) ink-jet printing test for LSC, the different parts of the sample are printed with different dye concentrations. Panel b) the comparison between the ink-jet printed sample and the drop-casted sample showing the difference in the emission between the two samples.

Further investigations are required for the MOFs with room-temperature phosphorescence. Regarding Zn-IPA, the incorporation of the iridium complex should be performed applying the gas phase method, where the dye is brought into the gas phase and then put in contact with the MOF. For Zn-DTA, single-crystal XRD analysis should be performed to resolve the precise crystalline structure of the MOF and in addition optical characterization should be performed to understand the excitation dynamics inside the MOF.

References

1. Stavila, V., A.A. Talin, and M.D. Allendorf, *MOF-based electronic and opto-electronic devices.* Chemical Society Reviews, 2014. **43**(16): p. 5994-6010.
2. Yaghi, O.M. and H. Li, *Hydrothermal Synthesis of a Metal-Organic Framework Containing Large Rectangular Channels.* Journal of the American Chemical Society, 1995. **117**(41): p. 10401-10402.
3. Zacher, D., et al., *Thin films of metal–organic frameworks.* Chemical Society Reviews, 2009. **38**(5): p. 1418-1429.
4. Liu, J. and C. Wöll, *Surface-supported metal–organic framework thin films: fabrication methods, applications, and challenges.* Chemical Society Reviews, 2017. **46**(19): p. 5730-5770.
5. Shubert, E.F., *Light-Emitting Diodes*. 2° Edition ed. 2006: Cambrige University Press.
6. Weber, W.H. and J. Lambe, *Luminescent greenhouse collector for solar radiation.* Applied Optics, 1976. **15**(10): p. 2299-2300.
7. van Sark, W.G.J.H.M., *Luminescent solar concentrators – A low cost photovoltaics alternative.* Renewable Energy, 2013. **49**: p. 207-210.
8. Senden, T., R.J.A. van Dijk-Moes, and A. Meijerink, *Quenching of the red Mn4+ luminescence in Mn4+-doped fluoride LED phosphors.* Light: Science & Applications, 2018. **7**(1): p. 8.
9. Milonni, P.W.a.E., J. H. , *Absorption, Emission, and Dispersion of Light*, in *Laser Physics*. 2010.
10. Condon, E., *A Theory of Intensity Distribution in Band Systems.* Physical Review, 1926. **28**(6): p. 1182-1201.
11. Sauer, M., Hofkens, J. and Enderlein, *Basic Principles of Fluorescence Spectroscopy*, in *Handbook of Fluorescence Spectroscopy and Imaging*. 2011.
12. Kasha, M., *Characterization of electronic transitions in complex molecules.* Discussions of the Faraday Society, 1950. **9**(0): p. 14-19.
13. Liu, Y., et al., *Room-temperature phosphorescence from purely organic materials.* Chinese Chemical Letters, 2016. **27**(8): p. 1231-1240.
14. Ghosh, M., et al., *Fluorescence self-quenching of tetraphenylporphyrin in liquid medium.* Journal of Luminescence, 2013. **141**: p. 87-92.
15. Luo, J., et al., *Aggregation-induced emission of 1-methyl-1,2,3,4,5-pentaphenylsilole.* Chemical Communications, 2001(18): p. 1740-1741.
16. Shi, J., et al., *Locking the phenyl rings of tetraphenylethene step by step: understanding the mechanism of aggregation-induced emission.* Chemical Communications, 2012. **48**(86): p. 10675-10677.
17. Mei, J., et al., *Aggregation-Induced Emission: The Whole Is More Brilliant than the Parts.* Advanced Materials, 2014. **26**(31): p. 5429-5479.
18. Leung, N.L.C., et al., *Restriction of Intramolecular Motions: The General Mechanism behind Aggregation-Induced Emission.* Chemistry – A European Journal, 2014. **20**(47): p. 15349-15353.
19. Zhu, Q., et al., *A New Series of C-6 Unsubstituted Tetrahydropyrimidines: Convenient One-Pot Chemoselective Synthesis, Aggregation-Induced and Size-Independent Emission Characteristics.* Chemistry – A European Journal, 2012. **19**(4): p. 1268-1280.
20. Huang, J., et al., *Similar or Totally Different: The Control of Conjugation Degree through Minor Structural Modifications, and Deep-Blue Aggregation-Induced Emission Luminogens for Non-Doped OLEDs.* Advanced Functional Materials, 2012. **23**(18): p. 2329-2337.
21. Shuming, C., et al., *Non-doped white organic light-emitting diodes based on aggregation-induced emission.* Journal of Physics D: Applied Physics, 2010. **43**(9): p. 095101.
22. Yue, Z., et al., *Hybrid GaN/Organic white light emitters with aggregation induced emission organic molecule.* Optical Materials Express, 2013. **3**(11): p. 1906-1911.
23. Zhao, Z., et al., *A tetraphenylethene-based red luminophor for an efficient non-doped electroluminescence device and cellular imaging.* Journal of Materials Chemistry, 2012. **22**(22): p. 11018-11021.

24. Yaghi, O.M., et al., *Reticular synthesis and the design of new materials.* Nature, 2003. **423**: p. 705.
25. Lu, W., et al., *Tuning the structure and function of metal–organic frameworks via linker design.* Chemical Society Reviews, 2014. **43**(16): p. 5561-5593.
26. Chen, T.-H., et al., *Metal–Organic Frameworks: Rise of the Ligands.* Chemistry of Materials, 2014. **26**(15): p. 4322-4325.
27. Latroche, M., et al., *Hydrogen Storage in the Giant-Pore Metal–Organic Frameworks MIL-100 and MIL-101.* Angewandte Chemie, 2006. **118**(48): p. 8407-8411.
28. Eddaoudi, M., et al., *Systematic Design of Pore Size and Functionality in Isoreticular MOFs and Their Application in Methane Storage.* Science, 2002. **295**(5554): p. 469.
29. Furukawa, H., et al., *Ultrahigh Porosity in Metal-Organic Frameworks.* Science, 2010. **329**(5990): p. 424.
30. Yaghi, O.M., G. Li, and H. Li, *Selective binding and removal of guests in a microporous metal–organic framework.* Nature, 1995. **378**: p. 703.
31. Gascon, J., et al., *Metal Organic Framework Catalysis: Quo vadis?* ACS Catalysis, 2014. **4**(2): p. 361-378.
32. Stock, N. and S. Biswas, *Synthesis of Metal-Organic Frameworks (MOFs): Routes to Various MOF Topologies, Morphologies, and Composites.* Chemical Reviews, 2012. **112**(2): p. 933-969.
33. Rabenau, A., *The Role of Hydrothermal Synthesis in Preparative Chemistry.* Angewandte Chemie International Edition in English, 1985. **24**(12): p. 1026-1040.
34. Gedye, R., et al., *The use of microwave ovens for rapid organic synthesis.* Tetrahedron Letters, 1986. **27**(3): p. 279-282.
35. Perry, J.J., Bauer, C. A. and Allendorf, M. D., *Luminescent Metal–Organic Frameworks*, in *Metal-Organic Frameworks*. 2011.
36. Allendorf, M.D., et al., *Luminescent metal–organic frameworks.* Chemical Society Reviews, 2009. **38**(5): p. 1330-1352.
37. Bordiga, S., et al., *Electronic and vibrational properties of a MOF-5 metal–organic framework: ZnO quantum dot behaviour.* Chemical Communications, 2004(20): p. 2300-2301.
38. He, X., et al., *A Series of One- to Three-Dimensional Copper Coordination Polymers Based on N-Heterocyclic Ligands.* European Journal of Inorganic Chemistry, 2006. **2006**(12): p. 2491-2503.
39. Jayaramulu, K., et al., *Luminescent Microporous Metal–Organic Framework with Functional Lewis Basic Sites on the Pore Surface: Specific Sensing and Removal of Metal Ions.* Inorganic Chemistry, 2012. **51**(19): p. 10089-10091.
40. Meek, S., et al., *Luminescent Metal-Organic Frameworks: A Nanolaboratory for Probing Energy Transfer via Interchromophore Interactions.* ECS Transactions, 2010. **28**(3): p. 137-143.
41. Wei, Z., et al., *Rigidifying Fluorescent Linkers by Metal–Organic Framework Formation for Fluorescence Blue Shift and Quantum Yield Enhancement.* Journal of the American Chemical Society, 2014. **136**(23): p. 8269-8276.
42. Li, X., et al., *Unique (3,12)-Connected Porous Lanthanide−Organic Frameworks Based on Ln4O4 Clusters: Synthesis, Crystal Structures, Luminescence, and Magnetism.* Inorganic Chemistry, 2010. **49**(4): p. 1865-1871.
43. Li, X., et al., *Syntheses of Metal−2-(Pyridin-4-yl)-1H-imidazole-4,5-dicarboxylate Networks with Topological Diversity: Gas Adsorption, Thermal Stability and Fluorescent Emission Properties.* Crystal Growth & Design, 2009. **9**(8): p. 3423-3431.
44. Müller, M., et al., *Highly emissive metal–organic framework composites by host–guest chemistry.* Photochemical & Photobiological Sciences, 2010. **9**(6): p. 846-853.
45. Wagner, B.D., et al., *Exciplex fluorescence of {[Zn(bipy)1.5(NO3)2}]·CH3OH·0.5pyrene}n: a coordination polymer containing intercalated pyrene molecules (bipy = 4,4'-bipyridine).* Chemical Communications, 2002(18): p. 2176-2177.
46. Falcaro, P., et al., *Centimetre-scale micropore alignment in oriented polycrystalline metal–organic framework films via heteroepitaxial growth.* Nature Materials, 2016. **16**: p. 342.
47. Bétard, A. and R.A. Fischer, *Metal–Organic Framework Thin Films: From Fundamentals to Applications.* Chemical Reviews, 2012. **112**(2): p. 1055-1083.

48. Gliemann, H. and C. Wöll, *Epitaxially grown metal-organic frameworks.* Materials Today, 2012. **15**(3): p. 110-116.
49. Liu, J., et al., *Deposition of Metal-Organic Frameworks by Liquid-Phase Epitaxy: The Influence of Substrate Functional Group Density on Film Orientation.* Materials, 2012. **5**(9).
50. Heinke, L., et al., *Surface-mounted metal-organic frameworks for applications in sensing and separation.* Microporous and Mesoporous Materials, 2015. **216**: p. 200-215.
51. Shekhah, O., et al., *Step-by-Step Route for the Synthesis of Metal–Organic Frameworks.* Journal of the American Chemical Society, 2007. **129**(49): p. 15118-15119.
52. Arslan, H.K., et al., *High-Throughput Fabrication of Uniform and Homogenous MOF Coatings.* Advanced Functional Materials, 2011. **21**(22): p. 4228-4231.
53. Arslan, H.K., et al., *Intercalation in Layered Metal–Organic Frameworks: Reversible Inclusion of an Extended π-System.* Journal of the American Chemical Society, 2011. **133**(21): p. 8158-8161.
54. Chernikova, V., O. Shekhah, and M. Eddaoudi, *Advanced Fabrication Method for the Preparation of MOF Thin Films: Liquid-Phase Epitaxy Approach Meets Spin Coating Method.* ACS Applied Materials & Interfaces, 2016. **8**(31): p. 20459-20464.
55. Gu, Z.-G., et al., *Transparent films of metal-organic frameworks for optical applications.* Microporous and Mesoporous Materials, 2015. **211**: p. 82-87.
56. Baroni, N., et al., *Facile loading of thin-film surface-anchored metal-organic frameworks with Lewis-base guest molecules.* Materials Chemistry Frontiers, 2017. **1**(9): p. 1888-1894.
57. de Mello, J.C., H.F. Wittmann, and R.H. Friend, *An improved experimental determination of external photoluminescence quantum efficiency.* Advanced Materials, 2004. **9**(3): p. 230-232.
58. Hamamatsu, *Guide to Streak Camera* *https://www.hamamatsu.com/resources/pdf/sys/SHSS0006E_STREAK.pdf*.
59. Yang, X. and D. Yan, *Strongly Enhanced Long-Lived Persistent Room Temperature Phosphorescence Based on the Formation of Metal–Organic Hybrids.* Advanced Optical Materials, 2016. **4**(6): p. 897-905.
60. Klinowski, J., et al., *Microwave-Assisted Synthesis of Metal–Organic Frameworks.* Dalton Transactions, 2011. **40**(2): p. 321-330.
61. Liu, J., et al., *A novel series of isoreticular metal organic frameworks: realizing metastable structures by liquid phase epitaxy.* Scientific Reports, 2012. **2**: p. 921.
62. Liu, Z.-c., et al., *An effective Cu(ii) quenching fluorescence sensor in aqueous solution and 1D chain coordination polymer framework.* Dalton Transactions, 2011. **40**(37): p. 9370-9373.
63. Bhyrappa, P. and K.S. Suslick, *Synthesis and crystal structure of 5,10,15,20-tetrakis(3,5-dinitrophenyl)porphyrin.* Journal of Porphyrins and Phthalocyanines, 1998. **2**(4-5): p. 391-396.
64. Singh, A. and L.W. Johnson, *Phosphorescence spectra and triplet state lifetimes of palladium octaethylporphyrin, palladium octaethylchlorin and palladium 2,3-dimethyloctaethylisobacteriochlorin at 77 K.* Spectrochimica Acta Part A: Molecular and Biomolecular Spectroscopy, 2003. **59**(5): p. 905-908.
65. Harriman, A., *Quantitative Analysis of Molecular Oxygen Using Palladium Porphyrins.* Platinurn Metals Rev, 1990. **34**(4): p. 181-184.
66. Kalinowski, J., et al., *Photophysics of an electrophosphorescent platinum (II) porphyrin in solid films.* The Journal of Chemical Physics, 2005. **122**(15): p. 154710.
67. Mandal, S., et al., *Photophysical properties of ionic liquid-assisted porphyrin nanoaggregate-nickel phthalocyanine conjugates and singlet oxygen generation.* Journal of Materials Chemistry C, 2014. **2**(41): p. 8691-8699.
68. Dienel, T., et al., *Novel near-infrared photoluminescence from platinum(II)-porphyrin (PtOEP) aggregates.* Journal of Luminescence, 2004. **110**(4): p. 253-257.
69. Serpone, N. and M.A. Jamieson, *Picosecond spectroscopy of transition metal complexes.* Coordination Chemistry Reviews, 1989. **93**(1): p. 87-153.
70. Guo, W., et al., *Loading of ionic compounds into metal–organic frameworks: a joint theoretical and experimental study for the case of La3+.* Physical Chemistry Chemical Physics, 2014. **16**(33): p. 17918-17923.

71. Baroni, N., et al., *Inkjet-Printed Photoluminescent Patterns of Aggregation-Induced-Emission Chromophores on Surface-Anchored Metal–Organic Frameworks.* ACS Applied Materials & Interfaces, 2018. **10**(30): p. 25754-25762.
72. Yan, X., et al., *Highly emissive platinum(II) metallacages.* Nat Chem, 2015. **7**(4): p. 342-348.
73. Alamán, J., et al., *Inkjet Printing of Functional Materials for Optical and Photonic Applications.* Materials (Basel, Switzerland), 2016. **9**(11): p. 910.
74. Hoth, C.N., et al., *High Photovoltaic Performance of Inkjet Printed Polymer:Fullerene Blends.* Advanced Materials, 2007. **19**(22): p. 3973-3978.
75. Chang, S.-C., et al., *Multicolor Organic Light-Emitting Diodes Processed by Hybrid Inkjet Printing.* Advanced Materials, 1999. **11**(9): p. 734-737.
76. de Gans, B.J., P.C. Duineveld, and U.S. Schubert, *Inkjet Printing of Polymers: State of the Art and Future Developments.* Advanced Materials, 2004. **16**(3): p. 203-213.
77. Cummins, G. and M.P.Y. Desmulliez, *Inkjet printing of conductive materials: a review.* Circuit World, 2012. **38**(4): p. 193-213.
78. Rowan, B.C., L.R. Wilson, and B.S. Richards, *Advanced Material Concepts for Luminescent Solar Concentrators.* IEEE Journal of Selected Topics in Quantum Electronics, 2008. **14**(5): p. 1312-1322.
79. solar, O., *Operating Instructions Sun Simulator Continuous-Light Sun Simulator for Thin Film Solar Cells and Modules.*
80. Desmet, L., et al., *Monocrystalline silicon photovoltaic luminescent solar concentrator with 4.2% power conversion efficiency.* Optics Letters, 2012. **37**(15): p. 3087-3089.
81. Baldo, M.A., et al., *Highly efficient phosphorescent emission from organic electroluminescent devices.* Nature, 1998. **395**(6698): p. 151-154.
82. Xue, P., et al., *Luminescence switching of a persistent room-temperature phosphorescent pure organic molecule in response to external stimuli.* Chemical Communications, 2015. **51**(52): p. 10381-10384.
83. Zhao, J., et al., *Triplet photosensitizers: from molecular design to applications.* Chemical Society Reviews, 2013. **42**(12): p. 5323-5351.
84. Yuan, W.Z., et al., *Crystallization-Induced Phosphorescence of Pure Organic Luminogens at Room Temperature.* The Journal of Physical Chemistry C, 2010. **114**(13): p. 6090-6099.
85. Liu, Z., W. He, and Z. Guo, *Metal coordination in photoluminescent sensing.* Chemical Society Reviews, 2013. **42**(4): p. 1568-1600.
86. You, Y. and S.Y. Park, *Inter-Ligand Energy Transfer and Related Emission Change in the Cyclometalated Heteroleptic Iridium Complex: Facile and Efficient Color Tuning over the Whole Visible Range by the Ancillary Ligand Structure.* Journal of the American Chemical Society, 2005. **127**(36): p. 12438-12439.
87. Shimizu, M., et al., *Aggregation-Induced Orange-to-Red Fluorescence of 2,5-Bis(diarylamino)terephthalic Acid Dithioesters.* European Journal of Organic Chemistry, 2016. **2016**(36): p. 5950-5956.
88. Pengo. *Pixel geometry*. 2009; Available from: https://upload.wikimedia.org/wikipedia/commons/4/4d/Pixel_geometry_01_Pengo.jpg.
89. Traverse, C.J., et al., *Emergence of highly transparent photovoltaics for distributed applications.* Nature Energy, 2017. **2**(11): p. 849-860.
90. Zhou, Y., et al., *Long-Lived Room-Temperature Phosphorescence for Visual and Quantitative Detection of Oxygen.* Angewandte Chemie International Edition, 2019. **58**(35): p. 12102-12106.
91. Debije, M.G. and P.P.C. Verbunt, *Thirty Years of Luminescent Solar Concentrator Research: Solar Energy for the Built Environment.* Advanced Energy Materials, 2012. **2**(1): p. 12-35.
92. Oldenburg, M., et al., *Enhancing the photoluminescence of surface anchored metal–organic frameworks: mixed linkers and efficient acceptors.* Physical Chemistry Chemical Physics, 2018. **20**(17): p. 11564-11576.
93. Oldenburg, M., et al., *Photon Upconversion at Crystalline Organic–Organic Heterojunctions.* Advanced Materials, 2016. **28**(38): p. 8477-8482.

Appendix:

HNMR spectra of the first three steps in the synthesis of 4′,4‴,4⁗,4⁗′-(Ethene-1,1,2,2-tetrayl)tetrakis-(([1,1′-biphenyl]-3-carboxylic acid)) (H_4ETTC).

1° Step

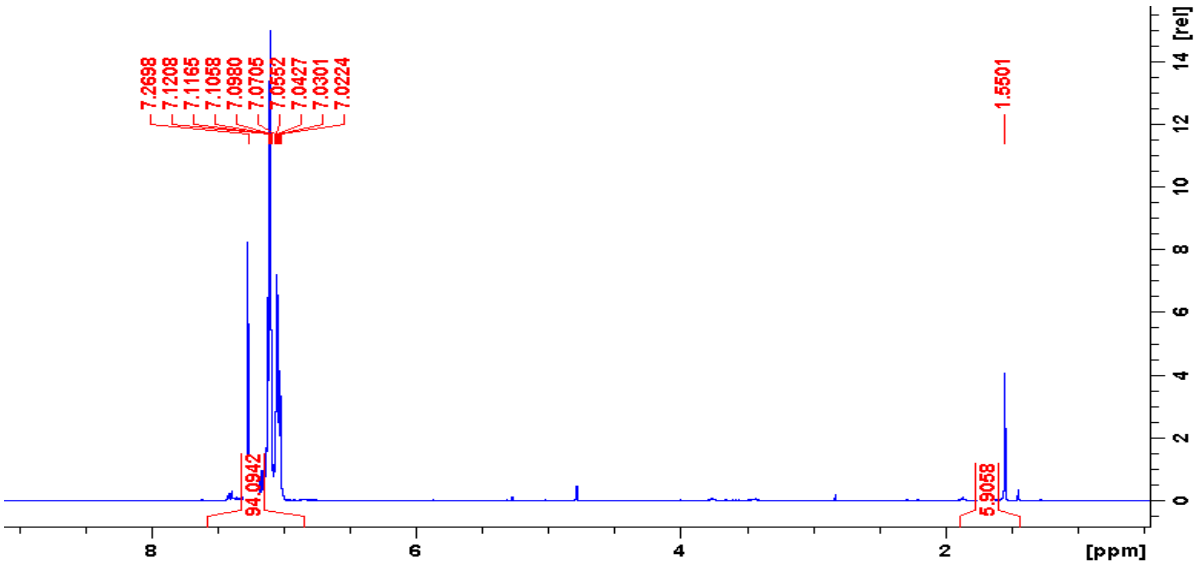

Figure A.1: HNMR spectrum of the 1° Step synthesis of tetraphenylethene in deuterated chloroform ($CDCl_3$).

2° Step

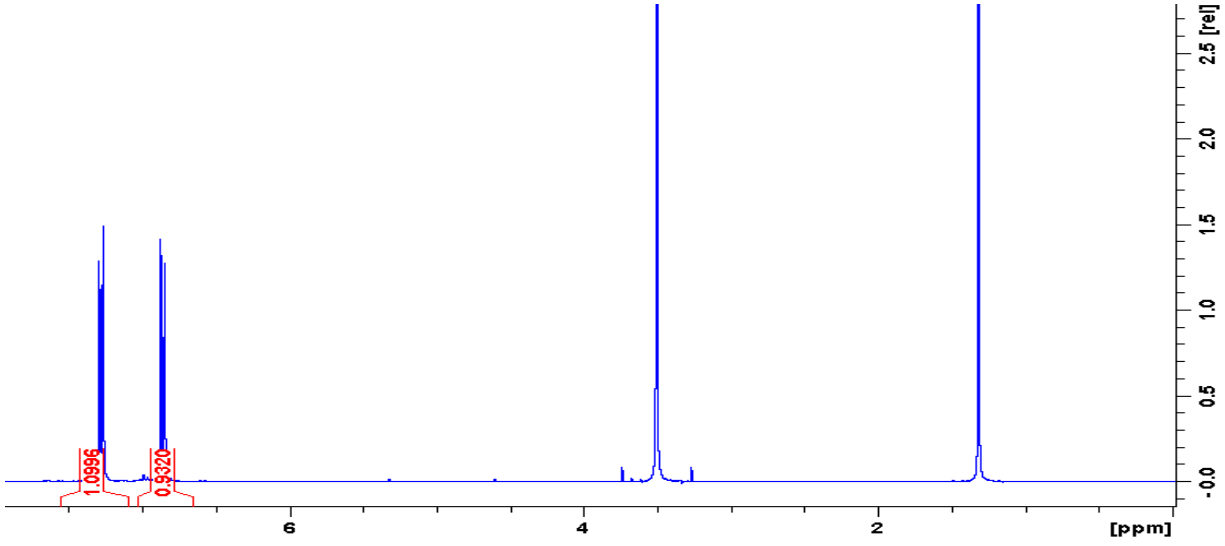

Figure A.2: HNMR spectrum of the 2° step Tetrakis(4-bromophenyl)ethane in DMSO.

3° Step

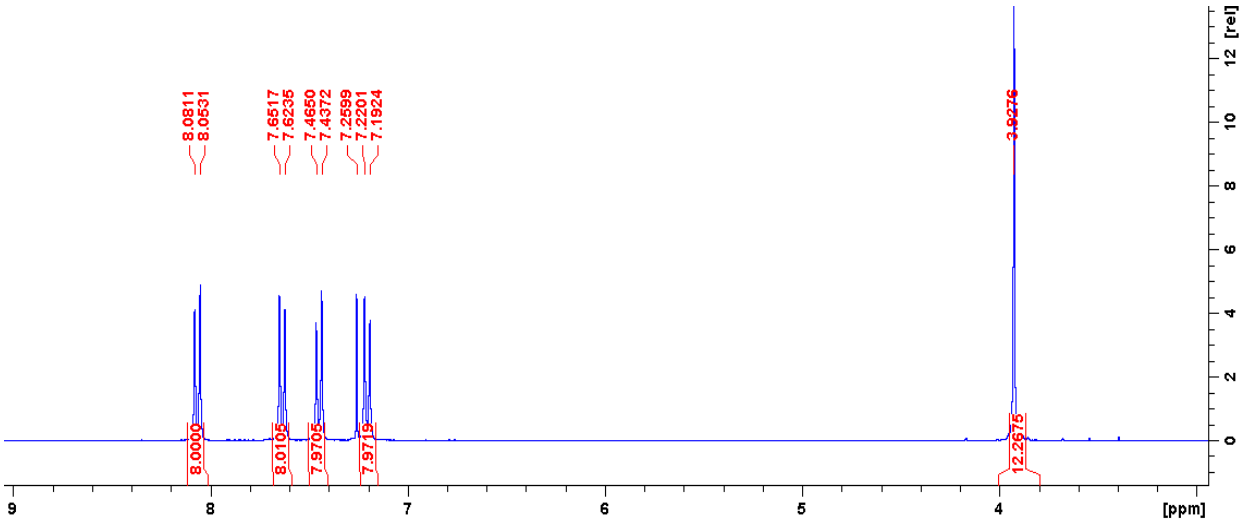

Figure A.3: HNMR spectrum of the 3° step synthesis of Tetramethyl4',4''',4''''',4'''''''-(ethene-1,1,2,2-tetrayl)tetrakis([1,1'-biphenyl]-4-carboxylate) in $CDCl_3$.

Silicon solar cell: EQE and I-V curve:

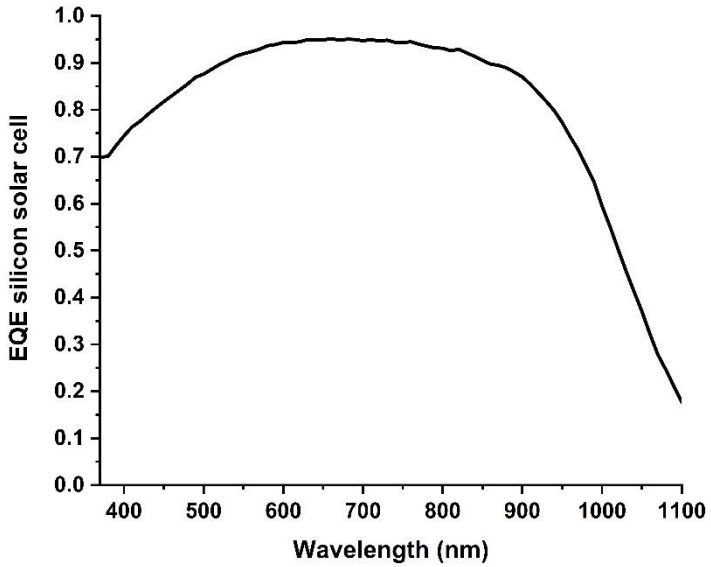

Figure A.4: EQE silicon solar cell.

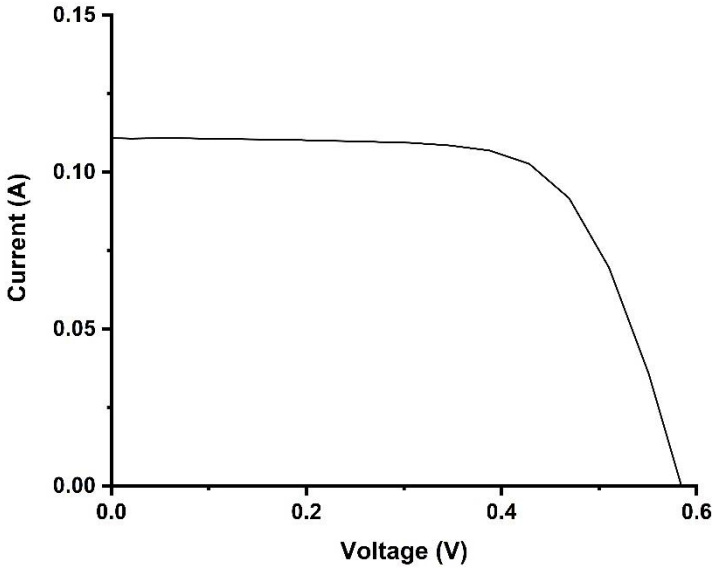

Figure A.5: I-V curve of the silicon solar cell record under the AM 1.5 global radiation of the sun simulator

Sun simulator: AM 1.5 global spectrum and T% filter RG 630

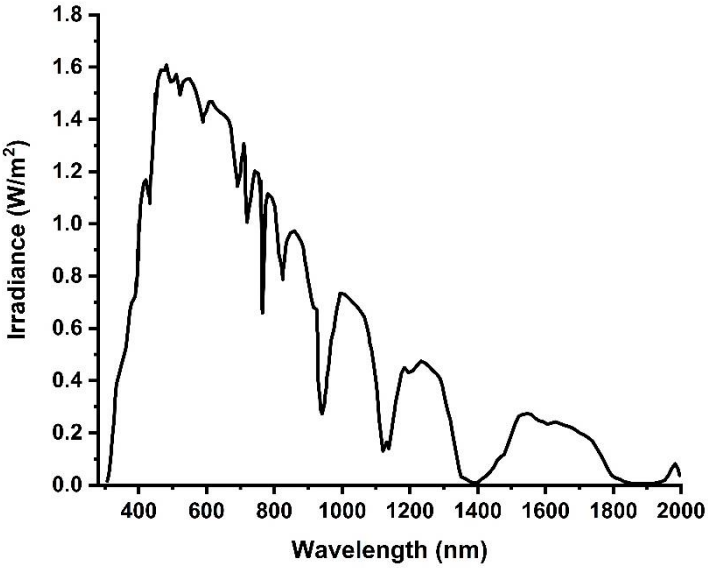

Figure A.6 : spectrum of the light produced by the solar simulator in order to simulate the AM 1.5 global spectrum. The spectrum has been taken from the device manual [79]

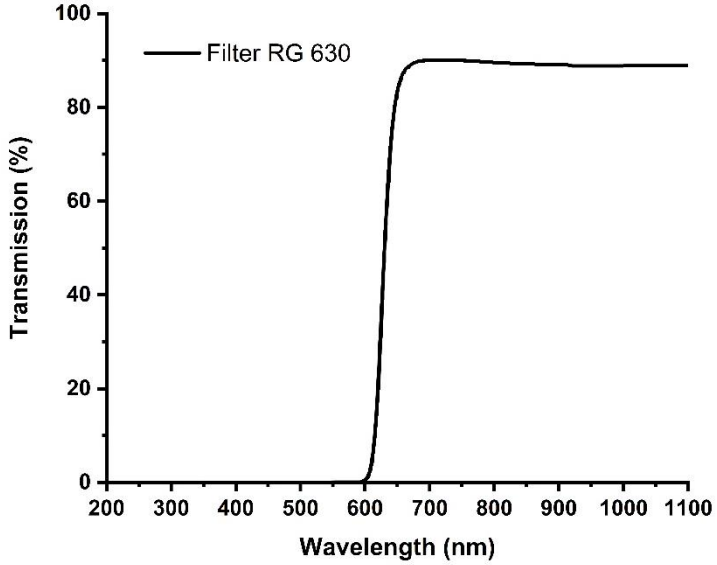

Figure A.7: transmission spectrum of the long pass filter RG 630. The filter allows to pass all the wavelengths above 630 nm and it is used in the measurments of $I_{SC\ Red}$.